Material-Specific Computed Tomography for Molecular X-Imaging in Biomedical Research

Xu Dong

Dissertation submitted to the faculty of the
Virginia Polytechnic Institute and State University
in partial fulfillment of the requirements for the degree of

Doctor of Philosophy
In
Biomedical Engineering and Mechanics

Guohua Cao, Chair
J. Daniel Bourland
Stephen M. LaConte
Yizheng Zhu
Yunhui Zhu

March 26, 2019
Blacksburg, Virginia

Keywords: Computed Tomography, Molecular Imaging, X-ray Fluorescence, Photon Counting CT, Deep Learning

Material-Specific Computed Tomography for Molecular X-ray Imaging in Biomedical Research

Xu Dong

ABSTRACT

X-ray Computed Tomography (CT) imaging has been playing a central role in clinical practice since it was invented in 1972. However, the traditional x-ray CT technique fails to distinguish different materials with similar density, especially for biological tissues. The lack of a quantitative imaging representation has constrained the application of CT technique from a broadening application such as personal or precision medicine. Therefore, my major thesis statement is to develop novel material-specific CT imaging techniques for molecular imaging in biological bodies. To achieve the goal, comprehensive studies were conducted to investigate three different techniques: x-ray fluorescence molecular imaging, material identification (specification) from photon counting CT, and photon counting CT data distortion correction approach based on deep learning.

X-ray fluorescence molecular imaging (XFMI) has shown great promise as a low-cost molecular imaging modality for clinical and pre-clinical applications with high sensitivity. In this study, the effects of excitation beam spectrum on the molecular sensitivity of XFMI were experimentally investigated, by quantitatively deriving minimum detectable concentration (MDC) under a fixed surface entrance dose of 200 mR at three different excitation beam spectra. The result shows that the MDC can be readily increased by a factor of 5.26 via excitation spectrum optimization. Furthermore, a numerical model was developed and validated by the experimental data ($PCC \geq 0.976$). The numerical model can be used to optimize XFMI system configurations to further improve the molecular sensitivity. Findings from this investigation could find applications for in vivo pre-clinical small-animal XFMI in the future.

PCCT is an emerging technique that has the ability to distinguish photon energy and generate much richer image data that contains x-ray spectral information compared to conventional CT. In this study, a physics model was developed based on x-ray matter interaction physics to calculate the effective atomic number (Z_{eff}) and effective electron density ($\rho_{e_{eff}}$) from PCCT image data for material identification. As the validation of the physics model, the Z_{eff} and $\rho_{e_{eff}}$ were calculated under various energy conditions for many materials. The relative standard deviations are mostly less than 1% (161 out of 168) shows that the developed model obtains good accuracy and robustness to energy conditions. To study the feasibility of applying the model with PCCT image data for material identification, both PCCT system numerical simulation and physical experiment were conducted. The result shows different materials can be clearly identified in the $Z_{eff} - \rho_{e_{eff}}$ map (with relative error $\leq$ 8.8%). The model has the value to serve as a material identification scheme for PCCT system for practical use in the future.

As PCCT appears to be a significant breakthrough in CT imaging field, there exists severe data distortion problem in PCCT, which greatly limits the application of PCCT in practice. Lately, deep learning (DL) neural network has demonstrated tremendous success in medical imaging field. In this study, a deep learning neural network based PCCT data distortion correction method was proposed. When applying the algorithm to process the test dataset data, the accuracy of the PCCT data can be greatly improved (RMSE improved 73.7%). Compared with traditional data correction approaches such as maximum likelihood, the deep learning approach demonstrate superiority in terms of RMSE, SSIM, PSNR, and most importantly, runtime (4053.21 sec vs. 1.98 sec). The proposed method has the potential to facilitate the PCCT studies and applications in practice.

Material-Specific Computed Tomography for Molecular X-ray Imaging in Biomedical Research

Xu Dong

GENERAL AUDIENCE ABSTRACT

X-ray Computed Tomography (CT) has played a central role in clinical imaging since it was invented in 1972. It has distinguishing characteristics of being able to generate three dimensional images with comprehensive inner structural information in fast speed (less than one second). However, traditional CT imaging lacks of material-specific capability due to the mechanism of image formation, which makes it cannot be used for molecular imaging. Molecular imaging plays a central role in present and future biomedical research and clinical diagnosis and treatment. For example, imaging of biological processes and molecular markers can provide unprecedented rich information, which has huge potentials for individualized therapies, novel drug design, earlier diagnosis, and personalized medicine. Therefore there exists a pressing need to enable the traditional CT imaging technique with material-specific capability for molecular imaging purpose.

This dissertation conducted comprehensive study to separately investigate three different techniques: x-ray fluorescence molecular imaging, material identification (specification) from photon counting CT, and photon counting CT data distortion correction approach based on deep learning. X-ray fluorescence molecular imaging utilizes fluorescence signal to achieve molecular imaging in CT; Material identification can be achieved based on the rich image data from PCCT; The deep learning based correction method is an efficient approach for PCCT data distortion correction, and furthermore can boost its performance on material identification. With those techniques, the material-specific capability of CT can be greatly enhanced and the molecular imaging can be approached in biological bodies.

Dedicated to the days and nights spent on working and researching.

ACKNOWLEDGEMENTS

First of all, I owe unending honor and gratitude to my advisor, Dr. Guohua Cao. Back to five year ago, I decided to pursue my Ph.D. degree overseas in biomedical engineering, which was a huge challenge for me who could only speak very little English and with only physics background. Dr. Cao took a leap of faith and welcomed me into the lab. He has been an amazing advisor with his terrific mentoring, intelligence, dedication, and kindness. I deeply appreciate his guidance and encouragement that I have gained to keep me on the track and to overcome the challenges. I would also like to thank Dr. Daniel Bourland, Dr. Stephen LaConte, Dr. Yizheng Zhu, and Dr. Yunhui Zhu for serving on my advisory committee and providing suggestions and helps that are invaluable.

I am very grateful to have the laboratory mates and collaborators: Dr. Olga V. Pen, Dr. Zhicheng Zhang, Mr. Swapnil Vekhande, Dr. Shunli Zhang, Dr. Eric Z. Chen, and Dr. Hao Gong. Your diligence and productivity have motivated me so much. Thank you all for your assistance, advice, and friendship.

Last but not the least, I would like to thank my family from the bottom of my heart for their understanding, love, and support.

Table of Contents

List of Figures

List of Tables

List of Abbreviations

CT	Computed tomography
MRI	Magnetic resonance imaging
PET	Positron emission tomography
SPECT	Single photon emission computed tomography
XFMI	X ray fluorescence molecular imaging
PCCT	Photon counting computed tomography
MDC	Minimum detectable concentration
PCC	Pearson correlation coefficient
Z_{eff}	Effective atomic number
$\rho_{e_{eff}}$	Effective electron density
E_{eff}	Effective energy
E	X-ray photon energy
μ	Attenuation coefficient
DL	Deep learning
ML	Maximum Likelihood
RMSE	Root mean square error
SSIM	Structural simularity
PSNR	Peak signal to noise ratio

Chapter 1 Introduction

1.1 Overview of x-ray CT

X-ray Computed Tomography (CT) is a technique of generating cross-sectional images of an object and non-invasively resolving internal structures [2, 3]. The foundation of CT can be divided into two aspects: physical aspect, and mathematical aspect. From physical aspect, different materials have different x-ray attenuation coefficients, and therefore CT employs x-ray to revolve the structural information of scanned objects by resolving the x-ray attenuation difference [4-6]. From mathematical aspect, the cross-sectional images can be reconstructed from projection data in many different views by tomography algorithm [7, 8]. After the reconstruction process, the internal structural information of scanned object can be presented in images.

The first commercial x-ray CT prototype was created by Godfrey Hounsfield in 1972 [9, 10], and it has been playing a significant role in clinics since its invention. Compared to other imaging modalities such as x-ray imaging, magnetic resonance imaging (MRI) [11], positron emission tomography (PET) [12], single‐photon emission computed tomography (SPECT) [13], etc., CT imaging has distinguishing characteristics of being able to generate three dimensional images with comprehensive inner structural information in fast speed (less than one second). The advantages make CT be the most frequently used imaging technique in clinical practice that the doctors rely heavily on for diagnosis.

1.2 The evolution of CT technique

The CT technique has been tremendously improved over the last four decades since its invention. The improvements come from many aspects: the system design, the spatial resolution, the temporary resolution, the contrast, and so on [3].

The first generation of CT was designed to use a parallel x-ray beam. The relative positions of x-ray source and detector were fixed. Both translational movement and angular

movement have to be made to scan one object and therefore it takes more than four minutes to finish one complete scan.

The second generation of CT started to use multiple detector pixels to collect data simultaneously at multiple angles. Even though translational movement are still needed, the scan time was greatly reduced compared to first generation CT scanner. The total scan time falls into the magnitude of seconds in second generation of CT.

The third generation of CT utilized more detector pixels that are sufficiently large to cover the scanned object all the time. Therefore the translational movement can be totally avoided in third generation CT scanner. Other technologies such as slip ring were invented as well to further facilitate the gantry rotation speed. The temporal resolution of CT was increased largely so that imaging of moving organs such as lung and cardiac became possible in third generation of CT.

The fourth generation of CT utilized a complete ring of detectors so that only x-ray tube needs to rotate during the entire scan. Even though several advantages are demonstrated in this design such as better detector stability and less aliasing, technical challenge along with the design such as the scattered photons have limited the fourth generation of CT from gaining popularity in the market.

1.3 Molecular imaging and material-specific CT

Molecular imaging (MI) is one of the most rapidly developing areas in biomedical imaging [14], which plays a central role in present and future biomedical research and clinical diagnosis and treatment. MI has the ability to *in vivo* characterize diseased tissues at the molecular level without invasive biopsies or other surgical procedures. It can provide unprecedented rich information if imaging of biological processes and molecular markers can be achieved, which has huge potentials for individualized therapies, novel drug design, earlier diagnosis, and personalized medicine [15-18]. For example, it empowers scientists to detect a tumor in its early stage in oncology and cancer biology, and also to visualize the

activity of a specific molecule or a biological process that is relevant to tumor development, therapy efficacy, and so on [19-21].

X-ray Computed Tomography (CT) imaging was among the most significant development in medical imaging since it was invented in 1972. The traditional CT measures the sum of the energy of x-ray photons incident on the detector. And after reconstruction and normalization, CT number [22] is used for image representation (pixel value in CT image), which is related to the averaged attenuation coefficient of the material weighted over the whole x-ray spectrum. Since the attenuation coefficient of a material is jointly determined by its chemical composition and mass density, and the x-ray photon energy, the mechanism of traditional CT resolving object leads to a few major limitations. First, The CT image often fails to distinguish different soft tissues because the CT number of them are very close. Figure 1.1 displays an abdomen image generated by a standard CT [1]. The contrast between the kidney and the around soft tissues in the image is almost not visible. The insufficient soft tissue contrast is caused by the fact that the mass densities of the soft tissues are so similar that leads to the very close CT numbers. Second, the CT images are not material-specific [23]. The CT images generated from different CT scanner often displays some difference even for the same biological material. Using CT number as CT image pixel value is not a quantitative, but rather qualitative image representation method [23]. The lack of the material-specific capability has greatly constrained the traditional CT technique from broadening applications in personal or precision medicine for many diseases such as cancers [19, 20]. Therefore, it is significant to develop novel CT techniques with material-specific capability for molecular imaging in biological bodies.

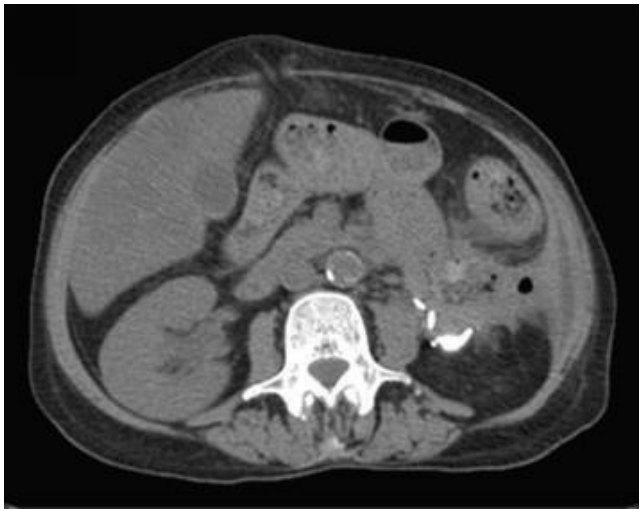

Figure 1.1: A typical abdomen CT image from a standard CT scanner [1].

1.4 Dissertation organization

The organization of the remaining chapters of this dissertation is as follows:

Chapter 2 introduces the x-ray fluorescence molecular imaging (XFMI). The XFMI technique utilizes x-ray fluorescence for molecular imaging, and therefore has the potential to enable CT with molecular imaging capability [21, 24-36]. In this study, the potential of XFMI was systematically and experimentally investigated and a molecular sensitivity improving technique was developed via excitation beam optimization. The chapter presents the theoretical model, the experimental design and construction, the data processing, and the numerical simulation. It also presents the evaluation method and the evaluation result.

Chapter 3 introduces a material identification method from photon counting CT (PCCT). PCCT is an emerging technique that has the ability to distinguish photon energy and generate much richer image data that contains x-ray spectral information compared to conventional CT [23, 37-42]. The richness of image data opens the possibility to achieve material identification (specification) from PCCT, and henceforth can achieve the material-specific function from CT imaging [43-53]. In this study, a physics model was developed to calculate effective atomic number (Z_{eff}) and effective electron density ($\rho_{e_{eff}}$) from PCCT data for material identification. Both physical experiment and numerical simulation were conducted to investigate the feasibility of the method and the result shows an

improved accuracy can be obtained from the method. The chapter presents the physics model, the validation of the physics model, the physical experiment and the numerical simulation, and data processing method. A comprehensive evaluation of the result is also conducted and reported in the chapter.

Chapter 4 introduces a correction approach for PCCT data distortion. The data distortion existing in PCCT is the long standing problem which is the biggest factor that diminishes the material identification (specification) accuracy from PCCT [23, 54, 55]. For example, as reported in the study of chapter 3, when using the distorted PPCT data for material identification, the error can be as high as 6.3%, as compared to the error of 2.1% without data distortion. To better complete the goal of achieving material-specific function from PCCT data, a PCCT data distortion correction approach was developed with deep learning neural network. This chapter presents the data preparation, the PCCT system simulation, the neural network design and training, and evaluation of the result. The developed approach was also compared with conventional maximum likelihood approach, and the result is also demonstrated in the chapter.

Chapter 5 introduce the overall discussion, conclusion, and outlook for all the studies presented in chapter 2, chapter 3, and chapter 4, which finally concludes this dissertation.

1.5 Attribution

In this section, the contribution of each author in the following chapters of this dissertation are briefly reported below, since these works are not sole-authorships.

Chapter 2 is the extended version of the paper titled “Improving Molecular Sensitivity in X-Ray Fluorescence Molecular Imaging (XFMI) of Iodine Distribution in Mouse-Sized Phantoms via Excitation Spectrum Optimization” (published in IEEE ACCESS) [56]. As the first author, my contribution includes the following aspects: the design and construction of XFMI system, the data processing and analysis, and the numerical simulation implementation. Dr. Cheng Chen contributed to the phantom material supply and Dr. Guohua Cao supervised the study.

Chapter 3 is the combination of the conference paper titled "An improved physics model for multi-material identification in photon counting CT" (published in SPIE Medical Imaging 2019) [55] and the manuscript titled "Improved material identification via accurate calculation of effective atomic number and electron density from photon counting CT images" (under review by Medical Physics). The authors for both two manuscripts are composed of myself, Olga V. Pen, Zhicheng Zhang, and Guohua Cao. As the first author, I contributed to the following aspects of this study: the physics model derivation and implementation, the physical experiment design and construction, the numerical simulation implementation, and the data processing and analysis. Ms. Olga V. Pen contributed to the knowledge of the physical model and Mr. Zhicheng Zhang contributed to the simulation. Dr. Guohua Cao supervised the study.

Chapter 4 is the extended version of the manuscript titled "A correction method for photon counting CT data distortion with deep learning neural network", which is still under preparation. As the first author of the manuscript, I contributed to the following aspects: the PCCT system simulation, data preparation, deep learning neural network design and implementation, network training and testing, and algorithm evaluation. Dr. Guohua Cao supervised the study.

1.6 Relevant publication

The following list shows the manuscripts published, accepted, reviewed, or prepared concurrently with this dissertation.

Journal Papers:

- S. Zhang, G. Geng, G. Guo, Y. Zhang, B. Liu, and **X. Dong**, "Fast Projection Algorithm for Lim-based Simultaneous Algebraic Reconstruction Technique and Its Parallel Implementation on GPU", IEEE Access, 2018.
- Z. Zhang, X. Liang, **X. Dong**, Y. Xie, and G. Cao, "A Sparse-View CT Reconstruction Method Based on Combination of DenseNet and Deconvolution", IEEE Trans. Med. Imaging, 2018.
- **X. Dong**, C. Chen, and G. Cao, "Improving Molecular Sensitivity in X-Ray Fluorescence Molecular Imaging (XFMI) of Iodine Distribution in Mouse-Sized Phantoms via Excitation Spectrum Optimization", IEEE Access, 2018.

- Z. Zhang, S. Yu, W. Qin, X. Liang, **X. Dong**, G. Cao, Y. Xie, "Super-resolution and deblur based iterative reconstruction (SADIR) for high-resolution CT," IEEE Trans. Med. Imaging, 2019. (Under Review)
- **X. Dong**, O. V. Pen, Z. Zhang, and G. Cao, "Improved material identification via accurate calculation of effective atomic number and electron density from photon counting CT images", Medical Physics, 2019. (Under Review)
- **X. Dong**, and G. Cao, "A correction method for photon counting CT data distortion with deep learning neural network" (Under Preparation)

Conference Papers:

- G. Cao, and **X. Dong**, "X-Ray Fluorescence Molecular Imaging with Improved Sensitivity for Biomedical Applications," 20th International Conference on Medical and Biomedical Engineering (ICMBE), 2018.
- Z. Zhang, **X. Dong**, S. Vekhande, and G. Cao, "A Deep Learning Based Reconstruction Method for Sparse-view CT, " 40th International Conference of the IEEE Engineering in Medicine and Biology Conference (EMBC), 2018.
- **X. Dong**, O. V. Pen, Z. Zhang, and G. Cao, "An improved physics model for multi-material identification in photon counting CT", International Society for Optics and Photonics (SPIE) Medical Imaging conference, 2019.
- **X. Dong**, S. Vekhande, and G. Cao, "Sinogram interpolation for sparse-view micro-CT with deep learning neural network," International Society for Optics and Photonics (SPIE) Medical Imaging conference, 2019.
- E. Z. Chen, **X. Dong**, J. Wu, H. Jiang, X. Li, and R. Rong, "Lesion attributes segmentation for melanoma detection with multi-task U-Net", IEEE International Symposium on Biomedical Imaging (ISBI), 2019.

Conference Abstracts:

- **X. Dong**, O. V. Pen, Z. Zhang, and G. Cao, "Material Identification from Spectral CT Using Effective Atomic Number and Electron Density", BMES annual conference, Atlanta, GA, 2018.
- **X. Dong**, O. V. Pen, Z. Zhang, and G. Cao, "Quantitative Imaging of Electron Density and Effective Atomic Number Using Spectral CT", BMES annual conference, Phoenix, AZ, 2017.
- **X. Dong**, and G. Cao, "Experimental Investigation of the Impact of Excitation Beam on Chemical Concentration Sensitivity for XFCT", BMES annual conference, Minneapolis, MN, 2016.

References

[1] J. Nelson, K. Rinard, A. Haynes, S. Filleur, and T. Nelius, "Extraluminal colonic carcinoma invading into kidney: A case report and review of the literature," *ISRN urology*, vol. 2011, 2011.

[2] W. A. Kalender, *Computed tomography: fundamentals, system technology, image quality, applications*. John Wiley & Sons, 2011.

[3] J. Hsieh, "Computed tomography: principles, design, artifacts, and recent advances," 2009: SPIE Bellingham, WA.

[4] A. M. Cormack, "Representation of a function by its line integrals, with some radiological applications. II," *Journal of Applied Physics*, vol. 35, no. 10, pp. 2908-2913, 1964.

[5] G. N. Hounsfield, "Computerized transverse axial scanning (tomography): Part 1. Description of system," *The British journal of radiology*, vol. 46, no. 552, pp. 1016-1022, 1973.

[6] M. J. Budoff, "Computed Tomography: Overview," in *Cardiac CT Imaging*: Springer, 2010, pp. 3-20.

[7] W. contributors. (2019, 14 March). *Tomographic reconstruction*. Available: https://en.wikipedia.org/w/index.php?title=Tomographic_reconstruction&oldid=886958910

[8] G. L. Zeng, *Medical image reconstruction: a conceptual tutorial*. Springer, 2010.

[9] E. C. Beckmann, "CT scanning the early days," *The British journal of radiology*, vol. 79, no. 937, pp. 5-8, 2006.

[10] R. E. Alexander and R. B. Gunderman, "EMI and the first CT scanner," *Journal of the American College of Radiology*, vol. 7, no. 10, pp. 778-781, 2010.

[11] E. M. Haacke, R. W. Brown, M. R. Thompson, and R. Venkatesan, *Magnetic resonance imaging: physical principles and sequence design*. Wiley-Liss New York:, 1999.

[12] D. L. Bailey, M. N. Maisey, D. W. Townsend, and P. E. Valk, *Positron emission tomography*. Springer, 2005.

[13] R. J. English and S. E. Brown, "SPECT single photon emission computed tomography: A primer," 1986.

[14] R. Weissleder and M. J. Pittet, "Imaging in the era of molecular oncology," (in English), *Nature*, vol. 452, no. 7187, pp. 580-589, Apr 3 2008.

[15] R. Weissleder and V. Ntziachristos, "Shedding light onto live molecular targets," *Nature Medicine*, vol. 9, no. 1, pp. 123-128, Jan 2003.

[16] F. A. Jaffer and R. Weissleder, "Molecular imaging in the clinical arena," (in English), *Journal of the American Medical Association*, vol. 293, no. 7, pp. 855-862, Feb 16 2005.

[17] M. Thakur and B. C. Lentle, "Report of a summit on molecular imaging," *Radiology*, vol. 236, no. 3, pp. 753-755, 2006.

[18] W. Han, J. A. Eichholz, J. Huang, and J. Lu, "RTE-based bioluminescence tomography: a theoretical study," *Inverse Problems in Science and Engineering*, vol. 19, no. 4, pp. 435-459, 2011.

[19] R. Weissleder, "Molecular Imaging in Cancer," *Science*, vol. 312, p. 26, 2006.

[20] M. A. Pysz, S. S. Gambhir, and J. K. Willmann, "Molecular imaging: current status and emerging strategies," (in eng), *Clinical radiology*, Research Support, N.I.H., Extramural Research Support, Non-U.S. Gov't Review vol. 65, no. 7, pp. 500-16, Jul 2010.

[21] G. Cao, J. Lu, and O. Zhou, "X-ray fluorescence molecular imaging with high sensitivity: feasibility study in phantoms," in *SPIE Medical Imaging*, 2012, pp. 83130S-83130S-6: International Society for Optics and Photonics.

[22] J. Bryant, N. Drage, and S. Richmond, "CT number definition," *Radiation Physics and Chemistry*, vol. 81, no. 4, pp. 358-361, 2012.

[23] K. Taguchi and J. S. Iwanczyk, "Vision 20/20: Single photon counting x‐ray detectors in medical imaging," *Medical physics,* vol. 40, no. 10, 2013.
[24] A. Simionovici *et al.*, "High-resolution x-ray fluorescence microtomography of homogeneous samples," *IEEE Transactions on Nuclear Science,* vol. 47, no. 6, pp. 2736-2740, 2000.
[25] W. Cong, H. Shen, and G. Wang, "Spectrally resolving and scattering-compensated x-ray luminescence/fluorescence computed tomography," *Journal of biomedical optics,* vol. 16, no. 6, pp. 066014-066014-7, 2011.
[26] K. Ricketts *et al.*, "A quantitative x-ray detection system for gold nanoparticle tumour biomarkers," *Phys Med Biol,* vol. 57, no. 17, pp. 5543-55, Sep 07 2012.
[27] B. L. Jones, N. Manohar, F. Reynoso, A. Karellas, and S. H. Cho, "Experimental demonstration of benchtop x-ray fluorescence computed tomography (XFCT) of gold nanoparticle-loaded objects using lead- and tin-filtered polychromatic cone-beams," *Phys Med Biol,* vol. 57, no. 23, pp. N457-67, Dec 07 2012.
[28] Y. Kuang, G. Pratx, M. Bazalova, B. Meng, J. Qian, and L. Xing, "First demonstration of multiplexed x-ray fluorescence computed tomography (XFCT) imaging," *IEEE transactions on medical imaging,* vol. 32, no. 2, pp. 262-267, 2013.
[29] M. Ahmad, M. Bazalova, L. Xiang, and L. Xing, "Order of magnitude sensitivity increase in X-ray Fluorescence Computed Tomography (XFCT) imaging with an optimized spectro-spatial detector configuration: theory and simulation," *IEEE Trans Med Imaging,* vol. 33, no. 5, pp. 1119-28, May 2014.
[30] L. Ren, D. Wu, Y. Li, G. Wang, X. Wu, and H. Liu, "Three-dimensional x-ray fluorescence mapping of a gold nanoparticle-loaded phantom," *Med Phys,* vol. 41, no. 3, p. 031902, Mar 2014.
[31] M. Ahmad, M. Bazalova-Carter, R. Fahrig, and L. Xing, "Optimized Detector Angular Configuration Increases the Sensitivity of X-ray Fluorescence Computed Tomography (XFCT)," *IEEE Trans Med Imaging,* vol. 34, no. 5, pp. 1140-7, May 2015.
[32] C. Yoon, Y. Kim, and W. Lee, "3D Non-Destructive Fluorescent X-Ray Computed Tomography With a CdTe Array," *IEEE Transactions on Nuclear Science,* vol. 63, no. 3, pp. 1844-1853, 2016.
[33] D. Wu *et al.*, "Measurements of gold nanoparticle concentration with K-shell x-ray fluorescence spectrum," in *Proc. of SPIE Vol*, 2017, vol. 10065, pp. 100650M-1.
[34] S. Zhang, L. Li, and Z. Chen, "XFCT imaging system with pinhole collimation and attenuation correction," in *Nuclear Science Symposium, Medical Imaging Conference and Room-Temperature Semiconductor Detector Workshop (NSS/MIC/RTSD), 2016*, 2016, pp. 1-4: IEEE.
[35] T. Sasaya *et al.*, "Preliminary study on X-ray fluorescence computed tomography imaging of gold nanoparticles: Acceleration of data acquisition by multiple pinholes scheme," *Nuclear Instruments and Methods in Physics Research Section A: Accelerators, Spectrometers, Detectors and Associated Equipment,* 2017.
[36] L. Li, S. Zhang, R. Li, and Z. Chen, "Full-field fan-beam x-ray fluorescence computed tomography with a conventional x-ray tube and photon-counting detectors for fast nanoparticle bioimaging," *Optical Engineering,* vol. 56, no. 4, p. 043106, 2017.
[37] Z. Yu *et al.*, "Evaluation of conventional imaging performance in a research whole-body CT system with a photon-counting detector array," *Physics in Medicine & Biology,* vol. 61, no. 4, p. 1572, 2016.
[38] X. Wang, A. Zamyatin, and D. Shi, "Dose reduction potential with photon counting computed tomography," in *Medical Imaging 2012: Physics of Medical Imaging*, 2012, vol. 8313, p. 831349: International Society for Optics and Photonics.

[39] P. M. Shikhaliev and S. G. Fritz, "Photon counting spectral CT versus conventional CT: comparative evaluation for breast imaging application," *Physics in Medicine & Biology,* vol. 56, no. 7, p. 1905, 2011.
[40] M. J. Willemink, M. Persson, A. Pourmorteza, N. J. Pelc, and D. Fleischmann, "Photon-counting CT: technical principles and clinical prospects," *Radiology,* vol. 289, no. 2, pp. 293-312, 2018.
[41] F. E. Boas and D. Fleischmann, "CT artifacts: causes and reduction techniques," *Imaging in Medicine,* vol. 4, no. 2, pp. 229-240, 2012.
[42] A. Pourmorteza *et al.*, "Abdominal imaging with contrast-enhanced photon-counting CT: first human experience," *Radiology,* vol. 279, no. 1, pp. 239-245, 2016.
[43] J. S. Butzer, A. P. H. Butler, P. H. Butler, P. J. Bones, N. Cook, and L. Tlustos, "Medipix imaging - evaluation of datasets with PCA," in *2008 23rd International Conference Image and Vision Computing New Zealand*, 2008, pp. 1-6.
[44] X. Wang, D. Meier, K. Taguchi, D. J. Wagenaar, B. E. Patt, and E. C. Frey, "Material separation in x‐ray CT with energy resolved photon‐counting detectors," *Medical physics,* vol. 38, no. 3, pp. 1534-1546, 2011.
[45] S. Leng *et al.*, "Spectral performance of a whole-body research photon counting detector CT: quantitative accuracy in derived image sets," *Physics in Medicine & Biology,* vol. 62, no. 17, p. 7216, 2017.
[46] K. C. Zimmerman and T. G. Schmidt, "Experimental comparison of empirical material decomposition methods for spectral CT," (in English), *Physics in Medicine and Biology,* vol. 60, no. 8, pp. 3175-3191, Apr 21 2015.
[47] Z. Li, S. Leng, L. Yu, Z. Yu, and C. H. McCollough, "Image-based material decomposition with a general volume constraint for photon-counting CT," in *Medical Imaging 2015: Physics of Medical Imaging*, 2015, vol. 9412, p. 94120T: International Society for Optics and Photonics.
[48] R. Symons *et al.*, "Photon‐counting CT for simultaneous imaging of multiple contrast agents in the abdomen: an in vivo study," *Medical physics,* vol. 44, no. 10, pp. 5120-5127, 2017.
[49] L. I. R. Garcia, J. F. P. Azorin, and J. F. Almansa, "A new method to measure electron density and effective atomic number using dual-energy CT images," *Physics in Medicine & Biology*, vol. 61, no. 1, p. 265, 2015.
[50] D.-H. Kim, W.-H. Lee, S.-S. Jeon, and H.-J. Kim, "Absolute measurement of the effective atomic number and the electron density by using dual-energy CT images," *Journal of the Korean Physical Society,* vol. 61, no. 12, pp. 2042-2048, 2012.
[51] K. Ogawa, T. Hirokawa, and S. Nakamura, "Identification of a material with a photon counting x-ray CT system," in *Nuclear Science Symposium Conference Record (NSS/MIC), 2010 IEEE*, 2010, pp. 2582-2586: IEEE.
[52] P. Babaheidarian and D. Castañón, "Feature selection for material identification in spectral ct," *Electronic Imaging,* vol. 2018, no. 15, pp. 134-1-1346, 2018.
[53] A. M. Alessio and L. R. MacDonald, "Quantitative material characterization from multi‐energy photon counting CT," *Medical physics,* vol. 40, no. 3, p. 031108, 2013.
[54] J. Cammin, S. G. Kappler, T. Weidinger, and K. Taguchi, "Evaluation of models of spectral distortions in photon-counting detectors for computed tomography," *Journal of Medical Imaging,* vol. 3, no. 2, p. 023503, 2016.
[55] X. Dong, O. V. Pen, Z. Zhang, and G. Cao, "An improved physics model for multi-material identification in photon counting CT," in *Medical Imaging 2019: Physics of Medical Imaging*, 2019, vol. 10948, p. 109484O: International Society for Optics and Photonics.

[56] X. Dong, C. Chen, and G. Cao, "Improving Molecular Sensitivity in X-Ray Fluorescence Molecular Imaging (XFMI) of Iodine Distribution in Mouse-Sized Phantoms via Excitation Spectrum Optimization," *IEEE Access,* vol. 6, pp. 56966-56976, 2018.

Chapter 2 X-ray fluorescence molecular imaging

Xu Dong[1], Cheng Chen[2], and Guohua Cao[1]

[1]Department of Biomedical Engineering and Mechanics, Virginia Polytechnic Institute and State University, Blacksburg, VA 24061, USA.

[2]Department of Mining and Minerals Engineering, Virginia Polytechnic Institute and State University, Blacksburg, VA 24061, USA.

Publication information – The major contents of this chapter were published as: X. Dong, C. Chen, and G. Cao, "Improving Molecular Sensitivity in X-Ray Fluorescence Molecular Imaging (XFMI) of Iodine Distribution in Mouse-Sized Phantoms via Excitation Spectrum Optimization," IEEE Access, vol. 6, pp. 56966-56976, 2018.

2.1 Abstract

X-ray fluorescence molecular imaging (XFMI) has shown great promise as a low-cost molecular imaging modality for clinical and pre-clinical applications with high sensitivity. Recently, progress has been made in enabling the XFMI technique with laboratory x-ray sources for various biomedical applications. However, the sensitivity of XFMI still needs to be improved for in vivo biomedical applications at a reasonably low radiation dose. In laboratory x-ray source-based XFMI, the main factor that limits the molecular sensitivity of XFMI is the scatter x-rays that coincide with the fluorescence x-rays from the targeted material. In this paper, we experimentally investigated the effects of excitation beam spectrum on the molecular sensitivity of XFMI, by quantitatively deriving minimum detectable concentration (MDC) under a fixed surface entrance dose of 200 mR at three different excitation beam spectra. XFMI experiments were carried out on two customized mouse-sized phantoms. The result shows that the MDC can be readily increased by a factor

of 5.26 via excitation spectrum optimization. Furthermore, a numerical model was developed and validated by the experimental data. The numerical model can be used to optimize XFMI system configurations to further improve the molecular sensitivity. Findings from this investigation could find applications for in vivo pre-clinical small-animal XFMI in the future.

Keywords: Molecular imaging, X-ray fluorescence, Molecular sensitivity

2.2 Introduction

X-ray Fluorescence Molecular Imaging (XFMI) as an imaging technique for elemental mapping or bio-distribution studies of a target molecule in a biological body has a great potential for applications in personal or precision medicine for many diseases such as cancers. XFMI utilizes the secondary x-ray fluorescence signal to map out the distribution information of specific elements. In XFMI, external x-rays are used to produce the secondary fluorescence x-rays via the interactions between the excitation x-ray photons and the target elements in the imaged object. Because the energies of the generated fluorescence x-ray photons are characteristic to the target elements, the spatial distribution of individual element species can be derived from their corresponding x-ray fluorescence signals.

The XFMI technique was first investigated for biological applications by Ahlgren et al. in 1976 by measuring lead in organs near the skin's surface using a synchrotron source [1]. Since then, the synchrotron-based XFMI technique has been widely investigated over the past decades for different biomedical applications [2-5]. The combination of XFMI technique with other imaging modalities has been investigated recently. For example, the combination of XFMI and micro-Computed Tomography (micro-CT) has been demonstrated in 2000 [6]. More recently, the XFMI technique has been adopted to quantitatively detect novel imaging contrast agents, such as nanoparticles based on iodine and gold, at low concentrations for specific biological purposes. Examples include the XFMI imaging of gold nanoparticle-based contrast agent to detect tumor locations [7, 8], and the XFMI imaging of iodine perfusion in a mouse brain [9]. All these experiments

employed monochromatic x-rays generated by the synchrotron sources. However, due to the limited availability and the high cost of synchrotron radiations, synchrotron-based XFMI technique has not been widely applied to clinical or pre-clinical research.

The feasibility of XFMI technique using laboratory x-ray sources was demonstrated rather recently in 2010 [10]. Enabling XFMI with conventional x-ray sources gives the technique a big boost to its potential in routine clinical or pre-clinical applications. In the past a few years, several studies have been conducted to examine the feasibility of enabling XFMI using conventional x-ray sources [11-19] [[20-22]. For instances, Jones et al. successfully built a benchtop cone beam x-ray fluorescence CT system in 2012 [13], Kuang et al. utilized the XFMI technique to trace the distributions of three different elements simultaneously in 2013 [14], Ren et al. implemented a pixel-mapping based XFMI for element analysis in 2014 [16], Yoon et al. developed a three dimension fluorescence CT system with CdTe detector array in 2016 [18], and Li et al. designed a full-field fan-beam x-ray fluorescence CT system in 2017 [22]. Most of the XFMI techniques utilized the K-shell fluorescence signals to obtain the element distribution, but XFMI using the L-shell fluorescence signals has also been investigated [23-25].

To adopt XFMI for biological applications, a main research focus is to increase molecular sensitivity at a biologically acceptable radiation dose. The sensitivity of the XFMI technique depends on a number of factors, including the targeted contrast agent, excitation x-ray spectrum, and acquisition geometry. XFMI imaging at different acquisition configurations has been investigated in several recent studies [11-19]. For imaging contrast agent, iodine [26, 27] and gold nanoparticles [28, 29] has been more extensively investigated because of their suitable x-ray fluorescence energies, high x-ray fluorescence yield, and good biochemical properties. A comprehensive comparison of different materials as XFMI contrast agents for biological applications can be found in the reference [30].

One of the main factors that determine the molecular sensitivity in laboratory x-ray source based XFMI is the scatter x-ray background from the interactions between a polychromatic excitation x-ray beam and the imaged object. Many methods have been proposed to overcome the interfering scatter background x-ray photons. For example, the detector is

typically placed perpendicular to the direction of the excitation x-ray beam to minimize the amount of scatter x-ray photons reaching the detector [31], and detector collimators are usually used to further reject the number of scatter photons reaching the detector [32]. Various data processing techniques based on curve fitting and statistical modeling have also been applied to subtract the scatter background x-ray photons [12, 25].

Another effective way to improve the molecular sensitivity of XFMI with laboratory x-ray sources is via optimizing the spectrum of the excitation x-ray beam [26, 33]. An intuitive explanation is that the scatter x-ray photons at the characteristic x-ray fluorescence energies of the targeted element would obscure the detected x-ray fluorescence peaks, resulting in lower XFMI sensitivity. Therefore, optimizing the excitation beam spectrum with a goal of suppressing the number of scatter photons at the characteristic x-ray fluorescence energies of the targeted element can be a viable strategy for improving molecular sensitivity for XFMI. For example, in a previous work we demonstrated that the molecular sensitivity in the XFMI of iodine-based contrast agent using a bremsstrahlung x-ray source can be improved via excitation spectrum optimization with simple x-ray filtrations [26]. However, a systematic and quantitative investigation on how the molecular sensitivity of XFMI depends on different spectra of the excitation beam has not been carried out, especially in the configuration of small animal XFMI.

XFMI of small animals, particularly mice and rats, will be valuable for many basic and preclinical studies for understanding the pathophysiology of disease [34, 35] and developing new drug candidates for cancer and cardiovascular disorders [36, 37]. This is especially true with the development of gene knockout and transgenic technologies. In this paper, we report our systematic and quantitative experimental investigations on improving the molecular sensitivity in XFMI of iodine distribution in mouse-sized phantoms via excitation spectrum optimization, with the goal of applying this technique for *in vivo* small-animal XFMI. Furthermore, we developed an XFMI simulation model and validated the model by the experimental data.

The chapter is organized as follows. After the introduction, in Section 2.3 we describe our experiments and methods, which contain the experimental setup, the data processing

methods, and the XFMI system simulation. The results are shown in Section 2.4, followed by the discussions and conclusions in Section 2.5.

2.3 Methods

2.3.1 Theoretical model

In an XFMI system, an object is excited by an external primary x-ray beam, as shown in Figure 2.1. The fluorescence signal could be generated only by those x-ray photons with energy higher than the K-edge energy (E_k) of the targeted element in the object. For iodine, $E_k = 33.2\ keV$. As a result, the number of fluorescence photons that are generated by an excitation x-ray beam at an interaction pixel is calculated as:

$$N_{fl} = \int_{E_k}^{E_{max}} \eta N_{(E)} \left(1 - exp(-\mu_{pe_{(E)}} * c * d)\right) dE \tag{2.1}$$

where $N_{(E)}$ is the number of x-ray photons at energy E for a given excitation spectrum, $\mu_{pe_{(E)}}$is the photoelectric attenuation coefficient of the interacting material at energy E, c is the element molecular concentration, d is the attenuating length of the pixel, and η is the fluorescence yield of the target element. For iodine K shell, η is 0.884.

Considering that the fluorescence x-ray detector in the XFMI system is well collimated by a detector collimator, only a small portion of the generated fluorescence x-ray photons in a certain solid angle that is determined from the acquisition geometry can reach the fluorescence x-ray detector. As a result, the measured number of fluorescence x-ray photons at the detector is:

$$N_{fl}^{measure} = \frac{1}{4\pi} * \int N_{fl} d\Omega = \frac{1}{2} \int_{\theta_d - \frac{\Delta\theta}{2}}^{\theta_d + \frac{\Delta\theta}{2}} N_{fl} \sin(\theta)\, d\theta \tag{2.2}$$

where θ_d is the angle between the excitation beam and the detector line of sight, which is 90 degree in our experimental setup, and $\Delta\theta$ is the angular range subtended by the x-ray

detector sensor area after the detector collimation. The detailed geometrical illustration is shown in Figure 2.1(B).

For the Rayleigh scatter, only those Rayleigh scatter x-ray photons with energy near the fluorescence peak energy (E_p) will interfere with the fluorescence signal measurement. Suppose the interfering Rayleigh scatter x-ray photon energy (E) ranges from [$E_p - \frac{\Delta E}{2}$, $E_p + \frac{\Delta E}{2}$] (which happens to be the fluorescence peak energy range), the number of measured Rayleigh scatter x-ray photons can be calculated in a similar way:

$$N_{rs}^{measure} = \frac{1}{4\pi} * \int N_{rs} d\Omega = \frac{1}{2} \int_{\theta_d - \frac{\Delta\theta}{2}}^{\theta_d + \frac{\Delta\theta}{2}} \int_{E_p - \frac{\Delta E}{2}}^{E_p + \frac{\Delta E}{2}} N_{(E)} \left(1 - exp(-\mu_{rs_{(E)}} * d)\right) dE \, sin(\theta) \, d\theta \quad (2.3)$$

where $\mu_{rs_{(E)}}$ is the Rayleigh scatter attenuation coefficient of the interacting material at energy E.

For the Compton scatter, the energy of the x-ray photon will change by the Compton scatter interaction, as a result, the number of measured Compton scatter x-ray photons can be calculated as:

$$N_{cs}^{measure} = \frac{1}{4\pi} * \int N_{cs} d\Omega = \frac{1}{2} \int_{\theta_d - \frac{\Delta\theta}{2}}^{\theta_d + \frac{\Delta\theta}{2}} \int_{E_1}^{E_2} N_{(E)} \left(1 - exp\left(-\mu_{cs_{(E)}} * d\right)\right) dE \, sin(\theta) \, d\theta \quad (2.4)$$

where $\mu_{cs_{(E)}}$ is the Compton scattering attenuation coefficient at the interacting x-ray energy (E).The integration energy range [E_1, E_2] is the energy range for the excitation beam x-ray energy (E) before Compton scattering, which corresponds to the interfering Compton scatter x-ray photon energy (E') ranging from [$E_p - \frac{\Delta E}{2}$, $E_p + \frac{\Delta E}{2}$]. The relationship between the Compton scatter x-ray photon energy (E') and the excitation x-ray photon energy (E) is governed by the following equation:

$$E = E' \frac{511\ keV}{511\ keV - E'(1 - cos\,\theta)} \quad (2.5)$$

Therefore, the total number of measured x-ray photons at the fluorescence x-ray energy range [$E_p - \Delta E/2$, $E_p + \Delta E/2$] in the XFMI setup illustrated in Figure 2.1 is:

$$N^{measure} = N_{fl}^{measure} + N_{rs}^{measure} + N_{cs}^{measure} \tag{2.6}$$

2.3.2 Experimental setup

To investigate the effects of the excitation beam spectra on the molecular sensitivity of XFMI systems, we developed a bench-top XFMI setup using a laboratory bremsstrahlung x-ray source. A picture of the XFMI setup is shown in Figure 2.1(A). It consists of a conventional x-ray source, a source beam filter, a source collimator, a mouse-sized phantom, and an energy-sensitive x-ray spectrometer with collimator. The XFMI geometry parameters and the experimental parameters are listed in Table 2.1.

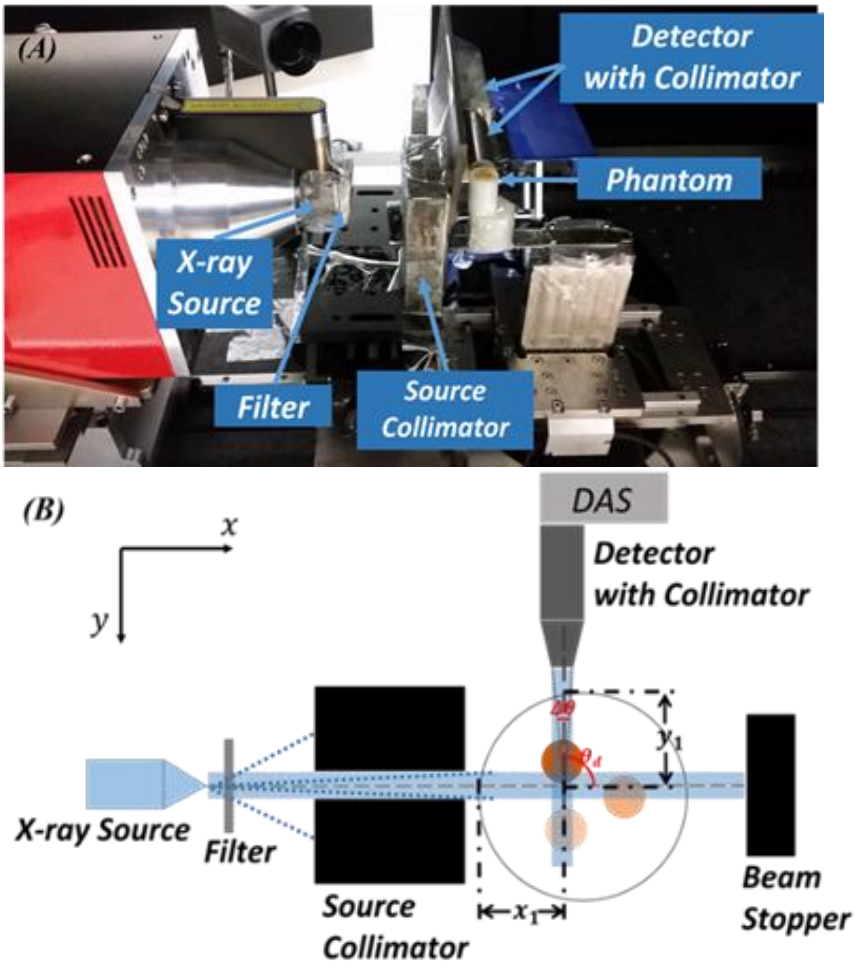

Figure 2.1: (A) The picture XFMI experimental system. (B) The schematic of XFMI system.

2.3.2A X-ray source and filters

A commercially available x-ray source (Thermo Kevex x-ray) was operated at 40 kV. It has a tungsten anode. A filter was placed near the x-ray source's exit window to shape the excitation x-ray beam spectrum. Different filter choices (materials and thickness) can lead to different excitation spectra. Three different filter choices were used in this study. They are 1.02 mm Copper, 5.20 mm Aluminum, and 2.08 mm Aluminum. The spectra of the excitation x-ray beam after different filters were measured experimentally by placing the detector along the excitation beam path. And the experimentally measured excitation spectra were further validated with the simulations by the SpekCalc program [38].

As shown in Figure 2.1, a source collimator was placed between the source filter and the object to shape the excitation x-ray beam into a pencil x-ray beam. The source collimator is made of alloy steel with a thickness of 3 cm and the aperture size of the collimator is 3 mm. This source collimator makes the cross section size of pencil beam passing through the object to be around 3 mm when the object is placed right next to the collimator.

Table 2.1: Parameters of the XFMI experiments.

Source to Object Distance	45 mm
Object to Detector Distance	30 mm
Collimators Aperture Size	3 mm
Phantom Diameter	20 mm
Phantom Vial Size	3 mm
Translational Step Size	3 mm
Source Voltage	40 kV
Radiation Dose Level	2 mGy for calibration phantom 5 mGy for contrast phantom

2.3.2B X-ray detector

The signals were detected by a CdTe detector (X-123CdTe, Amptek Inc). The detected signals were connected with a computer to collect and analyze the data. For this study, the detector was calibrated to collect x-ray photons from 0 keV to 43.73 keV with 2048 channels, resulting in the energy bin width of 21.35 eV per channel in the measured spectrum.

The detected x-rays consisted of the desired fluorescence x-ray photons from iodine and the undesired background x-ray photons which are mainly caused by the Compton

scattering of the excitation x-ray photons. To minimize the number of Compton scatter x-ray photons reaching the x-ray detector, the detector was mounted at 90-degree to the excitation x-ray beam and installed with a detector collimator.

The detector collimator was placed in front of the x-ray detector to minimize the scatter x-ray photons that reach the detector. The wall thickness of the detector collimator is 2.5 cm, and its aperture size is 3 mm as well, which restricts the detector line of sight to be around 3 mm at its cross section (see Figure 2.1). Under such geometry, only the x-ray photons originated from the pixel formed by the intersection of the excitation pencil x-ray beam and the detector line of sight can reach the x-ray detector. The pixel size from this collimation configuration is therefore 3 mm × 3 mm × 3 mm.

2.3.2C Imaging phantom

Two mouse-sized phantoms were built for this study. Their illustrations are shown in Figure 2.2. Both phantoms are made of 20-mm-diameter cylinders with the material of the phantoms as polymethyl methacrylate (PMMA). One is a calibration phantom (Figure 2.2(A)), and the other is a contrast phantom (Figure 2.2(B)).

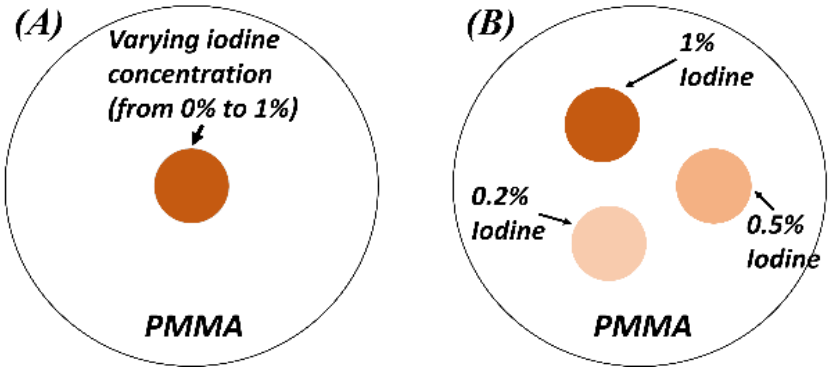

Figure 2.2: Schematics of the customized phantoms. (A) Calibration phantom with a single vial at the center. Different iodine solution with concentration of 1%, 0.5%, 0.25%, 0.167%, 0.125%, 0.1% and 0% (pure water) was inserted into the vial during each experiment. (B) The Contrast phantom with three vials filled with iodine solutions of different concentrations.

The calibration phantom contains a single 3-mm-diameter vial at its isocenter, which is filled with iodine solution of varying concentrations to find out the Minimum Detectable Concentration (MDC). In the calibration phantom study, the XFMI system is fixed and only the center voxel of the phantom, which corresponds to the center vial containing the iodine solution, was imaged. All the three filter options (1.02 mm Copper, 5.20 mm

Aluminum, and 2.08 mm Aluminum) were used to generate three different excitation beam spectra. The phantom was aligned with the excitation beam path and the detector line of sight in such a way that only the signal generated from the vail containing iodine solutions was able to reach the detector. For each excitation x-ray beam spectrum, a series of iodine solutions with concentrations at 1%, 0.5%, 0.25%, 0.167%, 0.125%, 0.1% and 0% (pure water) by weight (wt.), respectively, were inserted into the vial, and the resulted iodine fluorescence x-ray signals were measured at a fixed surface entrance dose of 2 mGy. The series of measurements are used to derive the MDC for each excitation x-ray beam spectrum.

The contrast phantom contains three vials, which are filled with three iodine solutions at different concentrations to investigate the imaging contrast and the system linearity. All vials have a diameter of 3 mm. Iodine solutions with the concentrations of 1%, 0.5%, and 0.2% were inserted into the three vials, respectively. In the contrast phantom study, translational stepping movements of the detector and the phantom in the x and the y directions respectively were made to collect signals, which will finally result in an XFMI signal image in the dimension of 7 pixels by 7 pixels covering the whole contrast phantom. The accurate stepping movements were achieved by the linear stage. The generated XFMI signal image after data processing can be used to reflect the iodine distribution in the contrast phantom. The surface entrance dose level was set to be 5 mGy. And the contrast phantom was imaged only by the two excitation spectra generated by the two Aluminum filter options (5.20 mm Aluminum and 2.08 mm Aluminum), mainly because of the long exposure time required to obtain the desired dose level when using the Copper filter.

2.3.2D Exposure time and radiation dose

In this study, the surface entrance dose was fixed at 2 mGy for the experiments with the calibration phantom, and 5 mGy for the experiments with the contrast phantom. To achieve the desired radiation dose, the exposure time (T) for different excitation spectrum was accordingly determined based on the characteristic dose factor (Γ) as the following:

$$T = \frac{D * d^2}{\Gamma * I} \tag{2.7}$$

where D is the dose level, d is the distance between the source and the imaged object, I is the x-ray source current, and Γ is the characteristic dose factor for a given excitation spectrum, which is calculated using the SpekCalc program [38]. The exposure time for each experiment is listed in Table 2.2.

Table 2.2: The exposure time for each experiment.

Different Excitation Spectra Group:	Characteristic Dose Factor ($\mu Gy/mA * s$ @ 1 meter)	X-ray Source Current Setup (mA)	Exposure Time for the Calibration Phantom [a] (sec.)	Exposure Time for the Contrast Phantom [b] (sec.)
1.02mm Cu filter:	0.009517	0.200	2127	N/A
5.20mm Al filter:	5.165561	0.010	78	196
2.08mm Al filter:	23.47016	0.005	34	86

To achieve a moderate and feasible exposure time for all the experiment, we used different x-ray source currents for different excitation spectra.
[a]For the calibration phantom (Figure 2.2(A)), the dose level is set to be 2 mGy.
[b]For the contrast phantom (Figure 2.2(B)), the dose level is set to be 5 mGy. And the copper filter is not used for the experiment.

2.3.3 Data processing

2.3.3A Extraction of fluorescence signal

Figure 2.3 shows an example of the *measured x-ray fluorescence signals* collected by the Amptek detector from the XFMI setup described in Section 2.3.2. The iodine x-ray

fluorescence signal contains two iodine fluorescence peaks, namely the k_α peak and the k_β peak. The centers of the two peaks are located at 28.6 keV and 32.3 keV, respectively. We set the window width for both fluorescence peaks at 2 keV in our data processing procedure. Therefore, the energy range from 27.6 keV to 29. 6 keV was considered as the k_α *fluorescence peak energy range*, and the energy range from 31.3 keV to 33.3 keV was considered as the k_β fluorescence peak energy range. All the other data outside the two fluorescence peak energy ranges were considered the *off-peak energy range* data.

The first step in extracting the *net fluorescence signal* from a measured x-ray fluorescence signal is to find out the *scatter background signals* in the fluorescence peak energy ranges. For the off-peak energy range data, a ten-order polynomial least squares fit was applied to obtain the *off-peak background fit*. Then, the scatter background signals within the fluorescence peak energy ranges were obtained by the ten-order polynomial interpolations of the off-peak background fit. The interpolated scatter background signals (denoted as bg) were subtracted from the measured x-ray fluorescence signals at the fluorescence peak energy range to obtain the *net fluorescence signal*. In this study, we only used iodine fluorescence signal at the k_α peak, because the intensity of the k_β peak is barely visible in our low dose experiments.

After obtaining the net iodine fluorescence signal, it was fit with a Gaussian curve. The height (denoted as h) of the fitted Gaussian curve was taken as the *strength* of the net fluorescence signal, and hereafter it is referred as the *fluorescence peak height*. An illustration of the procedure for extracting fluorescence signal is illustrated in Figure 2.3.

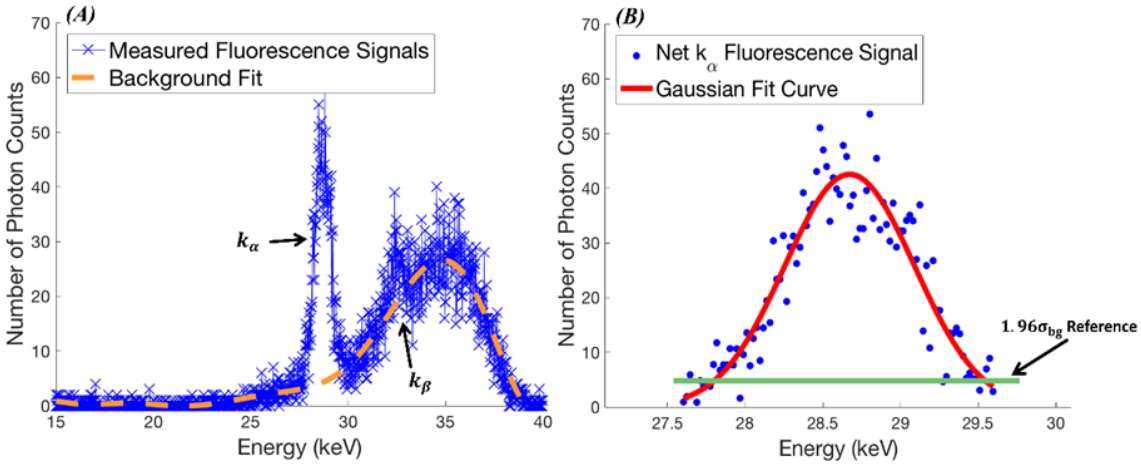

Figure 2.3: Illustration of the procedure for extracting net fluorescence signals. (A) Scatter background interpolation. The blue curve is the measured iodine fluorescence signal and the dashed orange line is the ten-order polynomial background fit from the off-peak range data. (B) Isolation of the net fluorescence signal. The blue dots represent the extracted net iodine k_α fluorescence signal, and the red curve is its Gaussian fit. The green line represents the reference level at $1.96\sigma_{bg}$.

2.3.3B Minimum detectable concentration

In this study, the Minimum Detectable Concentration (MDC) is used to characterize the molecular sensitivity of a XFMI system, which is a measure of the capability of the system to distinguish a net fluorescence signal (the fluorescence peak height (h)) from the random fluctuations of the background signal (bg). The random fluctuations of the background signal can be characterized by the background noise (σ_{bg}), which was treated as the mean of all the deviations between the experimentally measured data points and the fitted background values at the off-peak energy range. To be treated as distinguishable from the background fluctuations with 95% confidence level, the fluorescence peak height (h) must be larger than $1.96\sigma_{bg}$. In the calibration phantom study, a least squares linear fit was applied to the fluorescence peak heights (h) obtained at various iodine concentrations. Then the MDCs from different excitation spectra are determined by the intersecting points between the linear fit lines and the $1.96\sigma_{bg}$ reference lines, as shown in Figure 2.3(B).

2.3.3C Attenuation correction

In the contrast phantom study, to generate a whole XFMI signal image, attenuation corrections must be performed to the net fluorescence signal obtained via the procedure described in the above section. As shown in Figure 2.1(B), before the primary excitation beam reaches a pixel in the object, it experiences the attenuation by the path length x_1. Similarly, the generated secondary x-ray beam would also be attenuated by the path length y_1 before it could reach the detector. To ensure that the XFMI signal is proportional to the iodine concentration at each pixel location, the variation of primary beam attenuation and the secondary beam attenuation at different pixel location has to be corrected.

Henceforth, the attenuation correction factor (C) is calculated as:

$$C = exp\left(\int_0^{x_1} \mu_p(x)dx + \int_0^{y_1} \mu_p'(y)dy\right) \tag{2.8}$$

where x_1 and y_1 are the attenuation path length of the primary beam and the secondary beam, respectively, as illustrated in the Figure 2.1(B), and $\mu_p(x)$ and $\mu_p'(y)$ are the attenuation coefficients of the material along the paths of the primary beam and the secondary beam, correspondingly.

Considering the facts that the highest iodine concentration is 1.0% in our study and the attenuation coefficient of PMMA is similar to water, the calculation of the attenuation correction factor could be greatly simplified. Equation (2.2) can be simplified as:

$$C = exp(\mu_w * x_1 + \mu_w' * y_1) \tag{2.9}$$

where μ_w and μ_w' are the attenuation coefficients of water at the effective x-ray energy levels for the primary beam and the secondary beam, respectively. The secondary x-ray beam has an effective x-ray energy at the iodine fluorescence x-ray energy (28.6 keV). For the primary x-ray beam, only those x-ray photons with energies above 33.2 keV (the iodine K edge energy) in the excitation beam spectrum have the capability to excite the iodine atom to generate fluorescence x-rays.

Therefore, the effective energy ($\tilde{E}$) for the primary beam can be calculated by the following equation:

$$\tilde{E} = \frac{\int_{E=33.2keV}^{E=40keV} E \times w(E)\, dE}{\int_{E=33.2keV}^{E=40keV} w(E)\, dE} \tag{2.10}$$

where $w(E)$ is the distribution of excitation x-ray beam at the energy E in the normalized excitation spectrum.

Finally, the fluorescence peak height (h) produced by the procedure described in the above Section 2.3.3A was multiplied by the attenuation correction factor (C) to obtain the XFMI signal. The final XFMI images were generated for the contrast phantom under two excitation spectra.

2.3.4 XFMI system simulation

Based on the theoretical model in Appendix, we can computationally simulate an XFMI system and calculate *the number of the generated fluorescence photons (n)* for a given XFMI system setup. We implemented the simulation program in Matlab to simulate the physical experiments using the same system geometrical protocol as described in Section 2.3.2.

We used the calibration phantom (Figure 2.2(A)) in our simulation and calculated the number of generated fluorescence photons (k_α peak) for the three excitation spectra (1.02 mm Cu filter, 5.20 mm Al filter, and 2.08 mm Al filter) at a fixed dose level of 2 mGy. For the inserted iodine solution in the calibration phantom, we used a same series of iodine concentrations as we used in the experiment, which are1%, 0.5%, 0.25%, 0.167%, 0.125%, 0.1% and 0% (pure water) by weight (wt.)

To compare the simulation data with experimental data, we calculated the summation of net fluorescence signal for the k_α fluorescence peak energy range and the sum was considered the number of generated fluorescence photons corresponding to that obtained in the experiment. The comparison of the simulation data with the experimental data is plotted in Figure 2.8. The Pearson Correlation Coefficient (PCC) is calculated between the experimental data and simulation data by the equation below. The result is also reported in the plots (Figure 2.8).

$$PCC = \frac{\sum_i (n_i^e - \overline{n^e}) * (n_i^s - \overline{n^s})}{\sqrt{\sum_i (n_i^e - \overline{n^e})^2 * \sum_i (n_i^s - \overline{n^s})^2}}), \tag{2.11}$$

where n_i^e is the experimentally measured number of the generated fluorescence photons (under concentration c_i), n_i^s is the corresponding simulated number of the generated fluorescence photons in the simulation, $\overline{n^e}$ is the mean of experimentally measured data under different iodine concentrations, and $\overline{n^s}$ is the mean of corresponding simulated data in the simulation.

2.4 Results

2.4.1 Excitation beam spectra

Figure 2.4 displays the excitation spectra from the three filter options. It shows both the experimentally measured spectra and the simulated spectra from SpekCalc [38]. All the spectra are normalized for better visual comparison. A good match between the simulations and measurements can be observed in the figure, which also validates the dose calculation method adopted in this study.

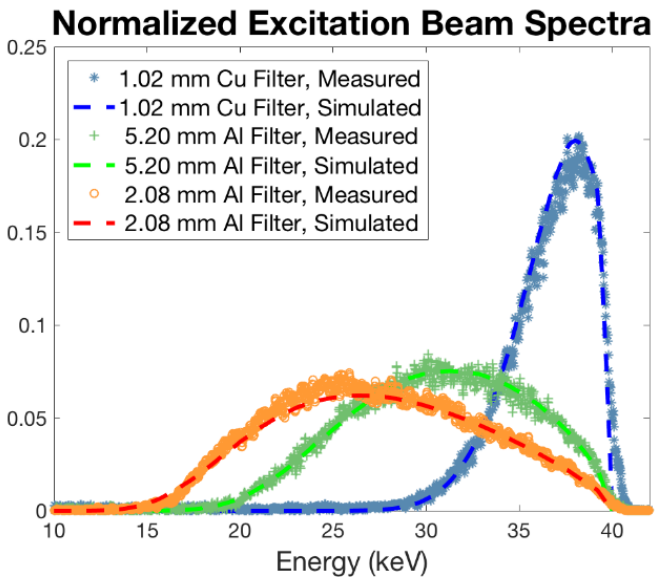

Figure 2.4: The normalized excitation spectra. The dots represent the experimentally measured data, and the dashed lines represent the simulated data from the SpekCalc.

2.4.2 Linearity between net fluorescence signals and iodine concentrations

The linearity between the net fluorescence signals and the corresponding iodine concentrations from the calibration phantom were investigated. Figure 2.5 shows the three linear least- squares-fitted curves for the fluorescence peak heights from the three filter options (1.02 mm Copper, 5.20 mm Aluminum, and 2.08 mm Aluminum). The linearity was characterized by the coefficients of determination (R^2), as displayed in the Figure 2.5. The coefficients of determination are all larger than 0.95 for the experiments with three excitation spectra. This good linearity indicates that the net fluorescence signals from our XFMI system can be used for quantifying the iodine concentrations with high confidence.

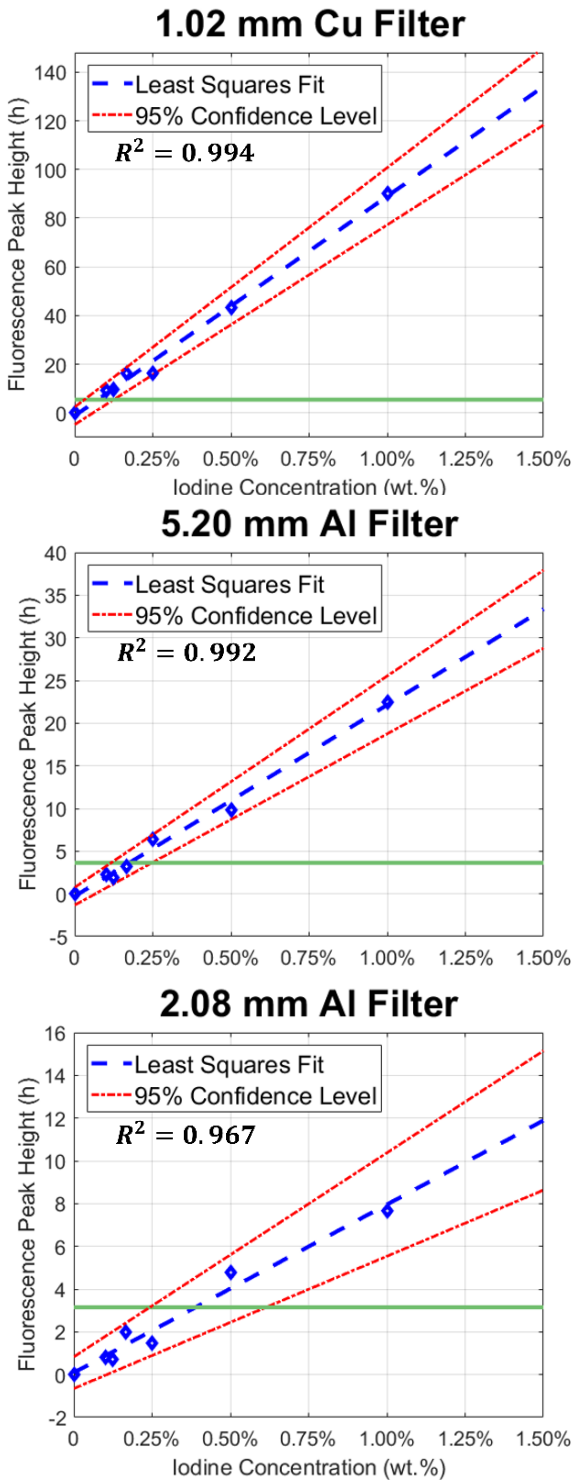

Figure 2.5: Linearity between the fluorescence peak heights and iodine concentrations under three excitation spectra. The blue dots are the experimentally obtained fluorescence peak heights at various concentrations, the dashed blue lines are the linear least squares fit to the fluorescence peak height data, the red dashed lines are the 95% confidence levels of the linear fits. The green solid lines are the $1.96\sigma_{bg}$ reference levels used to determine the MDCs.

2.4.3 Minimum detectable concentration

Using the data from the calibration phantom, the MDCs were obtained for the three filter options as shown in Fig. 5. The best sensitivity (i.e. MDC with the smallest value) came from the excitation spectrum by the 1.02 mm Cu filter, with the MDC as low as 0.074%, as listed in Table III. Compared to the MDC from the excitation spectrum by the 2.08 mm Al filter, the MDC from the excitation spectrum by the 5.20 mm Al filter was improved 2.22 times, and the MDC from the spectrum by the 1.02 mm Cu filer was improved 5.26 times. This demonstrates that the sensitivity of an XFMI system can be significantly increased by optimizing its excitation spectrum.

To find out the uncertainties of the MDCs, the 95% confidence levels of the linear fits to the fluorescence peak height data were plotted as the red dashed lines in Fig. 5. The intersection points of these 95% confidence level lines with the $1.96\sigma_{bg}$ reference line can be used to find out the uncertainties of the derived MDCs, which are shown in Table III.

Table 2.3: Minimum detectable concentrations at three excitation spectra.

Different Excitation Spectra Group:	MDC ($wt.$)
1.02mm Cu filter:	$0.074\%\ ^{-0.043\%}_{+0.051\%}$
5.20mm Al filter:	$0.175\%\ ^{-0.059\%}_{+0.072\%}$
2.08mm Al filter:	$0.389\%\ ^{-0.146\%}_{+0.225\%}$

2.4.4 XFMI image of contrast phantom

The XFMI image of the contrast phantom is shown in Figure 2.6. As can be seen from the figure, the positions of the three vials containing iodine solutions at three different concentrations are clearly visible, and the brightness of the three vials in the images correctly reflects the concentrations of the iodine solutions.

The XFMI signal at each vial location was plotted in Figure 2.7. For each excitation spectra, linear least squares fit was applied to the XFMI signals at the three vial locations. As shown in Figure 2.7, excellent linearity is observed ($R^2 > 0.97$ for both fits), which indicates the high confidence of our XFMI technique in accurately mapping out the different iodine concentrations in single XFMI experiment. Furthermore, our results show that the excellent

linearity ($R^2 > 0.97$) between the XFMI signals and the iodine concentrations can be achieved for iodine concentration from 0.2% to 1.0%.

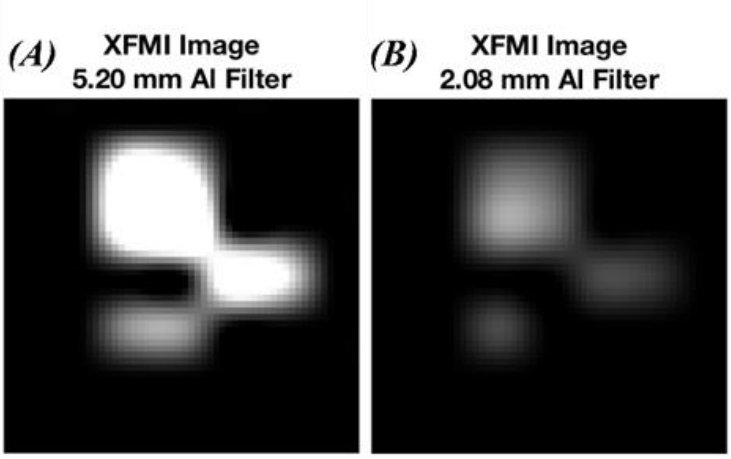

Figure 2.6: The XFMI images generated from the pixel-mapping method for the contrast phantom at two excitation spectra. The display window for the both images is [0, 40].

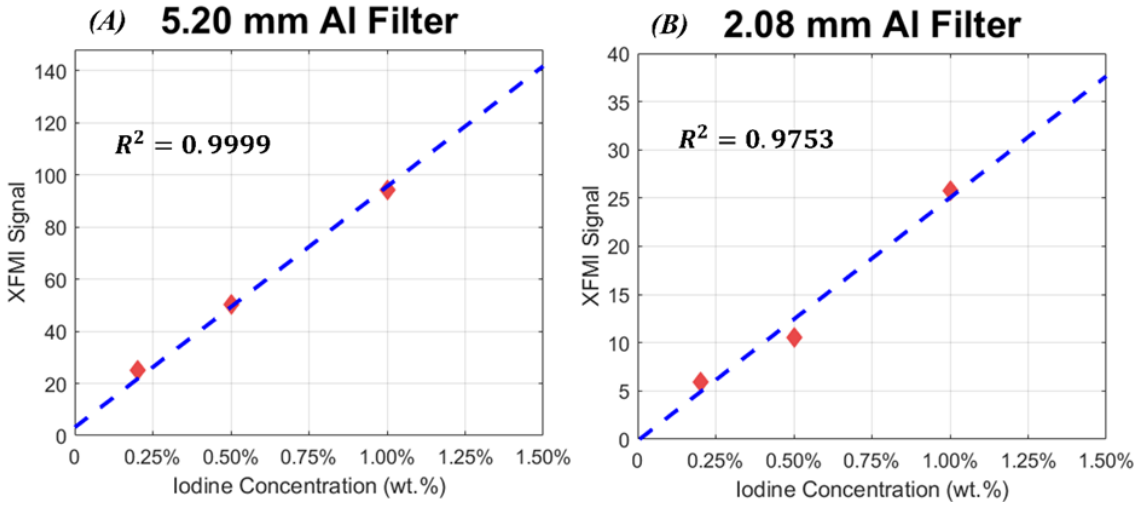

Figure 2.7: Linearity between the XFMI image signals and the iodine concentrations for the two XFMI experiments with (A) 5.20 mm Al filter, and (B) 2.08 mm Al filter.

2.4.5 Simulation vs. experiment

The comparison of simulation data with the experimental data is shown in Figure 2.8. A good match between the experimental data with the simulation model can be visually observed. To obtain the quantitative analysis of the deviation between the simulations and experiments, we report the PCC in plot. All the PCC values for all the three excitation

spectra are higher than 0.976. Henceforth, the simulation model is validated by the good agreement with the experimental data.

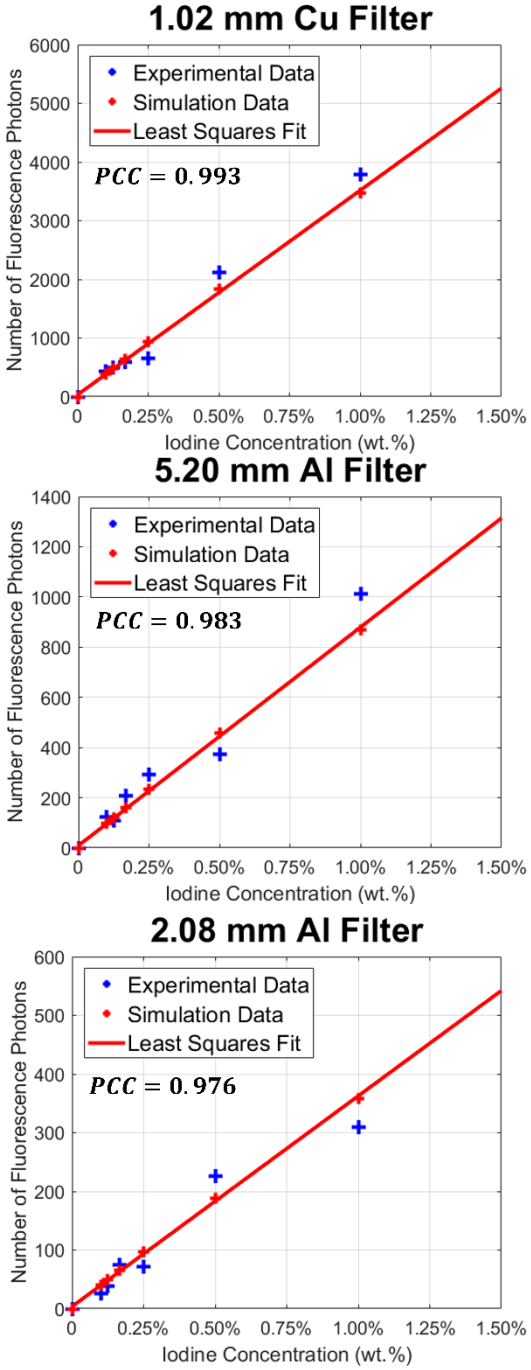

Figure 2.8: The comparison of experimental data with simulation data. The blue dots are the number of generated fluorescence photons (k_α peak) at various concentrations in the experimental data, the red dots are the number of generated fluorescence photons (k_α peak) at various concentrations in the simulation data, and the red lines are the linear least squares fits to the simulation data.

2.5 Discussion and conclusion

In this study, we experimentally investigated the impact of the excitation x-ray spectrum on the molecular sensitivity of XFMI in a pixel-mapping configuration. We investigated the effects of three distinctive excitation spectra, which were generated by changing the material and thickness of the x-ray source filter, on the XFMI imaging of a calibration phantom and a contrast phantom containing iodine solutions at low concentrations (≤ 1% wt.). We quantitatively determined the molecular sensitivity of the XFMI system using the minimum detectable concentration (MDC) of iodine. Our experimental results exhibit strong linearity between the fluorescence peak height and iodine concentration for the calibration phantom, as well as between the XFMI signal and iodine concentration for the contrast phantom. Furthermore, we developed an XFMI simulation model to simulate the XFMI system and validated the model with the experimental data. The good agreement ($\boldsymbol{PCC \geq 0.976}$) between the simulation and the experimental gives us high confidence in using the model to computationally search for an XFMI system that is optimized for a specific small-animal XFMI imaging task (spatial resolution, molecular sensitivity, radiation dose, spectrum optimization, source spectrum, detector configuration and geometry etc.) in future study.

We investigated the MDCs under different excitation spectra for a fixed surface entrance radiation dose level of 2 mGy. The result showed that increasing the thickness of the x-ray source filter (from 2.08 mm All to 5.20 mm Al) led to 2.22 times improvement in the molecular sensitivity, and when switching the filter to material with a higher atomic number (from 2.08 mm Al to 1.02 mm Cu), the molecular sensitivity was increased 5.26 times. The results are in line with what one would expect. It is well known that x-ray fluorescence of an element can only be generated by those excitation x-rays whose energies are higher than the K-edge of the element. For the three excitation spectra used in our study, as shown in the Figure 2.4, the spectrum generated by the 1.02 mm Cu filter contains the largest percentage of the effective x-rays that have the ability to generate x-ray fluorescence photons for iodine, and the spectrum generated by the 2.08 mm Al filter contains the smallest percentage of the effective x-rays. These results demonstrate the importance of

optimizing the excitation beam spectrum for improving the molecular sensitivity in Bremsstrahlung x-ray source based XFMI.

This effect of the excitation spectrum on molecular sensitivity of XFMI was further validated via the XFMI of a mouse-sized contrast phantom that contains various iodine concentrations. The generated XFMI images are shown in Figure 2.7. The XFMI image from the 5.20 mm Al filter clearly shows a better contrast between different iodine concentrations than the one from the 2.08 mm AL filter. Quantitatively, the contrast-to-noise ratio (CNR, defined as $CNR_{AB} = (Signal_A - Signal_B)/[(Noise_A + Noise_B)/2])$ between the 1% iodine solution and the 0.5% solution is 18.73 in the XFMI image from the 5.20 mm Al filter and 11.09 in the XFMI image from the 2.08 mm Al filter. Figure 2.7 shows the linearity between the XFMI image signals and the iodine concentrations. The slope of the linearly fitted line is referred as the sensitivity of XFMI system in some publications [12, 39]. Based on the slope, the molecular sensitivity in our XFMI system was improved by a factor of 3.61 from optimizing the excitation spectrum by changing the x-ray source filter from 2.08 mm Al to 5.20 mm Al. This result is consistent with the MDC finding using the calibration phantom.

The excitation spectrum can be further optimized to get even better sensitivity. There are at least two possible approaches. One is to increase the x-ray tube voltage to get more effective x-rays that are capable of generating fluorescence signals. However, the efficiency of exciting x-ray fluorescence from the target element by an excitation photon will decrease as the energy of the excitation photon increases, which will lead to lower dose efficiency (defined as sensitivity normalize by the radiation dose). Another is to further optimize the excitation spectrum by more filtering, for instance using a thicker copper filter to obtain a larger percentage of effective x-rays. For this approach, heavier filtration to the excitation beam can lead to higher sensitivity but it also comes with a cost of degraded contrasts in the image if using such filtration configuration for K-edge imaging and a cost of reduced excitation x-ray beam intensity, which will lead to longer exposure time to obtain the same amount of fluorescence signals. For example, as shown in Table 2.2 in this study, the required mAs for the Copper filter is 2479 times higher than the required mAs for the 2.08 mm Aluminum filter. To compensate for the long exposure time,

a higher x-ray source current can be adopted. For example, as shown in Table 2.2, we adopted different x-ray source currents for different excitation spectra. Therefore, for a given imaging task, a tradeoff between the excitation beam filtration, exposure time, and radiation dose has to be made. Furthermore, XFMI is inherently a molecular imaging modality. Similar to other existing molecular imaging modalities such as PET and SPECT, in the future XFMI can be combined with CT or MRI to receive both structure and physiological information.

XFMI of small animals, particularly mice and rats, will be valuable for many basic and preclinical studies. Improving the molecular sensitivity of XFMI system is the key to promote the application of XFMI technique. However, the molecular sensitivity of XFMI system is jointly affected by many factors, such as the detector configuration, the source configuration, the choice of contrast agent, and so on. For instance, different contrast agent (iodine, gold etc.) has different photoelectric absorption coefficient and fluorescence yield, which will lead to different fluorescence signal intensity. As a result, comprehensive investigations on how different configurations affect the molecular sensitivity are significant in optimizing the XFMI system design. In this study, we developed a simulation model to simulate an XFMI system and predict the generated x-ray photons based on the theoretical equations in Appendix. The simulation model was validated by the experimental data. This model can be used to predict the XFMI system sensitivity for different parameter choices (anode voltage, anode material, contrast agent, geometric configuration etc.). Using this model to investigate how to further optimize the XFMI system configuration to get higher molecular sensitivity will be our future research plan.

The achievable detected concentration for XFMI of the gold nanoparticle reported by Cheong et al. was 1.0% wt. at a dose of 2 Gy and a resolution of 0.1 mm [10]. After that, the extensive researches have been done to increase the sensitivity of XFMI techniques using laboratory x-ray sources. For example, Jones et al. reported the achievable gold nanoparticle concentration of 0.5% wt. at the dose of 204 mGy and a resolution of 3 mm in 2012 [13]; Ahmad et al. detected the concentration of 0.25% wt. at the dose of 14 mGy and a resolution of 6.4 mm in 2015 [17]; And Manohar et al. obtained the MDC as low as 0.24% wt. at the dose of 743 mGy and a resolution of 2.5 mm in 2016 [40]; Some relevant

works have shown that applying a sheet-beam configuration was helpful for sensitivity improvement [41, 42], and optimizing detector angular configuration was able to achieve one order of magnitude increase in sensitivity [43, 44]. Here we report the best sensitivity of 0.074% (wt.) for 2 mGy entrance dose at 3 mm spatial resolution for a laboratory x-ray source based XFMI system designed for small animal XFMI imaging. The improvement in sensitivity was achieved from excitation spectrum optimization via simple filtration.

In conclusion, a systematic investigation of the effect of the x-ray excitation spectrum on the molecular sensitivity of the XFMI system has been reported in this paper. We designed and generated three different excitation spectra by altering the x-ray filter material and thickness, and applied them to the XFMI imaging of two iodine-containing phantoms. The results show that under optimized excitation beam, the molecular sensitivity of the XFMI system was demonstrated to be much improved. Furthermore, based on the experimental investigation, an XFMI simulation model was built and validated, which will find use for further improving the molecular sensitivity and guiding the XFMI system design in the future.

References

[1] L. Ahlgren, K. Lidén, S. Mattsson, and S. Tejning, "X-ray fluorescence analysis of lead in human skeleton in vivo," *Scandinavian journal of work, environment & health*, pp. 82-86, 1976.

[2] R. Cesareo and S. Mascarenhas, "A new tomographic device based on the detection of fluorescent X-rays," *Nuclear Instruments and Methods in Physics Research Section A: Accelerators, Spectrometers, Detectors and Associated Equipment*, vol. 277, no. 2-3, pp. 669-672, 1989.

[3] J. P. Hogan, R. A. Gonsalves, and A. S. Krieger, "Fluorescent computer tomography: a model for correction of X-ray absorption," *IEEE Transactions on Nuclear Science*, vol. 38, no. 6, pp. 1721-1727, 1991.

[4] T. Yuasa *et al.*, "Reconstruction method for fluorescent X-ray computed tomography by least-squares method using singular value decomposition," *IEEE Transactions on Nuclear Science*, vol. 44, no. 1, pp. 54-62, 1997.

[5] P. J. La Rivière, "Approximate analytic reconstruction in x-ray fluorescence computed tomography," *Physics in medicine and biology*, vol. 49, no. 11, p. 2391, 2004.

[6] A. Simionovici *et al.*, "High-resolution x-ray fluorescence microtomography of homogeneous samples," *IEEE Transactions on Nuclear Science*, vol. 47, no. 6, pp. 2736-2740, 2000.

[7] J. F. Hainfeld, M. J. O'Connor, F. Dilmanian, D. N. Slatkin, D. J. Adams, and H. M. Smilowitz, "Micro-CT enables microlocalisation and quantification of Her2-targeted gold

nanoparticles within tumour regions," *The British journal of radiology,* vol. 84, no. 1002, pp. 526-533, 2011.
[8] N. Khlebtsov and L. Dykman, "Biodistribution and toxicity of engineered gold nanoparticles: a review of in vitro and in vivo studies," *Chemical Society Reviews,* vol. 40, no. 3, pp. 1647-1671, 2011.
[9] T. Takeda *et al.*, "X-ray fluorescent CT imaging of cerebral uptake of stable-iodine perfusion agent iodoamphetamine analog IMP in mice," *Journal of synchrotron radiation,* vol. 16, no. 1, pp. 57-62, 2009.
[10] S.-K. Cheong, B. L. Jones, A. K. Siddiqi, F. Liu, N. Manohar, and S. H. Cho, "X-ray fluorescence computed tomography (XFCT) imaging of gold nanoparticle-loaded objects using 110 kVp x-rays," *Physics in medicine and biology,* vol. 55, no. 3, p. 647, 2010.
[11] W. Cong, H. Shen, and G. Wang, "Spectrally resolving and scattering-compensated x-ray luminescence/fluorescence computed tomography," *Journal of biomedical optics,* vol. 16, no. 6, pp. 066014-066014-7, 2011.
[12] K. Ricketts *et al.*, "A quantitative x-ray detection system for gold nanoparticle tumour biomarkers," *Phys Med Biol,* vol. 57, no. 17, pp. 5543-55, Sep 07 2012.
[13] B. L. Jones, N. Manohar, F. Reynoso, A. Karellas, and S. H. Cho, "Experimental demonstration of benchtop x-ray fluorescence computed tomography (XFCT) of gold nanoparticle-loaded objects using lead- and tin-filtered polychromatic cone-beams," *Phys Med Biol,* vol. 57, no. 23, pp. N457-67, Dec 07 2012.
[14] Y. Kuang, G. Pratx, M. Bazalova, B. Meng, J. Qian, and L. Xing, "First demonstration of multiplexed x-ray fluorescence computed tomography (XFCT) imaging," *IEEE transactions on medical imaging,* vol. 32, no. 2, pp. 262-267, 2013.
[15] M. Ahmad, M. Bazalova, L. Xiang, and L. Xing, "Order of magnitude sensitivity increase in X-ray Fluorescence Computed Tomography (XFCT) imaging with an optimized spectro-spatial detector configuration: theory and simulation," *IEEE Trans Med Imaging,* vol. 33, no. 5, pp. 1119-28, May 2014.
[16] L. Ren, D. Wu, Y. Li, G. Wang, X. Wu, and H. Liu, "Three-dimensional x-ray fluorescence mapping of a gold nanoparticle-loaded phantom," *Med Phys,* vol. 41, no. 3, p. 031902, Mar 2014.
[17] M. Ahmad, M. Bazalova-Carter, R. Fahrig, and L. Xing, "Optimized Detector Angular Configuration Increases the Sensitivity of X-ray Fluorescence Computed Tomography (XFCT)," *IEEE Trans Med Imaging,* vol. 34, no. 5, pp. 1140-7, May 2015.
[18] C. Yoon, Y. Kim, and W. Lee, "3D Non-Destructive Fluorescent X-Ray Computed Tomography With a CdTe Array," *IEEE Transactions on Nuclear Science,* vol. 63, no. 3, pp. 1844-1853, 2016.
[19] D. Wu *et al.*, "Measurements of gold nanoparticle concentration with K-shell x-ray fluorescence spectrum," in *Proc. of SPIE Vol*, 2017, vol. 10065, pp. 100650M-1.
[20] S. Zhang, L. Li, and Z. Chen, "XFCT imaging system with pinhole collimation and attenuation correction," in *Nuclear Science Symposium, Medical Imaging Conference and Room-Temperature Semiconductor Detector Workshop (NSS/MIC/RTSD), 2016*, 2016, pp. 1-4: IEEE.
[21] T. Sasaya *et al.*, "Preliminary study on X-ray fluorescence computed tomography imaging of gold nanoparticles: Acceleration of data acquisition by multiple pinholes scheme," *Nuclear Instruments and Methods in Physics Research Section A: Accelerators, Spectrometers, Detectors and Associated Equipment,* 2017.
[22] L. Li, S. Zhang, R. Li, and Z. Chen, "Full-field fan-beam x-ray fluorescence computed tomography with a conventional x-ray tube and photon-counting detectors for fast nanoparticle bioimaging," *Optical Engineering,* vol. 56, no. 4, p. 043106, 2017.

[23] M. Bazalova, M. Ahmad, G. Pratx, and L. Xing, "L-shell x-ray fluorescence computed tomography (XFCT) imaging of Cisplatin," *Phys. Med. Biol,* vol. 59, no. 1, pp. 219-232, 2014.

[24] M. Bazalova-Carter, M. Ahmad, L. Xing, and R. Fahrig, "Experimental validation of L-shell x-ray fluorescence computed tomography imaging: phantom study," *Journal of Medical Imaging,* vol. 2, no. 4, pp. 043501-043501, 2015.

[25] N. Manohar, F. J. Reynoso, and S. H. Cho, "Experimental demonstration of direct L‐shell x‐ray fluorescence imaging of gold nanoparticles using a benchtop x‐ray source," *Medical physics,* vol. 40, no. 8, 2013.

[26] G. Cao, J. Lu, and O. Zhou, "X-ray fluorescence molecular imaging with high sensitivity: feasibility study in phantoms," in *SPIE Medical Imaging*, 2012, pp. 83130S-83130S-6: International Society for Optics and Photonics.

[27] T. Takeda *et al.*, "Iodine imaging in thyroid by fluorescent X-ray CT with 0.05 mm spatial resolution," *Nuclear Instruments and Methods in Physics Research Section A: Accelerators, Spectrometers, Detectors and Associated Equipment,* vol. 467, pp. 1318-1321, 2001.

[28] D. Wu, Y. Li, M. D. Wong, and H. Liu, "A method of measuring gold nanoparticle concentrations by x‐ray fluorescence for biomedical applications," *Medical physics,* vol. 40, no. 5, 2013.

[29] J. C. Larsson, W. Vågberg, C. Vogt, U. Lundström, D. H. Larsson, and H. M. Hertz, "High-spatial-resolution nanoparticle x-ray fluorescence tomography," in *Medical Imaging 2016: Physics of Medical Imaging*, 2016, vol. 9783, p. 97831V: International Society for Optics and Photonics.

[30] M. Shilo, T. Reuveni, M. Motiei, and R. Popovtzer, "Nanoparticles as computed tomography contrast agents: current status and future perspectives," *Nanomedicine,* vol. 7, no. 2, pp. 257-269, 2012.

[31] K. Ricketts, C. Guazzoni, A. Castoldi, and G. Royle, "A bench-top K X-ray fluorescence system for quantitative measurement of gold nanoparticles for biological sample diagnostics," *Nuclear Instruments and Methods in Physics Research Section A: Accelerators, Spectrometers, Detectors and Associated Equipment,* vol. 816, pp. 25-32, 2016.

[32] T. Takeda *et al.*, "Fluorescent x-ray computed tomography with synchrotron radiation using fan collimator," in *Proc. SPIE*, 1996, vol. 2708, pp. 685-695.

[33] W. Cong, H. Shen, G. Cao, H. Liu, and G. Wang, "X-ray fluorescence tomographic system design and image reconstruction," *Journal of X-ray science and technology,* vol. 21, no. 1, pp. 1-8, 2013.

[34] G. C. Kagadis, G. Loudos, K. Katsanos, S. G. Langer, and G. C. Nikiforidis, "In vivo small animal imaging: Current status and future prospects," *Medical Physics,* vol. 37, no. 12, pp. 6421-6442, 2010.

[35] C. T. Badea, M. Drangova, D. W. Holdsworth, and G. A. Johnson, "In vivo small-animal imaging using micro-CT and digital subtraction angiography," (in English), *Physics in Medicine and Biology,* Review vol. 53, no. 19, pp. R319-R350, Oct 2008.

[36] B. M. Tsui and D. L. Kraitchman, "Recent advances in small-animal cardiovascular imaging," (in eng), *J Nucl Med,* Research Support, N.I.H., Extramural Research Support, Non-U.S. Gov't Review vol. 50, no. 5, pp. 667-70, May 2009.

[37] R. Weissleder, "Scaling down imaging: molecular mapping of cancer in mice," (in eng), *Nat Rev Cancer,* Review vol. 2, no. 1, pp. 11-8, Jan 2002.

[38] G. Poludniowski, G. Landry, F. DeBlois, P. Evans, and F. Verhaegen, "SpekCalc: a program to calculate photon spectra from tungsten anode x-ray tubes," *Physics in medicine and biology,* vol. 54, no. 19, p. N433, 2009.

[39] R. Van Grieken and A. Markowicz, *Handbook of X-ray Spectrometry*. CRC Press, 2001.
[40] N. Manohar, F. J. Reynoso, P. Diagaradjane, S. Krishnan, and S. H. Cho, "Quantitative imaging of gold nanoparticle distribution in a tumor-bearing mouse using benchtop x-ray fluorescence computed tomography," *Scientific reports*, vol. 6, 2016.
[41] Q. Huo *et al.*, "Sheet-beam geometry for in vivo fluorescent x-ray computed tomography: proof-of-concept experiment in molecular imaging," *Optics letters*, vol. 33, no. 21, pp. 2494-2496, 2008.
[42] S. Jiang, P. He, L. Deng, M. Chen, and B. Wei, "Monte Carlo Simulation for Polychromatic X-Ray Fluorescence Computed Tomography with Sheet-Beam Geometry," *International Journal of Biomedical Imaging*, vol. 2017, 2017.
[43] H. Von Busch, G. Harding, G. Martens, J.-P. Schlomka, and B. Schweizer, "Investigation of externally activated x-ray fluorescence tomography for use in medical diagnostics," in *Medical Imaging 2005: Physics of Medical Imaging*, 2005, vol. 5745, pp. 90-102: International Society for Optics and Photonics.
[44] M. Sjölin and M. Danielsson, "Improved signal-to-noise ratio for non-perpendicular detection angles in x-ray fluorescence computed tomography (XFCT)," *Physics in medicine and biology*, vol. 59, no. 21, p. 6507, 2014.

Chapter 3 Material identification from photon counting CT

Xu Dong[1], Olga V. Pen[2], Zhicheng Zhang[3], and Guohua Cao[1]

[1]Department of Biomedical Engineering and Mechanics, Virginia Polytechnic Institute and State University, Blacksburg, VA 24061, USA.

[2]Department of Biomedical Engineering, Wake Forest University, Winston-Salem, NC, USA, 27109.

[3]Institute of Biomedical and Health Engineering, Shenzhen Institutes of Advanced Technology, Chinese Academy of Sciences, Shenzhen, Guangdong, China, 518055

Publication information – The major content of this chapter are the combination of one published paper (X. Dong, O. V. Pen, Z. Zhang, and G. Cao, "An improved physics model for multi-material identification in photon counting CT," in Medical Imaging 2019: Physics of Medical Imaging, 2019, vol. 10948, p. 109484O: International Society for Optics and Photonics. (DOI: 10.1117/12.2512525)) and one under-review manuscript (X. Dong, O. V. Pen, Z. Zhang, and G. Cao, "Improved material identification via accurate calculation of effective atomic number and electron density from photon counting CT images," Medical Physics, 2019).

3.1 Abstract

Purpose

Photon counting Computed Tomography (PCCT) has been considered as a revolutionary technique in recent years. Different from conventional CT, one PCCT scan can generate multiple CT image datasets corresponding to the multiple pre-set energy bins. Therefore,

the richness of the image information from PCCT opens the possibility of achieving the material identification capability for CT. In this work, we present a model to calculate effective atomic number (Z_{eff}) and effective electron density ($\rho_{e_{eff}}$) and further combine the model with PCCT image data to achieve material identification for PCCT.

Methods

An equation to model the x-ray interaction with single element material was developed by Hawkes and Jackson based on x-ray interaction physics. We adapted the equation to extend its usage for all the materials (single elements, compounds, and mixtures). Furthermore, we developed a model to calculate Z_{eff} and $\rho_{e_{eff}}$ of any material from the x-ray energy (E) and corresponding linear attenuation coefficient (μ). The performance of our model was validated on a broad range of materials under various energy circumstances. The relative standard deviation of calculated Z_{eff} and $\rho_{e_{eff}}$ was used to evaluate the accuracy of the model.

To study the feasibility of applying the model with PCCT image data for material identification purpose, we conducted both PCCT system numerical simulation and physical experiment. In the simulation, an ideal detector model and a realistic detector model were utilized separately. A $Z_{eff} - \rho_{e_{eff}}$ map was generated to display the calculated Z_{eff} and $\rho_{e_{eff}}$ of different materials. Besides, the relative errors were computed by comparing the Z_{eff} and $\rho_{e_{eff}}$ calculated from PCCT data with those calculated from NIST database.

Results

In the model validation, the relative standard deviations are mostly less than 1% (161 out of 168) shows that our developed model obtains good accuracy and robustness to energy conditions. When incorporating the model with PCCT image data, different materials (acetone, water, silicon dioxide, sodium chloride, and calcium chloride) can be clearly identified in the $Z_{eff} - \rho_{e_{eff}}$ map. Compared to the ground truth, the averaged absolute relative errors of calculated Z_{eff} across all the five materials are 2.1% for the simulated ideal detector model, 6.3% for the simulated realistic detector model, and 6.6% for the physical experiment. And the averaged absolute relative errors of calculated $\rho_{e_{eff}}$ across

all the five materials are 1.8% for the simulated ideal detector model, 5.1% for the simulated realistic detector model, and 5.6% for the physical experiment. The relatively small errors confirm the potential that we can use the model with PCCT data to achieve material identification purpose.

Conclusions

In this study, a model was developed to calculate effective atomic number and effective electron density from PCCT data. The feasibility of incorporating the model with PCCT data was verified and material identification was achieved in the $Z_{eff} - \rho_{e_{eff}}$ map. Our model can serve as a material identification scheme for PCCT system in the future.

Keywords: Photon counting CT, material identification, effective atomic number, x-ray interaction physics.

3.2 Introduction

Conventional x-ray Computed Tomography (CT) has several limitations such as low contrast for soft tissues and lack of material-specific capability and therefore can hardly be used for material identification. Recently, those limitations have reportedly been alleviated by an emerging technique - photon counting Computed Tomography (PCCT) [1-3]. The PCCT employs energy-resolving, photon counting x-ray detector to distinguish the energies of the detected photon, and sort the measured photons into several preset energy bins. The number of preset energy bins is usually more than two [3], which leads to multiple sinogram datasets from a single CT scan. After tomographic image reconstruction, PCCT can generate multiple CT image datasets from one scan with each CT image set corresponding to one energy bin.

The richness of the image information from PCCT opens the possibility of achieving the material identification capability for CT. Previously, several methods have been proposed to identify or separate materials based on PCCT data. Butzer *et. al.* used principal component analysis method to extract the difference between materials [4]; Wang et al. proposed an angular separation method in the attenuation map to separate the materials [5];

Moreover, the traditional material decomposition method has been widely adapted by many researches [6-10]. Another method to achieve material identification is to calculate effective atomic number and electron density for the imaged materials [11, 12]. Because effective atomic number and electron density are the intrinsic properties of materials, characterizing a material by its effective atomic number and electron density is more intuitive. The goal of this study is to develop a method to calculate the two parameters (effective atomic number and effective electron density) from PCCT data to achieve multiple material identification from one PCCT scan.

Calculating effective atomic number for compounds and mixtures from CT image data has been a classical problem in the CT field [13-20]. Interestingly, several different definitions for effective atomic number have been proposed. For example, effective atomic number was typically calculated with atomic percentage weighting from the formula for a heterogeneous material [13, 21]. Others proposed to use the power law to approximate effective atomic number [15, 17], or calculated effective atomic number based on interpolation [18]. More comprehensive reviews about different effective atomic number definitions can be found in [19, 22].

Despite those prior works, one of the major problems for applying those definitions into real-world applications is that they are based on rather simple approximations. Those simple approximations may be true for some materials but could lead to high error for other materials, which raises concern for applying those methods to more general applications over the complex materials encountered in biomedical applications. Besides, using those methods to calculate effective atomic number can even lead to inconsistent results for the same material. Some methods led to energy-independent effective atomic numbers [18, 21], while other methods led to energy-dependent effective atomic numbers. Similar problem exists for the calculation of effective electron density [21]. Our aim in this work is to address such inconsistency in the calculated effective atomic numbers from PCCT data and come up with a general framework for material identification through effective atomic number and effective electron density.

Hawkes and Jackson parametrized the x-ray attenuation coefficients based on the x-ray matter interaction physics, and derived exact formulas for effective atomic number and

effective electron density for heterogenous materials in 1980s [23, 24]. Because their model started from the basic physics ab initio, their formulas for effective atomic number and effective electron density can hold true for a broad range of scenarios. However, their formulas are very complicated and hard to compute, especially for compounds and mixtures. The details of Hawkes and Jackson's model will be explained more as follows.

In this study, our objective is to build a model to calculate effective atomic number and effective electron density so that we can calculate them from PCCT data for material identification in biomedical applications. To achieve this purpose, a balance between the physical accuracy of the model and the numerical computability of the model was made. In essence, in this work we developed a model based on the x-ray matter interaction physics [23] [24] so that the model can have high accuracy, and also made simplifications to make the model feasible for extracting effective atomic number and effective electron density for different materials based on PCCT image data.

The paper is organized as follows. After the introduction, in section II we explained our model for calculating effective atomic number and effective electron density, and validated the accuracy of the model over some materials. We then carried out PCCT physical experiment and PCCT numerical simulation, and use the data from simulations and experiments to demonstrate the usability of the model. The results are shown in section III, and the discussions and conclusions are in section IV.

3.3 Methods

3.3.1 The derivation of the model

As we all know, linear attenuation coefficient (μ) of a material is determined by the photon energy (E) and the intrinsic properties of the material. For single elements, the intrinsic properties can be summarized as the atomic number (Z) and the electron density (ρ_e). According to the Hawkes and Jackson [23, 24], the linear attenuation coefficient (μ) of single elements can be parameterized by the following equation:

$$\mu(E, Z, \rho_e) = f(E, Z, \rho_e) = \rho_e(Z^4 F(E, Z) + G(E, Z)) \tag{3.1}$$

where $Z^4 F(E, Z)$ corresponds to the photoelectric cross-section, and $G(E, Z)$ corresponds to the scattering cross-section term. The detailed derivation of the equations $F(E, Z)$ and $G(E, Z)$ can be found in Hawkes and Jackson's papers [23, 24]. We also summarized the derivation in Appendix in this paper.

Compounds and mixtures are composited by a bunch of single elements with different atomic numbers (Z_i) and electron densities (ρ_{e_i}). For a compound or mixture composed of n different elements, Hawkes and Jackson provides a detailed parameterization of μ [24]. The equation can be summarized as:

$$\mu = g(E, Z_1, Z_2, \dots, Z_n, \rho_{e_1}, \rho_{e_2}, \dots, \rho_{e_n}) \tag{3.2}$$

This formula is based on the elemental composition of a specific material, which has $2n + 1$ parameters, and n is varying since different material have different number of elemental compositions. Henceforth, the variety of the parameters makes the formula too complicated to be utilized with PCCT data.

To obtain the numerical computability of the model, we generally hope to use two parameters to characterize the compounds and mixtures as we use atomic number (Z) and electron density (ρ_e) to characterize single elements. Since single elements can be considered as a special case of compounds and mixtures with only one elemental composition, we can expect the parameterization of μ for single elements sharing a lot of similarity with the parameterization of μ for compounds and mixtures. Inspired by the equation (3.1) as the parameterization of μ for single elements, we define two corresponding parameters for compounds and mixtures: the effective atomic number (Z_{eff}) and the effective electron density ($\rho_{e_{eff}}$)1, and we assume the linear attenuation coefficient (μ) for compounds and mixtures can be parameterized in a similar way as for single elements:

$$\mu\left(E, Z_{eff}, \rho_{e_{eff}}\right) = f\left(E, Z_{eff}, \rho_{e_{eff}}\right) = \rho_{e_{eff}}(Z_{eff}^4 F\left(E, Z_{eff}\right) + G\left(E, Z_{eff}\right)) \quad (3.3)$$

Both Z_{eff} and $\rho_{e_{eff}}$ should be the material's intrinsic properties and invariant to photon energy, as a result, they are functions of the atomic numbers (Z_i) and the electron densities (ρ_{e_i}) of the material's elemental compositions:

$$Z_{eff} = h_1\left(Z_1, \dots, Z_n, \rho_{e_1}, \dots, \rho_{e_n}\right) \quad (3.4)$$

$$\rho_{e_{eff}} = h_2\left(Z_1, \dots, Z_n, \rho_{e_1}, \dots, \rho_{e_n}\right) \quad (3.5)$$

The validity of equation (3.3) can be proven by linking it to equation (3.2) and solving the functions h_1 and h_2 from the following set of differential equations:

[1] We use the name of effective electron density here instead of electron density, because this value of the effective electron density is calculated from equation (3.3). It may or may not be exactly the real electron density of the material itself. The purpose of defining such parameter is to use it to characterize materials, which could or could not be the real electron density for the material. We are using the terminology of effective electron density here in order to avoid the potential conflict with the concept of real electron density of a material.

$$\begin{cases} \frac{\partial g}{\partial Z_1} = \frac{\partial f}{\partial Z_{eff}} * \frac{\partial h_1}{\partial Z_1} + \frac{\partial f}{\partial \rho_{e_{eff}}} * \frac{\partial h_2}{\partial Z_1} \\ \frac{\partial g}{\partial Z_2} = \frac{\partial f}{\partial Z_{eff}} * \frac{\partial h_1}{\partial Z_2} + \frac{\partial f}{\partial \rho_{e_{eff}}} * \frac{\partial h_2}{\partial Z_2} \\ \vdots \\ \frac{\partial g}{\partial Z_n} = \frac{\partial f}{\partial Z_{eff}} * \frac{\partial h_1}{\partial Z_n} + \frac{\partial f}{\partial \rho_{e_{eff}}} * \frac{\partial h_2}{\partial Z_n} \\ \frac{\partial g}{\partial \rho_{e_1}} = \frac{\partial f}{\partial Z_{eff}} * \frac{\partial h_1}{\partial \rho_{e_1}} + \frac{\partial f}{\partial \rho_{e_{eff}}} * \frac{\partial h_2}{\partial \rho_{e_1}} \\ \frac{\partial g}{\partial \rho_{e_2}} = \frac{\partial f}{\partial Z_{eff}} * \frac{\partial h_1}{\partial \rho_{e_2}} + \frac{\partial f}{\partial \rho_{e_{eff}}} * \frac{\partial h_2}{\partial \rho_{e_2}} \\ \vdots \\ \frac{\partial g}{\partial \rho_{e_n}} = \frac{\partial f}{\partial Z_{eff}} * \frac{\partial h_1}{\partial \rho_{e_n}} + \frac{\partial f}{\partial \rho_{e_{eff}}} * \frac{\partial h_2}{\partial \rho_{e_n}} \end{cases} \quad (3.6)$$

With this definition for effective atomic number and effective electron density, equation (3.3) can be applicable to any material, be it single element, compound, or mixture. Z_{eff} and $\rho_{e_{eff}}$ can be iteratively computed from several measurements of E and μ according to equation (3.3). The iterative algorithm we chose in the study was Levenberg–Marquardt algorithm. Therefore, using the definition of effective atomic number and effective electron density from equation (3.3) and the Levenberg–Marquardt algorithm, one can calculate the energy-invariant Z_{eff} and $\rho_{e_{eff}}$ from several groups of (E, μ) measurements.

As discussed above, the validity of the model can be proven if the set of differential equations (6) is solvable. But considering the complexity of solving the differential equations, instead of calculating the analytical solutions of h_1 and h_2, we will validate the model in a more feasible way by manually testing the accuracy of the calculated Z_{eff} and $\rho_{e_{eff}}$ under various x-ray energy conditions for a broad range of materials.

3.3.2 The validation of the model

As the validation of the model, we manually tested the accuracy of the calculated Z_{eff} and $\rho_{e_{eff}}$ under various x-ray energy conditions for a broad range of materials. The materials contain single elements (carbon, sodium, aluminum, and calcium), compounds (acetone,

water, silicon dioxide, sodium chloride, and calcium peroxide), and mixtures (70% ethanol solution, saline, and 10% sodium chloride solution).

For each material, we randomly chose photon energy (E) in the range from 30 keV to 120 keV and obtained the corresponding linear attenuation coefficient (μ) from NIST database [25]. Then we repeated the calculation 10,000 times with different randomly chosen photon energies to test the robustness of the model. Besides, since Z_{eff} and $\rho_{e_{eff}}$ are iteratively calculated, the number of groups of (E, μ) combination as the input of the model is flexible, which can be any number more than one. Therefore, we tested using two groups, three groups, four groups, five groups, six groups, seven groups, and eight groups of (E, μ) combination as the input of the model to validate its accuracy over different numbers of groups of (E, μ) combination.

In summary, for each material, under each certain number of groups of (E, μ) combination, we calculated Z_{eff} and $\rho_{e_{eff}}$ 10,000 times with randomly chosen photon energy. We calculated the mean value and the standard deviation of the Z_{eff} and $\rho_{e_{eff}}$ over 10,000-time calculations. Then the relative standard deviation ($\frac{mean}{standard\ deviation}$) was used to measure the accuracy of the model. The results are reported in Table 3.3.

3.3.3 The physical experiment of PCCT

A phan beam photon counting CT system was built in a laboratory benchtop platform. A picture of the PCCT setup is shown in Figure 3.1 and the illustration is shown in Figure 3.2. It mainly consisted of a laboratory x-ray source and an aluminum beam filter, a scatter collimator, a mouse sized phantom, and a photon counting detector with collimator. The PCCT systematic parameters and the scan protocols are listed in Table 3.1.

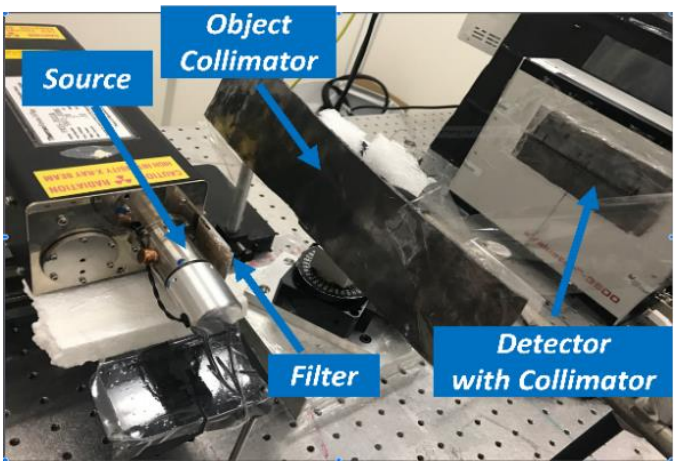

Figure 3.1: The picture of experimental setup.

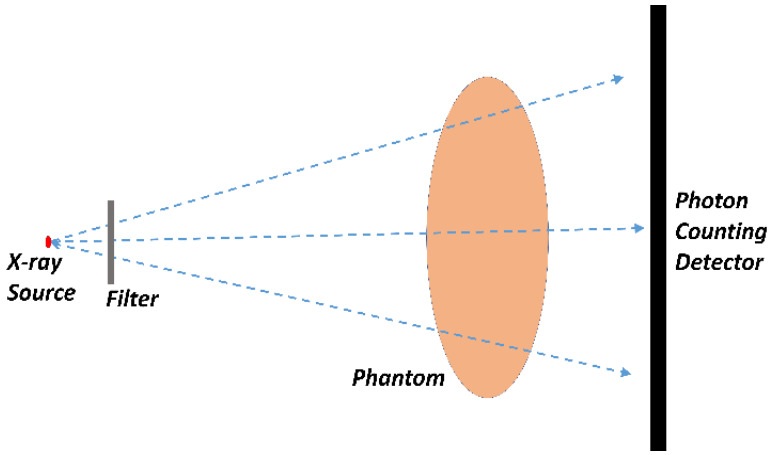

Figure 3.2: Schematics of the simulated PCCT system.

Table 3.1: Parameters of the PCCT system.

Source voltage	70 kV
Filter	2.10 mm Aluminum
Source to isocenter distance	147 mm
Source to detector distance	515 mm
Detector pixel size	0.5 mm
Detector resolution	256 pixels
Data acquisition	1 projection per degree 360 projections in total

3.3.3A X-ray source and filter

A commercially available x-ray source (Thermo Kevex x-ray) with tungsten anode was operated at 70 kV. The x-ray source current was set to be 0.05 mA. The small current was

used to control the x-ray flux and prevent the pulse pileup effect in photon counting detector. A 2.10 mm aluminum filter was placed at the x-ray source exit window to shape the x-ray spectrum.

3.3.3B Image phantom

One water phantom and one contrast phantom were built for the study. Both phantoms were made by polymethyl methacrylate (PMMA) container with the diameter of 25.45 mm. For the water phantom, the container was simply filled by only water (H2O). For the contrast phantom, other than filling water as background, we also inserted four vials with the diameter of 6.36 mm into the container. The vials were filled by acetone (C3H6O), silicon dioxide (SiO2), sodium chloride (NaCl), and calcium chloride (CaCl2), respectively. The picture of the phantoms is shown in Figure 3.3 and the schematic illustration of the phantoms is shown in Figure 3.4.

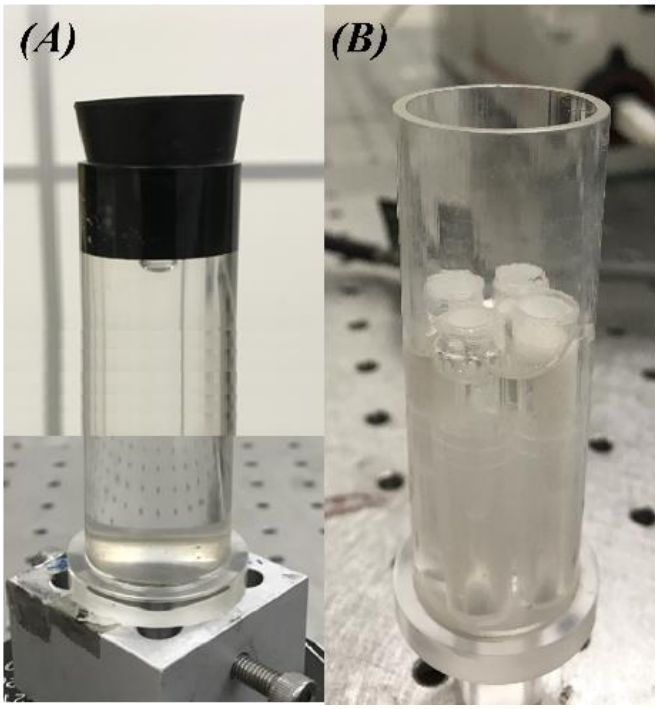

Figure 3.3: The picture of water phantom and contrast phantom used in the experiment.

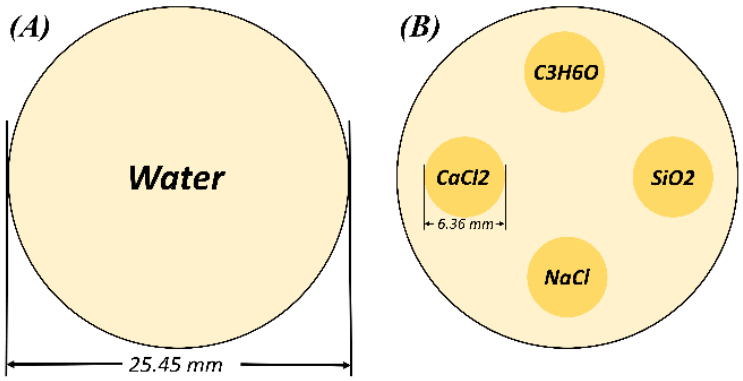

Figure 3.4: Schematics of the phantoms used in the simulation.

3.3.3C Photon counting detector

X-rays were detected by a commercially available photon counting detector (eV-3500, eV products). The detector has 256 pixels and all of them are lined up in a single row. Therefore, the resolution of the detector is 1 × 256 with each detector pixel size to be 2 mm × 0.5 mm, where the pixel size along the row is 0.5 mm. The sensor of the detector is made of CdZnTe and the application specific integrated circuit (ASIC) was connected behind the sensor. After x-ray signal being detected by the sensor and processed by ASIC, it is then analyzed by the connected computer.

The detector can support to collect photon counts simultaneously in as many as four energy bins. In our experiment, the four energy bins were preset from 30 keV to 70 keV with a fixed energy bin width of 10 keV, which is listed in Table 3.2.

3.3.3D Collimation

Since the x-ray beam from the x-ray source is in cone beam shape, scatters can be generated in every part of the phantom that is exposed to x-rays, and the generated scatter photons stand a good chance to be detected by the detector if without any collimation. In the study, we want to construct a phan-beam photon counting CT, therefore we need to prevent the scatter generated outside of the phan beam plane (off-plane scatter) from contaminating the detected signal. To eliminate the scatter contamination, we placed an object collimator and a detector collimator in front of the phantom and in front of the detector respectively (as shown in Figure 3.1). Both collimators are made of lead sheet with the thickness of 5 mm, and they both have a 3-mm-width slot at the center to let x-rays pass through. In such

a way, only signal in the plane formed by the slots can be collected. Therefore, most of the off-plane scatter were blocked and the phan beam PCCT system was constructed.

3.3.4 The numerical simulation of PCCT

Numerical simulation of the phan-beam PCCT system was also conducted with the same geometrical setup and scanning protocol as in the physical experiment. The simulated system is illustrated in Figure 3.2 and the scanning protocol is also listed in Table 3.1. Like in the physical experiment, one water phantom and one contrast phantom were used in the simulation as illustrated in Figure 3.4.

The workflow of the simulation is mainly consisted of three parts. First, the excitation beam was generated by SpekCalc program [26] with the operation voltage as 70keV and 2.10 mm as the filter. Then the line-based Siddon's algorithm[27] was used to calculate the attenuation of each ray and to forward project x-ray photons. After the photons reach the detector, all the incident photons will go through the photon counting detector model. In reality, a real photon counting detector has many detector degradation effects.[28] To model the complexity of a real detector, we adapted the photon counting detector model developed by Taguchi *et al.*[29] to simulate the realistic detector response, including photon noise and detector noise, charge sharing, K-escape x-ray, etc. Meanwhile, for the purpose of comparison, an ideal detector model was used in the simulation, which simply assumes the x-ray spectrum outputted by the detector is perfectly the same as the spectrum hitting onto the detector surface without any distortion in the detector response.

3.3.5 Data processing

In both simulation and experiment, four energy bins were pre-set from 30 keV to 70 keV with a fixed energy bin width of 10 keV, as listed in Table 3.2. Therefore, four reconstructed images were generated in one scan, with each image corresponding to one energy bin. We first calculated the effective energy (E_{eff}) for each energy bin defined as the average of the x-ray photon energies weighted by the x-ray photon intensities:

$$E_{eff} = \frac{\sum_{E_{low}}^{E_{high}} E_i * I_i}{\sum_{E_{low}}^{E_{high}} I_i} \tag{3.7}$$

where E_{low} and E_{high} are the boundaries of the energy bin, E_i in the energy of each x-ray photon in the energy bin, and I_i is the intensity of the x-ray photon with the energy of E_i. By equation (3.7), we can use E_{eff} to represent the overall energy of interacting x-ray photons in each energy bin.

After obtaining E_{eff} for every energy bin, the linear attenuation coefficients (μ) corresponding to the energy bin can be obtained from the pixel values in the CT image. To eliminate the interference of the image noise, we calculated the averaged linear attenuation coefficient (μ) for each material by averaging the image pixel values in the Region of Interest (ROI) illustrated in Figure 3.5. As a result, a combination of the interacting x-ray photon energy (E) and the linear attenuation coefficient (μ) can be obtained for each material at each energy bin. Four combinations of (E, μ) can be obtained from the PCCT image data sets with four energy bins. The accuracy of the linear attenuation coefficient (μ) from the simulated realistic detector model, the simulated ideal detector model, and the physical experiment were calculated by comparing them with the linear attenuation coefficients (μ) from NIST database [25]. The relative errors are listed in Table 3.4.

Then we fed the four (E, μ) combinations into the model to calculate Z_{eff} and $\rho_{e_{eff}}$. To compare the accuracy, the Z_{eff} and $\rho_{e_{eff}}$ were calculated from PCCT data by the simulated realistic detector model, PCCT data by the simulated ideal detector model, PCCT data by the physical experiment, as well as the linear attenuation coefficient values taken from the NIST database [25]. The calculated Z_{eff} and $\rho_{e_{eff}}$ from NIST database data were treated as the ground truth for comparison. A $Z_{eff} - \rho_{e_{eff}}$ plot was generated to display the result as shown in Figure 3.6. We also computed the relative errors of calculated Z_{eff} and $\rho_{e_{eff}}$ from PCCT data when compared with the ground truth, as reported in Table 3.5.

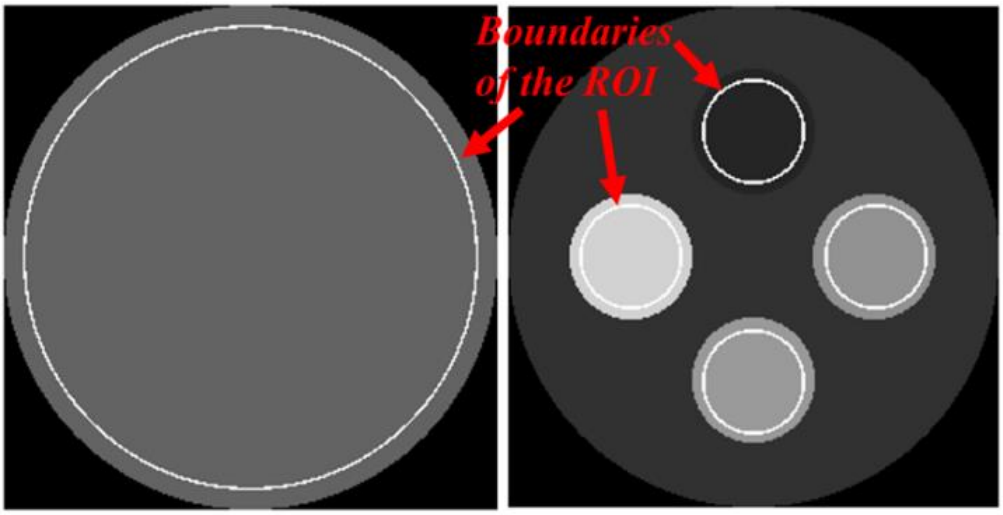

Figure 3.5: The illustration of the ROIs in the reconstructed images to calculate the averaged linear attenuation coefficients (μ). The left image is one reconstructed image of the water phantom; the right image is one reconstructed image of the contrast phantom.

Table 3.2: The setup of the energy bins.

Energy Bin	Energy Range	Corresponding Effective Energy
Bin 1:	30 – 40 keV	35.08 keV
Bin 2:	40 – 50 keV	44.79 keV
Bin 3:	50 – 60 keV	54.55 keV
Bin 4:	60 – 70 keV	63.40 keV

3.4 Results

3.4.1 The validation of the model

The relative standard deviations of the computed Z_{eff} and $\rho_{e_{eff}}$ are reported in Table 3.3. The result shows that the relative standard deviations for all the materials are mostly less than 1% (161 out of 168). The small standard deviations indicate that the Z_{eff} and $\rho_{e_{eff}}$ calculated from the model are not dependent on the input energies. Furthermore, as the number of (E, μ) combinations increases, the relative standard deviation becomes smaller. This trend is valid for all the studied materials, which implies that the model has higher accuracy with more energy bins as inputs. For instance, when using eight (E, μ)

combinations as the input, the relative standard deviations for all the studied materials are less than 0.38%.

3.4.2 The accuracy of linear attenuation coefficients in PCCT image

The averaged μ in ROIs of the PCCT image data were compared with the μ obtained from the NIST database. As shown in Table 3.4, we can see both the simulated realistic detector model and the physical detector used in experiments will induce linear attenuation coefficient value error to some certain extent in the reconstructed images. The error comes from the spectral distortion in the detector response due to the intrinsic degradation factors in the photon counting detector [29]. As reported in Table 3.4, the averaged absolute relative errors across all the five materials and all the energy bins are 1.26% for the simulated ideal PCT model, 5.52% for the simulated realistic detector model, and 7.94% for the physical experiment.

3.4.3 Calculation of Z_{eff} and $\rho_{e_{eff}}$ from PCCT data

As shown in Figure 3.6, we can see all the five materials can be clearly separated in the $Z_{eff} - \rho_{e_{eff}}$ map, and the calculated Z_{eff} and $\rho_{e_{eff}}$ from the PCCT data (both simulation data and experimental data) are well correlated with the calculated Z_{eff} and $\rho_{e_{eff}}$ from the NIST data (ground truth). We can clearly separate and identify each material in the $Z_{eff} - \rho_{e_{eff}}$ map by comparing the calculated Z_{eff} and $\rho_{e_{eff}}$.

We also computed the relative errors of the calculated Z_{eff} and $\rho_{e_{eff}}$ from PCCT data by comparing them with Z_{eff} and $\rho_{e_{eff}}$ calculated from NIST data. As listed in Table 3.5, the averaged absolute relative errors of calculated Z_{eff} across all the five materials are 2.1% for the simulated ideal detector model, 6.3% for the simulated realistic detector model, and 6.6% for the physical experiment. And the averaged absolute relative errors of calculated $\rho_{e_{eff}}$ across all the five materials are 1.8% for the simulated ideal detector model, 5.1% for the simulated realistic detector model, and 5.6% for the physical experiment. The relatively small errors also confirm the potential that we can incorporate the model with PCCT data to achieve material identification purpose.

Table 3.3: The relative standard deviations of the calculated effective atomic numbers ($\boldsymbol{Z_{eff}}$) and effective electron densities ($\boldsymbol{\rho_{eff}}$) under different numbers of groups of (μ, E) combination as the input of the model over 10,000-time calculations.

Number of Groups of (μ, E) combination	**Carbon (C)**		**Sodium (Na)**		**Aluminum (Al)**		**Calcium (Ca)**	
	Relative Standard Deviation of $\boldsymbol{Z_{eff}}$	Relative Standard Deviation of $\boldsymbol{\rho_{eff}}$	Relative Standard Deviation of $\boldsymbol{Z_{eff}}$	Relative Standard Deviation of $\boldsymbol{\rho_{eff}}$	Relative Standard Deviation of $\boldsymbol{Z_{eff}}$	Relative Standard Deviation of $\boldsymbol{\rho_{eff}}$	Relative Standard Deviation of $\boldsymbol{Z_{eff}}$	Relative Standard Deviation of $\boldsymbol{\rho_{eff}}$
2	5.45%	0.22%	0.63%	0.19%	5.45%	0.22%	0.37%	0.18%
3	0.84%	0.05%	0.15%	0.05%	0.84%	0.05%	0.09%	0.05%
4	0.43%	0.03%	0.07%	0.03%	0.43%	0.03%	0.05%	0.03%
5	0.27%	0.02%	0.05%	0.02%	0.27%	0.02%	0.03%	0.02%
6	0.20%	0.02%	0.04%	0.02%	0.20%	0.02%	0.02%	0.02%
7	0.16%	0.02%	0.03%	0.02%	0.16%	0.02%	0.02%	0.02%
8	0.14%	0.01%	0.03%	0.02%	0.14%	0.01%	0.02%	0.02%
Number of Groups of (μ, E) combination	**Acetone (C3H6O)**		**Water (H2O)**		**Silicon Dioxide (SiO2)**		**Sodium Chloride (NaCl)**	
	Relative Standard Deviation of $\boldsymbol{Z_{eff}}$	Relative Standard Deviation of $\boldsymbol{\rho_{eff}}$	Relative Standard Deviation of $\boldsymbol{Z_{eff}}$	Relative Standard Deviation of $\boldsymbol{\rho_{eff}}$	Relative Standard Deviation of $\boldsymbol{Z_{eff}}$	Relative Standard Deviation of $\boldsymbol{\rho_{eff}}$	Relative Standard Deviation of $\boldsymbol{Z_{eff}}$	Relative Standard Deviation of $\boldsymbol{\rho_{eff}}$
2	0.16%	1.45%	0.63%	0.19%	0.48%	0.20%	0.28%	0.23%
3	0.09%	0.75%	0.15%	0.05%	0.13%	0.05%	0.09%	0.09%
4	0.07%	0.54%	0.07%	0.03%	0.07%	0.04%	0.06%	0.07%
5	0.06%	0.44%	0.05%	0.02%	0.05%	0.03%	0.05%	0.06%
6	0.05%	0.36%	0.04%	0.02%	0.04%	0.02%	0.04%	0.05%
7	0.04%	0.31%	0.03%	0.02%	0.03%	0.02%	0.04%	0.04%
8	0.04%	0.27%	0.03%	0.02%	0.03%	0.02%	0.03%	0.04%
Number of Groups of (μ, E) combination	**Calcium Chloride (CaCl2)**		**70% Ethanol**		**0.9% NaCl**		**10% NaCl**	
	Relative Standard Deviation of $\boldsymbol{Z_{eff}}$	Relative Standard Deviation of $\boldsymbol{\rho_{eff}}$	Relative Standard Deviation of $\boldsymbol{Z_{eff}}$	Relative Standard Deviation of $\boldsymbol{\rho_{eff}}$	Relative Standard Deviation of $\boldsymbol{Z_{eff}}$	Relative Standard Deviation of $\boldsymbol{\rho_{eff}}$	Relative Standard Deviation of $\boldsymbol{Z_{eff}}$	Relative Standard Deviation of $\boldsymbol{\rho_{eff}}$
2	0.29%	0.39%	7.48%	0.99%	2.19%	0.20%	0.96%	0.19%
3	0.17%	0.23%	3.73%	0.54%	0.57%	0.07%	0.33%	0.08%
4	0.14%	0.19%	2.02%	0.35%	0.33%	0.05%	0.23%	0.06%
5	0.12%	0.17%	1.12%	0.23%	0.22%	0.04%	0.19%	0.05%
6	0.11%	0.15%	0.82%	0.19%	0.18%	0.03%	0.16%	0.04%
7	0.10%	0.14%	0.46%	0.17%	0.16%	0.03%	0.14%	0.04%
8	0.09%	0.13%	0.38%	0.15%	0.15%	0.03%	0.12%	0.03%

Table 3.4: (A). The relative error of the linear attenuation coefficient from simulated ideal detector model.

.	C3H6O	H2O	SiO2	NaCl	CaCl2
Bin 1	7.67%	1.49%	0.46%	-1.76%	-4.30%
Bin 2	1.74%	0.59%	1.23%	1.09%	0.46%
Bin 3	0.75%	0.31%	0.19%	0.34%	0.61%
Bin 4	0.84%	0.17%	-0.32%	-0.21%	0.57%

The corresponding linear attenuation coefficients (μ) from the NIST database are taken as the ground truth in the comparison.

Table 3.4: (B). The relative error of the linear attenuation coefficient from simulated realistic detector model.

	C3H6O	H2O	SiO2	NaCl	CaCl2
Bin 1	12.70%	-3.90%	-15.60%	-23.70%	-30.20%
Bin 2	2.20%	-0.90%	-3.10%	-5.30%	-7.30%
Bin 3	1.10%	0.30%	-0.10%	-0.20%	-0.20%
Bin 4	1.30%	0.30%	0.00%	0.60%	1.40%

The corresponding linear attenuation coefficients (μ) from the NIST database are taken as the ground truth in the comparison.

Table 3.4: (C). The relative error of the linear attenuation coefficient from physical experiment.

	C3H6O	H2O	SiO2	NaCl	CaCl2
Bin 1	3.30%	-9.60%	-20.50%	-29.30%	-27.90%
Bin 2	-5.50%	-7.50%	-6.30%	-9.00%	-9.20%
Bin 3	-3.00%	-2.10%	-3.40%	-1.80%	-7.10%
Bin 4	-2.90%	-1.70%	-3.90%	-2.10%	-2.70%

The corresponding linear attenuation coefficients (μ) from the NIST database are taken as the ground truth in the comparison.

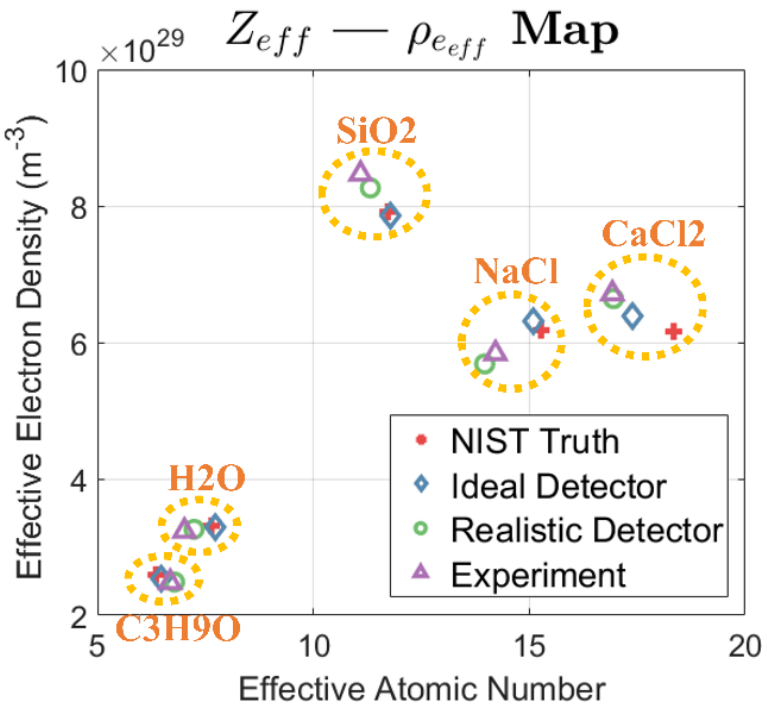

Figure 3.6: The calculated effective atomic number (Z_{eff}) and effective electron densities (ρ_e) for the five materials (acetone, water, silicon dioxide, sodium chloride, and calcium chloride) from different data. The red dots represent the results calculated based on the NIST database, which are taken as the ground truth; The blue dots represent the results calculated from the simulated PCCT data by the ideal detector model; The green dots represent the results calculated from the simulated PCCT data by the realistic detector model; The purple dots represent the results calculated from the physical experimental PCCT data.

Table 3.5: (A). The relative errors of the calculated effective atomic numbers (Z_{eff}) from different detector models.

	C3H6O	**H2O**	**SiO2**	**NaCl**	**CaCl2**
Ideal Detector Model	2.0%	1.5%	0.7%	-1.1%	-5.2%
Realistic Detector Model	6.7%	-5.2%	-3.4%	-8.6%	-7.6%
Physical Experiment	5.1%	-8.1%	-5.3%	-6.9%	-7.7%

The ground truth are the effective atomic numbers that are calculated from NIST database data.

Table 3.5: (B). The relative errors of the calculated effective electron densities ($\rho_{e_{eff}}$) from different detector models.

	C3H6O	**H2O**	**SiO2**	**NaCl**	**CaCl2**
Ideal Detector Model	-2.3%	-0.4%	-0.7%	2.3%	3.4%
Realistic Detector Model	-4.0%	-1.4%	4.5%	-8.0%	7.7%
Physical Experiment	-4.2%	-2.2%	7.1%	-5.5%	8.8%

The ground truth are the effective electron densities that are calculated from NIST database data.

3.5 Discussion and conclusion

In this study, we developed a model to calculate effective atomic number and effective electron density based on x-ray interaction physics. We validated the accuracy of the model for many different materials. Furthermore, we incorporated the model with PCCT data and demonstrated the feasibility of the model to achieve material separation and identification from PCCT image data.

As the validation of the model, we calculated Z_{eff} and $\rho_{e_{eff}}$ under various energy conditions for many materials. The result shows that, given a specific material, the calculated Z_{eff} and $\rho_{e_{eff}}$ from the model demonstrate good accuracy and robustness to different energy conditions (as shown in Table 3.3, most of the relative standard deviations are within 1%). The good accuracy of the model indicates that the model can be used to characterize different materials in an accurate and reliable manner.

To investigate the feasibility of incorporating the model with PCCT data, we conducted PCCT system simulation and physical experiment to generate PCCT data. In the simulation, we adopted a realistic detector model [29] that includes many detector degradation effects (photon noise and detector noise, charge sharing, K-escape x-ray, et al.) and also simulated an ideal detector that assumes perfect detector response as a comparison. As can be seen in Table 3.4, the detector degradation effects lead to the accuracy degradation of the attenuation values in the reconstructed images. For the simulated ideal detector model, the averaged absolute relative error across all the five materials and all the energy bins is 1.26%; for the simulated realistic detector model, the averaged absolute relative error is 5.52%; and for the physical experiment, the averaged absolute relative error is 7.94%.

The degraded attenuation value accuracy further leads to the degraded accuracy of the calculated Z_{eff} and $\rho_{e_{eff}}$. As listed in Table 3.5, the averaged absolute relative error of calculated Z_{eff} across all the five materials are 2.1% for simulated ideal detector model, 6.3% for simulated realistic detector model, and 6.6% for physical experiment. And the averaged absolute relative error of calculated $\rho_{e_{eff}}$ across all the five materials are 1.8% for simulated ideal detector model, 5.1% for simulated realistic detector model, and 5.6% for physical experiment. Despite of the degraded attenuation accuracy caused by detector degradation, all the five materials can still be well separated and easily identified in the $Z_{eff} - \rho_{e_{eff}}$ map (Figure 3.6), which demonstrates the feasibility of using the model for PCCT data to achieve the material identification.

The idea of employing effective atomic number to characterize materials has been explored by some previous studies since the introduction of PCCT [30-32]. But they have certain limitations. Firstly, the model they utilized to calculate effective atomic number is adapted from dual-energy CT [33, 34], which leads to different effective atomic number value under different energy condition. Secondly, the accuracy of their model varies largely for different materials. For example, the relative errors of calculated effective atomic number can be as small as 0.5% for Carbon and as large as 16.8% for Titanium as reported in [30]. Here we reported an improved model to calculate effective atomic number that is energy-invariant. The model retains good accuracy for a broad range of materials for that the model

is based on x-ray matter interaction physics. When applying the model with PCCT data, the highest error is reported to be 8.8%. An improved accuracy is achieved from our model.

The accuracy of the calculated Z_{eff} and $\rho_{e_{eff}}$ can be improved in a few ways. Firstly, we can increase the accuracy by using more energy bins. Because as more groups of (E, μ) combination are used to calculate Z_{eff} and $\rho_{e_{eff}}$, the better robustness to energy condition and higher error tolerance the model has. Secondly, we can increase the accuracy by narrowing down the energy bin width. In the PCCT system, we take the photons in each energy bin as quasi-monoenergetic photons and compute the effective energy (E_{eff}) as the photon energy in the energy bin, which is an approximation. The approximation can contribute to the error of the attenuation in reconstructed images, which will lead to the error of the calculated Z_{eff} and $\rho_{e_{eff}}$ eventually. Improvement of accuracy can be expected if we narrow down the energy bin width so that the effective energy (E_{eff}) can better represent the energy of all the photons in the energy bin. In our simulation and experiment, we used four energy bins and set the energy bin width to be 10 keV, which is a practical setup for the contemporary detector technique. More accurate calculated Z_{eff} and $\rho_{e_{eff}}$ can be expected as the detector technique advances in the future.

The model we developed in the study has certain limitation. The model cannot handle heavy materials well with very high effective atomic numbers. As can be observed in Table 3.3, as the effective atomic number becomes higher, the relative error becomes higher. In our study, we tested to calculate Z_{eff} for the Iodine using the model, and the calculated Z_{eff} is around 49, which is 7% off from the real atomic number of iodine itself (53). We think the discrepancy is because the model still has insufficient accuracy to handle the K-edge in the photoelectric absorption attenuation coefficient, which plays a significant role in the attenuation coefficient for heavy materials. But on the other hand, as shown in Table 3.3, our model demonstrates very good accuracy for materials with effective atomic number as high as 20 (Calcium). Since the mostly biological materials have effective atomic number lower than 20, the model can be applied to biological materials with relatively good accuracy.

In summary, we developed a model to calculate effective atomic number and effective electron density from PCCT data. The feasibility of incorporating the model with PCCT data was demonstrated by both PCCT simulation and experiment. Material identification can be achieved from the model in the $Z_{eff} - \rho_{e_{eff}}$ map. The model has the value to serve as a material identification scheme for PCCT system for practical use in the future.

3.6 Appendix

When an x-ray beam passes through an object, the intensity of the x-ray beam would be weakened due to the attenuation by the object. And the interaction between the x-rays and the imaged object is characterized by the Beer-Lambert law:

$$\frac{I}{I_0} = \exp(-\mu x) \tag{3.8}$$

where I is the intensity of the x-ray beam after the attenuation, I_0 is the intensity of the x-ray beam before the attenuation, and μ is the linear attenuation coefficient, which is determined jointly by the x-ray photon energy (E) and the intrinsic properties of the interacting material itself.

For single elements, the intrinsic properties of the material can be summarized as the atomic number (Z) and the electron density (ρ_e). According to the Hawkes and Jackson [23, 24], the linear attenuation coefficient (μ) of single elements can be parameterized by the following equation:

$$\mu(E, Z, \rho_e) = f(E, Z, \rho_e) = \rho_e(Z^4 F(E, Z) + G(E, Z)) \tag{3.9}$$

where $Z^4 F(E, Z)$ corresponds to the photoelectric cross-section, and $G(E, Z)$ corresponds to the scattering cross-section term, which includes both the coherent scattering and the incoherent scattering.

Hawkes and Jackson derived the equations of $F(E, Z)$ and $G(E, Z)$ from the scratch on the basis of the physics of the interaction between an x-ray photon and an electron [23, 24]. The final expression $F(E, Z)$ is summarized as:

$$\mathrm{F}(E,Z) = 4 * \sqrt{2} * \left(\frac{e^2}{\hbar c}\right)^4 * (m_e c^2)^{\frac{7}{2}} * \frac{\sigma^T}{E^{\frac{7}{2}}} * S(E,Z) * N(Z) * \left(1 + \mathcal{F}(\beta)\right) \quad (3.10)$$

where e is the electron charge, $\hbar$ is the Dirac constant, c is the light speed, m_e is the rest mass of an electron, r_e is the classical electron radius, σ^T represents the Thomson cross-section, which equals to $\frac{8*\pi}{3} r_e^2$, and the function of $N(Z)$ is screening constant table, which is listed in Jackson and Hawkes's study [24].

The function of $S(E,Z)$ is used to apply correction to the Born approximation from the Stobbe's study [35]:

$$S(E,Z) = 2\pi * \left(\frac{\varepsilon_K}{E - \varepsilon_K}\right)^{0.5} * \frac{\exp(-4 * n_1 * \cot^{-1} n1)}{1 - \exp(-2\pi * n_1)} \quad (3.11)$$

where $\varepsilon_K = \frac{Z^2 m_e e^4}{2\hbar^2}$, and $n_1 = \left(\frac{\varepsilon_K}{E - \varepsilon_K}\right)^{0.5}$.

The term of $(1 + \mathcal{F}(\beta))$ is used to incorporate the relativistic effects [36], which is expressed as: $1 + \mathcal{F}(\beta) = 1 + 0.143\beta^2 + 1.667\beta^8$, where $\beta = \sqrt{\frac{2E}{m_e c^2}}$.

As for the $G(E,Z)$ function, the final expression is summarized as:

$$G(E,Z) = \sigma^{KN} + \frac{(1 - Z^{b-1})}{Z} * \left(\frac{Z}{Z'}\right)^2 * \left(\frac{3}{8} * \sigma^T\right) * \int_{-1}^{1} (1 + \cos^2(\theta)) * [\mathbb{F}(\mathrm{x}, \mathrm{Z}')]^2 d(\cos(\theta)) \quad (3.12)$$

where Z' is the atomic number of a standard element serving as the reference to calculate the coherent scattering cross-section, $E' = (\frac{Z}{Z'})^{\frac{1}{3}} * E$, and b is the empirically established parameter that varies with different ranges of Z. We used $Z' = 8$ and $b = 0.5$ in our implementation, as suggested in the Hubbell's study [37] for the modeling of the soft tissue like materials.

σ^{KN} refers to the Klein-Nishina cross-section [38]. It is used to model the coherent scattering for the interaction between a photon and a free electron, the equation is expressed as:

$$\sigma^{KN} = 2\pi * r_e^2 * \left(\frac{1+k}{k^2} * \left(2 * \frac{1+k}{1+2k} - \frac{\ln(1+2k)}{k}\right) + \frac{\ln(1+2k)}{2k} - \frac{1+3k}{(1+2k)^2}\right) \quad (3.13)$$

where $k = \frac{E}{m_e c^2}$.

$\mathbb{F}(x, Z')$ is the atomic form factor function, where x is momentum-transfer variable, which equals to $\frac{\sin\left(\frac{\theta}{2}\right)}{\lambda(A)}$, and $\lambda(A)$ is the photon wavelength in angstroms, which equals to $\frac{12.398520}{E'(keV)}$. The detailed explanation can be found in Hubbell's study [37]. And θ is the angle between the photon directions of travel prior to and following a scattering interaction.

As a summary, using the above parameterization of $\mu(E, Z, \rho_e)$, the relationship of the linear attenuation coefficient μ, the x-ray photon energy E, and the atomic number (Z) and the electron density (ρ_e) for a single element is established.

References

[1] Z. Yu *et al.*, "Evaluation of conventional imaging performance in a research whole-body CT system with a photon-counting detector array," *Physics in Medicine & Biology*, vol. 61, no. 4, p. 1572, 2016.

[2] X. Wang, A. Zamyatin, and D. Shi, "Dose reduction potential with photon counting computed tomography," in *Medical Imaging 2012: Physics of Medical Imaging*, 2012, vol. 8313, p. 831349: International Society for Optics and Photonics.

[3] K. Taguchi and J. S. Iwanczyk, "Vision 20/20: Single photon counting x- ray detectors in medical imaging," *Medical physics*, vol. 40, no. 10, 2013.

[4] J. S. Butzer, A. P. H. Butler, P. H. Butler, P. J. Bones, N. Cook, and L. Tlustos, "Medipix imaging - evaluation of datasets with PCA," in *2008 23rd International Conference Image and Vision Computing New Zealand*, 2008, pp. 1-6.

[5] X. Wang, D. Meier, K. Taguchi, D. J. Wagenaar, B. E. Patt, and E. C. Frey, "Material separation in x- ray CT with energy resolved photon- counting detectors," *Medical physics*, vol. 38, no. 3, pp. 1534-1546, 2011.

[6] S. Leng *et al.*, "Spectral performance of a whole-body research photon counting detector CT: quantitative accuracy in derived image sets," *Physics in Medicine & Biology*, vol. 62, no. 17, p. 7216, 2017.

[7] K. C. Zimmerman and T. G. Schmidt, "Experimental comparison of empirical material decomposition methods for spectral CT," (in English), *Physics in Medicine and Biology*, vol. 60, no. 8, pp. 3175-3191, Apr 21 2015.

[8] Z. Li, S. Leng, L. Yu, Z. Yu, and C. H. McCollough, "Image-based material decomposition with a general volume constraint for photon-counting CT," in *Medical Imaging 2015: Physics of Medical Imaging*, 2015, vol. 9412, p. 94120T: International Society for Optics and Photonics.

[9] R. Symons *et al.*, "Photon- counting CT for simultaneous imaging of multiple contrast agents in the abdomen: an in vivo study," *Medical physics*, vol. 44, no. 10, pp. 5120-5127, 2017.

[10] X. Liu, L. Yu, A. N. Primak, and C. H. McCollough, "Quantitative imaging of element composition and mass fraction using dual- energy CT: Three- material decomposition," *Medical physics*, vol. 36, no. 5, pp. 1602-1609, 2009.

[11] L. I. R. Garcia, J. F. P. Azorin, and J. F. Almansa, "A new method to measure electron density and effective atomic number using dual-energy CT images," *Physics in Medicine & Biology*, vol. 61, no. 1, p. 265, 2015.

[12] D.-H. Kim, W.-H. Lee, S.-S. Jeon, and H.-J. Kim, "Absolute measurement of the effective atomic number and the electron density by using dual-energy CT images," *Journal of the Korean Physical Society*, vol. 61, no. 12, pp. 2042-2048, 2012.

[13] R. Murty, "Effective atomic numbers of heterogeneous materials," *Nature*, vol. 207, no. 4995, p. 398, 1965.

[14] R. E. Latchaw, J. T. Payne, and L. Gold, "Effective atomic number and electron density as measured with a computed tomography scanner: computation and correlation with brain tumor histology," *Journal of computer assisted tomography*, vol. 2, no. 2, pp. 199-208, 1978.

[15] R. Rutherford, B. Pullan, and I. Isherwood, "Measurement of effective atomic number and electron density using an EMI scanner," *Neuroradiology*, vol. 11, no. 1, pp. 15-21, 1976.

[16] U. Schneider, E. Pedroni, and A. Lomax, "The calibration of CT Hounsfield units for radiotherapy treatment planning," *Physics in Medicine & Biology*, vol. 41, no. 1, p. 111, 1996.

[17] Z. Qi, J. Zambelli, N. Bevins, and G.-H. Chen, "Quantitative imaging of electron density and effective atomic number using phase contrast CT," *Physics in Medicine & Biology*, vol. 55, no. 9, p. 2669, 2010.

[18] M. Taylor, R. Smith, F. Dossing, and R. Franich, "Robust calculation of effective atomic numbers: The Auto-Zeff software," *Medical physics*, vol. 39, no. 4, pp. 1769-1778, 2012.

[19] V. P. Singh, N. Badiger, and N. Kucuk, "Determination of effective atomic numbers using different methods for some low-Z materials," *Journal of Nuclear Chemistry*, vol. 2014, 2014.

[20] S. R. Manohara, S. M. Hanagodimath, K. S. Thind, and L. Gerward, "On the effective atomic number and electron density: A comprehensive set of formulas for all types of materials and energies above 1 keV," *Nuclear Instruments and Methods in Physics Research Section B: Beam Interactions with Materials and Atoms*, vol. 266, no. 18, pp. 3906-3912, 9// 2008.

[21] S. R. Manohara, S. M. Hanagodimath, and L. Gerward, "Studies on effective atomic number, electron density and kerma for some fatty acids and carbohydrates," *Phys Med Biol*, vol. 53, no. 20, pp. N377-86, Oct 21 2008.

[22] P. Duvauchelle, G. Peix, and D. Babot, "Effective atomic number in the Rayleigh to Compton scattering ratio," *Nuclear Instruments and Methods in Physics Research Section B: Beam Interactions with Materials and Atoms*, vol. 155, no. 3, pp. 221-228, 1999.

[23] D. Hawkes and D. F. Jackson, "An accurate parametrisation of the x-ray attenuation coefficient," *Physics in Medicine & Biology*, vol. 25, no. 6, p. 1167, 1980.

[24] D. F. Jackson and D. J. Hawkes, "X-ray attenuation coefficients of elements and mixtures," *Physics Reports*, vol. 70, no. 3, pp. 169-233, 1981.

[25] J. H. Hubbell and S. M. Seltzer, "Tables of X-ray mass attenuation coefficients and mass energy-absorption coefficients 1 keV to 20 MeV for elements Z= 1 to 92 and 48 additional substances of dosimetric interest," National Inst. of Standards and Technology-PL, Gaithersburg, MD (United States). Ionizing Radiation Div.1995.
[26] G. Poludniowski, G. Landry, F. DeBlois, P. Evans, and F. Verhaegen, "SpekCalc: a program to calculate photon spectra from tungsten anode x-ray tubes," *Physics in medicine and biology,* vol. 54, no. 19, p. N433, 2009.
[27] R. L. Siddon, "Fast calculation of the exact radiological path for a three-dimensional CT array," *Med Phys,* vol. 12, no. 2, pp. 252-5, Mar-Apr 1985.
[28] J. Cammin, S. G. Kappler, T. Weidinger, and K. Taguchi, "Evaluation of models of spectral distortions in photon-counting detectors for computed tomography," *Journal of Medical Imaging,* vol. 3, no. 2, p. 023503, 2016.
[29] K. Taguchi, K. Stierstorfer, C. Polster, O. Lee, and S. Kappler, "Spatio- energetic cross-talk in photon counting detectors: Numerical detector model (PcTK) and workflow for CT image quality assessment," *Medical physics,* 2018.
[30] W. Zou *et al.*, "Atomic number and electron density measurement using a conventional x-ray tube and a cdte detector," *Japanese journal of applied physics,* vol. 47, no. 9R, p. 7317, 2008.
[31] K. Kan, Y. Imura, H. Morii, K. Kobayashi, T. Minemura, and T. Aoki, "Application of photon-counting X-ray computed tomography to aluminum-casting inspection," *World Journal of Nuclear Science and Technology,* vol. 3, no. 03, p. 106, 2013.
[32] Y. Yamashita *et al.*, "Measurement of effective atomic numbers using energy-resolved computed tomography," *Journal of Nuclear Science and Technology,* vol. 51, no. 10, pp. 1256-1263, 2014/10/03 2014.
[33] M. Torikoshi *et al.*, "Design of synchrotron light source and its beamline dedicated to dual-energy x-ray computed tomography," *journal of Biomedical Optics,* vol. 6, no. 3, pp. 371-377, 2001.
[34] T. Tsunoo *et al.*, "Measurement of electron density and effective atomic number using dual-energy x-ray CT," in *Nuclear Science Symposium Conference Record, 2004 IEEE*, 2004, vol. 6, pp. 3764-3768: IEEE.
[35] M. Stobbe, "Zur quantenmechanik photoelektrischer prozesse," *Annalen der Physik,* vol. 399, no. 6, pp. 661-715, 1930.
[36] F. Sauter, "Über den atomaren Photoeffekt bei großer Härte der anregenden Strahlung," *Annalen der Physik,* vol. 401, no. 2, pp. 217-248, 1931.
[37] J. Hubbell, W. J. Veigele, E. Briggs, R. Brown, D. Cromer, and d. R. Howerton, "Atomic form factors, incoherent scattering functions, and photon scattering cross sections," *Journal of physical and chemical reference data,* vol. 4, no. 3, pp. 471-538, 1975.
[38] O. Klein and Y. Nishina, "Über die Streuung von Strahlung durch freie Elektronen nach der neuen relativistischen Quantendynamik von Dirac," *Zeitschrift für Physik,* vol. 52, no. 11-12, pp. 853-868, 1929.

Chapter 4 Deep learning correction for PCCT data distortion

Xu Dong, and Guohua Cao

Department of Biomedical Engineering and Mechanics, Virginia Polytechnic Institute and State University, Blacksburg, VA 24061, USA.

Publication information – The major contents of this chapter were from the under-preparation manuscript: X. Dong, and G. Cao, "A correction method for photon counting CT data distortion with deep learning neural network," Medical Physics, 2019

4.1 Abstract

Photon counting computed tomography (PCCT) has reportedly demonstrated significantly better imaging performance compared to conventional CT. As PCCT appears to be a significant breakthrough in CT imaging field, there exists severe data distortion problem in PCCT, which greatly limits the application of PCCT in practice. The foundation of the PCCT data distortion can be divided into two distinct process: detector sensor response and pulse pileup. While pulse pileup caused data distortion can be avoid by controlling x-ray flux, the detector sensor response caused data distortion is inherent to detector and cannot be avoided. In this study, we focus on developing an approach to correct the distortion caused by detector sensor response. Lately, deep learning (DL) neural network has demonstrated tremendous success in medical imaging field. In this paper, we propose a correction method for PCCT data distortion based on deep learning neural network. First, we conducted PCCT simulation to generate sufficient PCCT data for network training from a public clinical CT dataset. Second, we optimized the neural network design by making the network to process each individual sinogram view. After the algorithm was trained,

when applying the algorithm to process the test dataset data, the accuracy of the PCCT data can be greatly improved (RMSE improved 73.7%). Compared with traditional data correction approaches such as maximum likelihood, the deep learning approach demonstrate superiority in terms of RMSE, SSIM, PSNR, and most importantly, runtime (4053.21 sec vs. 1.98 sec). The proposed method has the potential to facilitate the PCCT studies and applications in practice.

Keywords: Molecular imaging, X-ray fluorescence, Molecular sensitivity

4.2 Introduction

Recently photon counting computed tomography (PCCT) has reportedly demonstrated significantly better imaging performance compared to conventional CT [1-3]. PCCT utilize photon counting detector that is capable of discriminating photon energy. Using photon counting detector, the photon can be recognized individually and the energy of the photon can be distinguished and sorted into several energy bins. Therefore, PCCT can generate much richer image data that contains spectral information inside compared to conventional CT. Many applications have been derived based on PCCT, such as the material identification/separation [4, 5], material decomposition [6, 7], and so on.

As PCCT appears to be a significant breakthrough in CT imaging field, there exists severe data distortion problem in PCCT [8, 9]. Due to the limitation of current detector technique, there are many degradation factors such as charge sharing and pulse pileup that contributes the PCCT data distortion, which greatly diminish the applications of PCCT. For example, our previous study shows that serious pixel value deviation was observed in the reconstructed PCCT images due to the PCCT data distortion [5]. When using the distorted PPCT data for material identification, the error can be as high as 4.84%, as compared to the error of 0.39% without data distortion [5]. Therefore, to promote its application in practice, it is critical to address the data distortion problem in PCCT.

The foundation of the PCCT data distortion can be divided into two distinct processes: detector sensor response and pulse pileup [10, 11]. The detector sensor response is used to

model the physical processes of capturing an x-ray photon by the detector sensor and converting the photon energy to electronic signal. The pulse pileup is used to model the processing of electronic signals in integrated circuit. Many studies have been conducted to model the data distortion in the two processes [10-15]. Generally speaking, the detector sensor response is reliant on the detector intrinsic setting, while the pulse pileup is totally dependent on the incident x-ray flux. The distortion caused by the pulse pileup only became obvious when the x-ray flux is too high compared to the dead time of the detector, and therefore can be prevented by using a small x-ray flux in practice. On the other hand, the distortion caused by the detector sensor response involves many physical processes such as the K-escape x-ray, fluorescence reabsorption, electronic cloud movement, and so on. The distortion caused by those phenomena is complicated and inherent to the detector, and therefore the distortion is hard to be avoided during data acquisition and has to be corrected by other approaches. In this study, we focus on developing an approach to correct the distortion caused by the detector sensor response.

Previously, some researches have been conducted to tackle the data distortion problem [16-21]. For example, Lee et al developed an estimator based on x-ray transmittance model [16]; Schmidt et al developed an optimization algorithm to estimate the basis material maps [17]; Rodesch et al proposed a PCCT image reconstruction method based on the photon counting detector model [18]. However, all the studies involve using iterative methods for distortion correction, which lead to great computational cost of using those methods.

Deep learning neural network has demonstrated tremendous success in medical imaging field in recent years [22-24]. Even though the exact theoretical foundation is not well understood yet, it has the ability to extract the intrinsic feature in the data and transform the input data into desired output after learning in a considerably big dataset [25, 26]. Furthermore, once a neural network is trained well, applying the network to process data can be fairly fast compared to iterative approaches. In this study, we will develop a deep learning based approach to correct the PCCT data distortion.

The paper is organized as follows. After the introduction, in section II we explained the data preparation and the PCCT simulation, the neural network design and the network

training, and the evaluation of the approach in test dataset. The results are shown in section III, and discussions and conclusions are in section IV.

4.3 Methods

4.3.1 Method overview

A shown in Figure 4.1, we applied the neural network to process the PCCT sinograms. To generate a large dataset for network training, a PCCT system was simulated in the study and PCCT data were generated from clinical CT images. A realistic detector model and an ideal detector model were separately used in the simulation. A deep learning neural network was developed to process the PCCT data from realistic detector model, with the goal to improve the accuracy to be as close as to the PPCT data from ideal detector model.

The network was first trained in training dataset in a supervised way. Then the network was used to process the sinograms in the test dataset. After reconstructing the sinograms into images, we evaluated the image quality in both sinogram domain and reconstructed image domain.

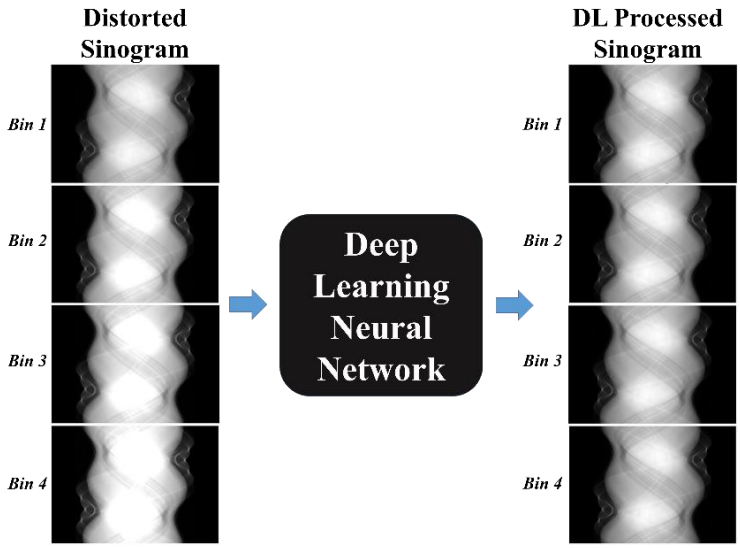

Figure 4.1: The overview of the method. The deep learning neural network is used to process the sinogram from the distorted PCCT data.

4.3.2 Simulation data generation

A total of 471 two-dimensional clinical CT images were obtained from National Biomedical Imaging Archive (NBIA) [27] for PCCT simulation. The CT images are acquired from several parts of human body, which include 22% head, 35% chest, 35% abdomen, and 8% hip. The images are in DICOM format with 512×512 pixels per image, where the image pixel values are the Hounsfield unit numbers (HU number).

To utilize the DICOM images for photon counting CT simulation, we need to convert them into attenuation maps where the image pixel values are attenuation coefficients. Therefore, we preprocessed the raw clinical CT images in two steps. First, we decomposed each raw image into four basis materials: air, fat, muscle, and bone. The HU numbers for air, fat, muscle and bone were considered to be -1000, -100, 50, and 3000 respectively. The decomposition was achieved by decomposing each image pixel into a linear combination of any one or two of the four material based on the pixel's HU number. For example, for a pixel with HU number between -1000 (HU number of air) and -100 (HU number of fat), the pixel was taken as the linear combination of air and fat; for a pixel with HU number beyond 3000, the pixel was taken as bone only, and the corresponding weight coefficient was computed based on its specific HU number.

After the decomposition, one air basis image, one fat basis image, one muscle basis image, and one bone basis image can be obtained from one raw CT image. The attenuation coefficient of the four basis materials can be obtained from NIST database [28]. Then we constructed the attenuation maps by combing the material basis images and the corresponding attenuation coefficient. We calculated the attenuation maps under the energy from 20 keV to 150 keV with the increment of 1 keV. The attenuation maps then can be used for PCCT simulation.

4.3.3 PCCT system simulation

We simulated a small clinical phan-beam CT system. The illustration of the system is shown in Figure 4.2 and the simulation setup is listed in Table 4.1. Once the excitation beam was generated by SpekCalc [29], the line-based Siddon's algorithm [30] was used to calculate the attenuation for each ray during the forward projecting process.

The data distortion is caused by the detector response. A realistic photon counting detector includes many degradation factors such as photon noise and detector noise, fluorescence reabsorption, K-escape x-ray, et al., and those degradation factors eventually contribute to the distortion in PCCT data. Taguchi et al. developed a numerical detector model to simulate the data distortion in the detector sensor response process, which shows good agreement with experimental data [31]. As a result, we adapted the model in our simulation to simulate a realistic detector response.

On the other hand, we also simulated an ideal detector with perfect detector response, which simply assumes that the detector loyally outputs the spectrum incident on it without any distortion. The PCCT data from ideal detector model were taken as the reference in the study.

We set four energy bins in the simulation, from 40 keV to 80 keV with the energy bin width as 10 keV. After preprocessing in section II.2, the 471 CT images were taken as 471 different objects to be scanned by the PCCT system. Each scan generated a sinogram with the size of $4 \times 1024 \times 720$, corresponding to the 4 energy bins, the 1024 detector pixels, and the 720 views per scan, respectively. Then the sinograms were reconstructed by filtered backprojection (FBP) algorithm, which eventually generated images with the size of $4 \times 512 \times 512$, where 4 is the number of energy bins, and 512×512 is the image size under each energy bin.

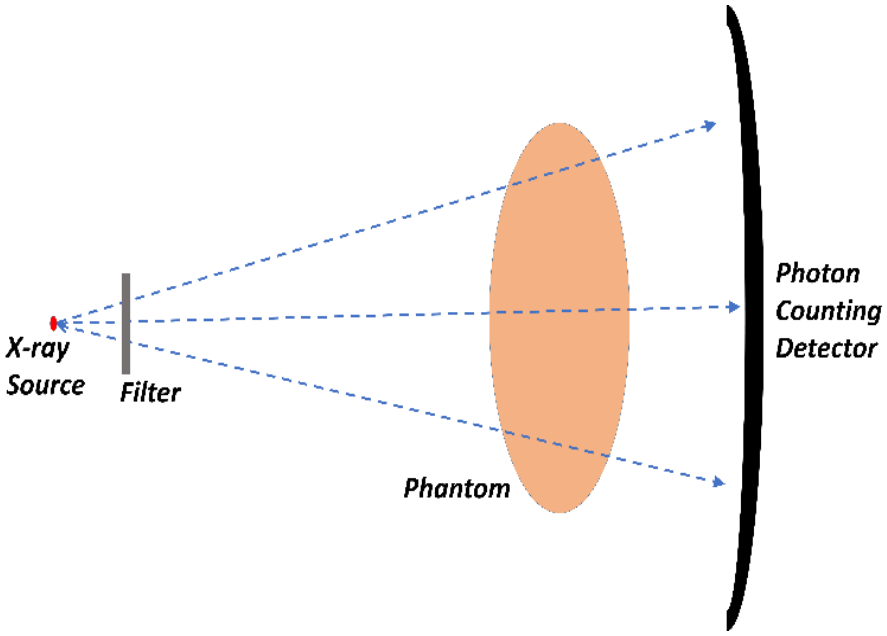

Figure 4.2: The schematic of the simulated PCCT system.

Table 4.1: Parameters of the PCCT system simulation.

Source voltage	80 kV
Filter	2.10 mm Aluminum
Source to isocenter distance	500 mm
Source to detector distance	900 mm
Detector pixel size	0.75 mm
Detector resolution	1024 pixels
Data acquisition	2 projections per degree 720 projections in total
Photon statistics	1.0e6 photons per ray

4.3.4 Data preparation for network training

The 471 CT images were randomly divided into training dataset (320 images), validation dataset (32 images), and test dataset (119 images), which roughly account for 68%, 7%, and 25% of the whole dataset respectively. For the network training, instead of training the neural network on reconstructed images or sinograms, we chose to train the network on each individual sinogram view. Our choice is based on two reasons.

First, the data distortion comes from the imperfect detector response, which directly affects the sinograms and then subsequently affects the reconstructed images after reconstruction. Therefore, training the network on sinograms rather than reconstructed images can be more

effective to learn the distortion pattern caused by the detector. On the other hand, even though the data distortion has an impact both spatially in neighboring pixels and energetically in different energy bins, the impact is independent to each individual sinogram view. In other words, the signal from each detector pixel under each energy bin is correlated to the signal from its neighboring pixels and other energy bins within the same view, while it is irrelevant to the signal in different sinogram views. As a result, training the network on each individual sinogram view would be effective and sufficient to force the network to learn the distortion pattern. Second, each sinogram view has the size of 4×1024, which is much smaller than the whole sinogram size and the reconstructed image size. Training on sinogram view requires much less computational power and therefore makes the method more accessible to broader usages.

We also conducted data selection in the training dataset. Considering the angular step was set to be 0.5 degree in PCCT data collection, the adjunct sinogram views would share great similarities. To enable the network to learn the data distortion pattern with the generalization ability, we want to train the network by as much variety of data as possible, instead of very similar data. As a result, we sampled one sinogram view in in every ten views such that only one tenth of the training data were actually used for training. By sampling the sinogram views in a sample rate of 10, we can reduce the redundant data to promote the neural network's generalization ability. On the other hand, the training process also gets facilitated when having a smaller dataset.

4.3.5 Convolutional neural network

Convolutional neural network (CNN) is one of the most successful deep learning methods to extract features in the data. In this study, we constructed a successive convolutional neural network. Fourteen convolutional layers were used in our network, and each convolutional layer was followed by a ReLu activation layer except the last layer. We set the convolutional kernel size to be 4 by 4 and the stride to be 1. The size of the data was maintained the same in every layer, while the number of feature channels was set to be 32 for the head layer, 64 for the body layers, and 1 for the output layer. The architecture of the network and structural parameters are shown in Figure 4.3.

The residual learning technique was used in the network. The input data was added onto the output of the 14 successive convolution layers, and the summation was taken as the eventual output of the network. Such design can force the network to learn the difference between the input data and the reference data instead of direct mapping. The residual learning can improve the convergence and facilitate training.

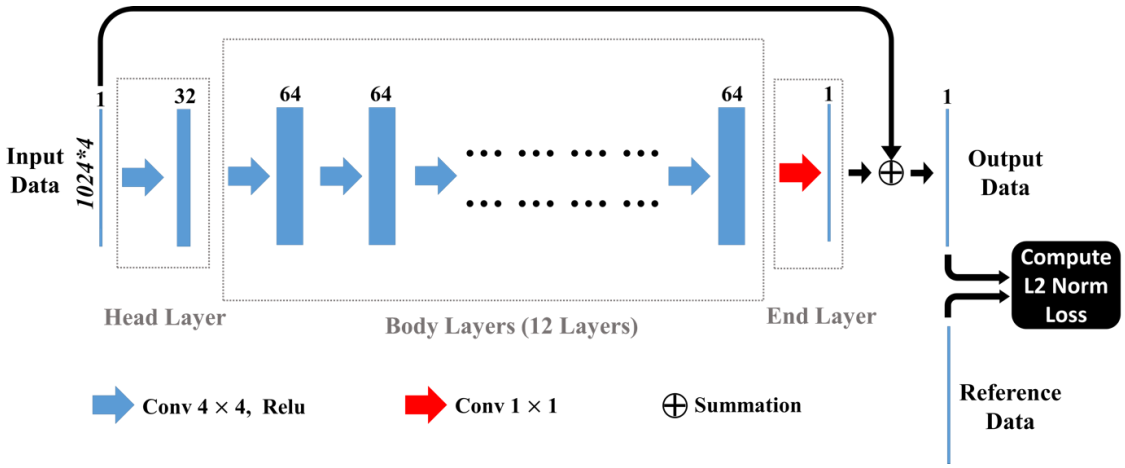

Figure 4.3: The architecture of the proposed neural network.

4.3.6 Network training

The sinograms from realistic detector model were feed into the network, then the output of the network were compared with sinograms from ideal detector model (reference data). The L2 norm was calculated and used as the loss function. The network updates its parameter in every epoch with the objective to minimize the loss function.

The stochastic gradient descent (SGD) optimizer was used to optimize the network. The learning rate was set to be 0.2 initially, and decays 0.8 in every 500 steps. The algorithm was implemented in Python based on TensorFlow. The training was done on a workstation with Intel Core i5-7400 CPU and 16GB RAM. A GPU card (Nvidia GTX Titan X) accelerated the training process. All the convolution and deconvolution filters were initialized with random Gaussian distributions with zero mean and 0.01 standard deviation.

4.3.7 Evaluation

After the neural network being trained in the training dataset, it is applied to the test dataset to correct the distortion. In this study, we also applied maximum likelihood method [32,

33] for data distortion based on the detector model. We compared the sinogram from realistic detector model (realistic sinogram), the sinogram corrected by maximum likelihood method (ML processed sinogram), the sinogram processed by the proposed deep learning method (DL processed sinogram), and the sinogram from ideal detector model (reference sinogram). The comparison is illustrated in Figure 4.4, and Figure 4.5.

The sinograms were reconstructed by FBP algorithm. Figure 4.6 shows the image reconstructed from realistic sinogram (realistic image), the image reconstructed from ML processed sinogram (ML processed image), the image reconstructed from DL processed sinogram (DL processed image), and the image reconstructed from reference sinogram (reference image). Figure 4.7 shows the difference image of realistic image and reference image, the difference image of ML processed image and reference image, and the difference image of DL processed image and reference image.

We also made quantitative analysis of reconstructed images. The line-profiles of the central horizontal lines (the corresponding position is indicated in Figure 4.6) were plotted in Figure 4.8. In comparison with reference images, the root mean square error (RMSE), structural similarity (SSIM), and peak signal to noise ratio (PSNR) were calculated for realistic images, ML processed images, and DL processed images. The result is reported in Table 4.2.

4.4 Results

4.4.1 The evaluation of sinograms

Figure 4.4 shows examples of a realistic sinogram, a ML processed sinogram, a DL processed sinogram, and a reference sinogram. After subtracting reference sinogram, the difference images for realistic sinogram, ML processed sinogram, and DL processed sinogram are shown in Figure 4.5. We can see that the both maximum likelihood approach and deep learning approach can improve the accuracy of sinograms based on visual comparison.

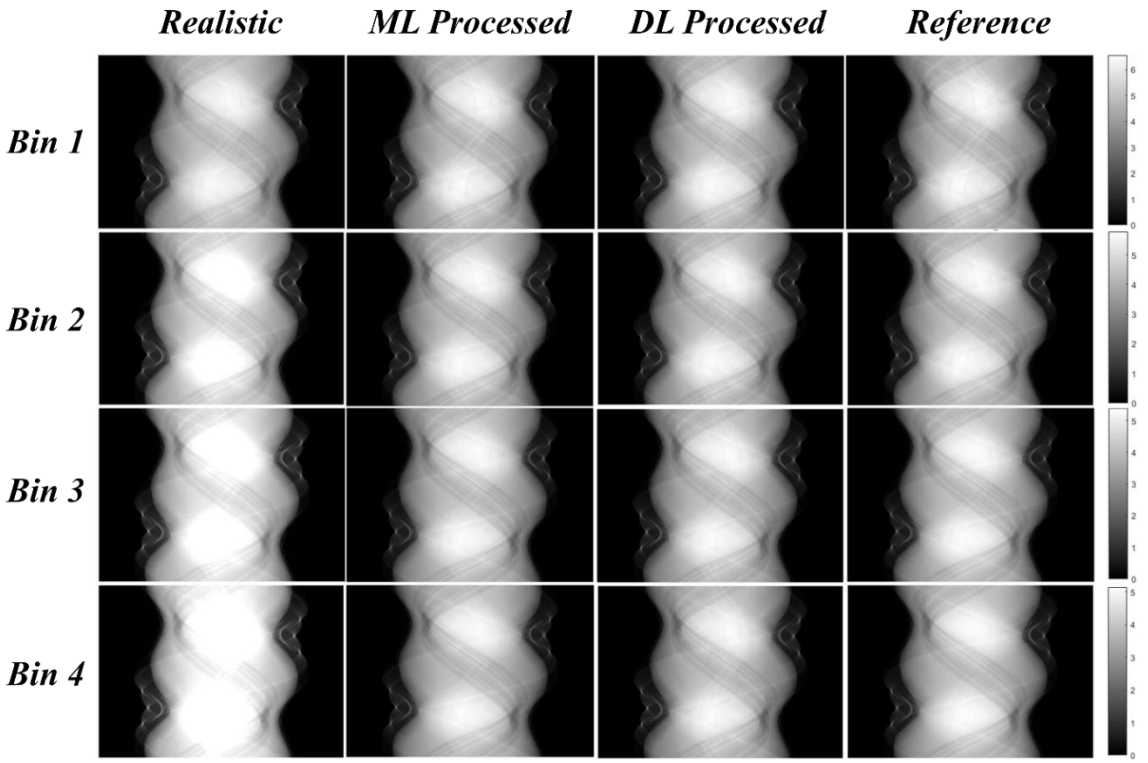

Figure 4.4: The example of sinograms. Each column from left to right represents the realistic sinograms, ML processed sonograms, DL processed sinograms, and reference sinograms. Each row represent the sinograms under each energy bin. The display window for sinograms in each row is the same, as shown on the rightmost.

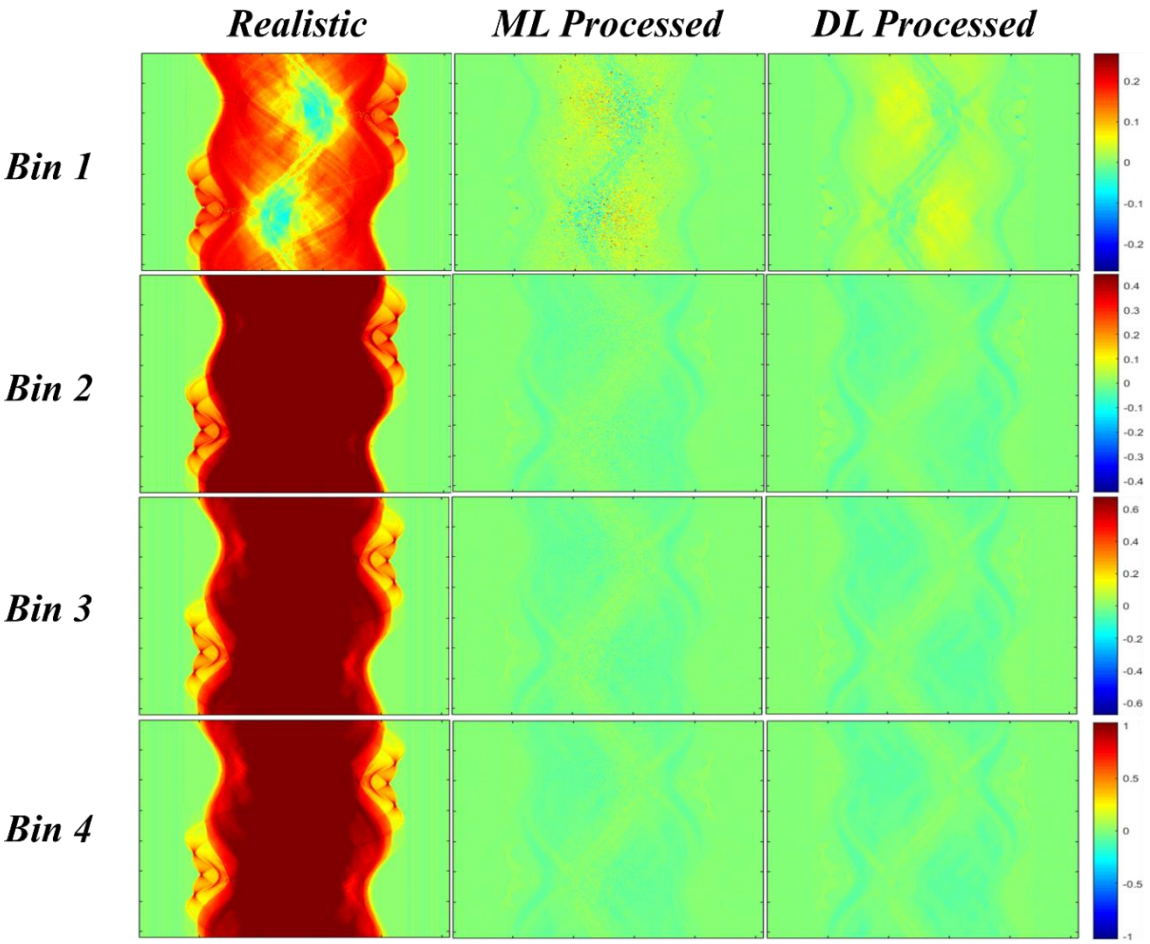

Figure 4.5: After subtracting the reference sinograms, the difference images of realistic sinograms (left column), ML processed sonograms (middle column), and DL processed sinograms (right column). Each row represent the sinograms under each energy bin. The display window for sinograms in each row is the same, as shown on the rightmost.

4.4.2 The evaluation of reconstructed images

Figure 4.6 shows a realistic image, a ML processed image, a DL processed image, and a reference image. The difference images are shown in Figure 4.7. Based on visual comparison, the ML processed image and the DL processed image are numerically much closer to the reference image than the realistic image.

As for quantitative analysis, the line-profiles are shown in Figure 4.8. It also confirms that both maximum likelihood approach and deep learning approach can reduce the numerical error of the realistic image. As can be seen in the line-profiles, compared with maximum likelihood approach, the image processed by deep learning approach is less noisy and numerically closer to reference image.

Table 4.2 shows the RMSE, SSIM, and PSNR for realistic images, ML processed images, and DL processed images, when compared with references images in the test dataset. When using maximum likelihood to correct data distortion, the RMSE is improved from 0.00243 to 0.00090, SSIM is improved from 99.15% to 99.90%, and the PSNR is improved from 51.57 to 60.86. On the other hand, when using deep learning to correct data distortion, the RMSE is improved to 0.00058, SSIM is improved to 99.99%, and PSNR is improved to 64.71.

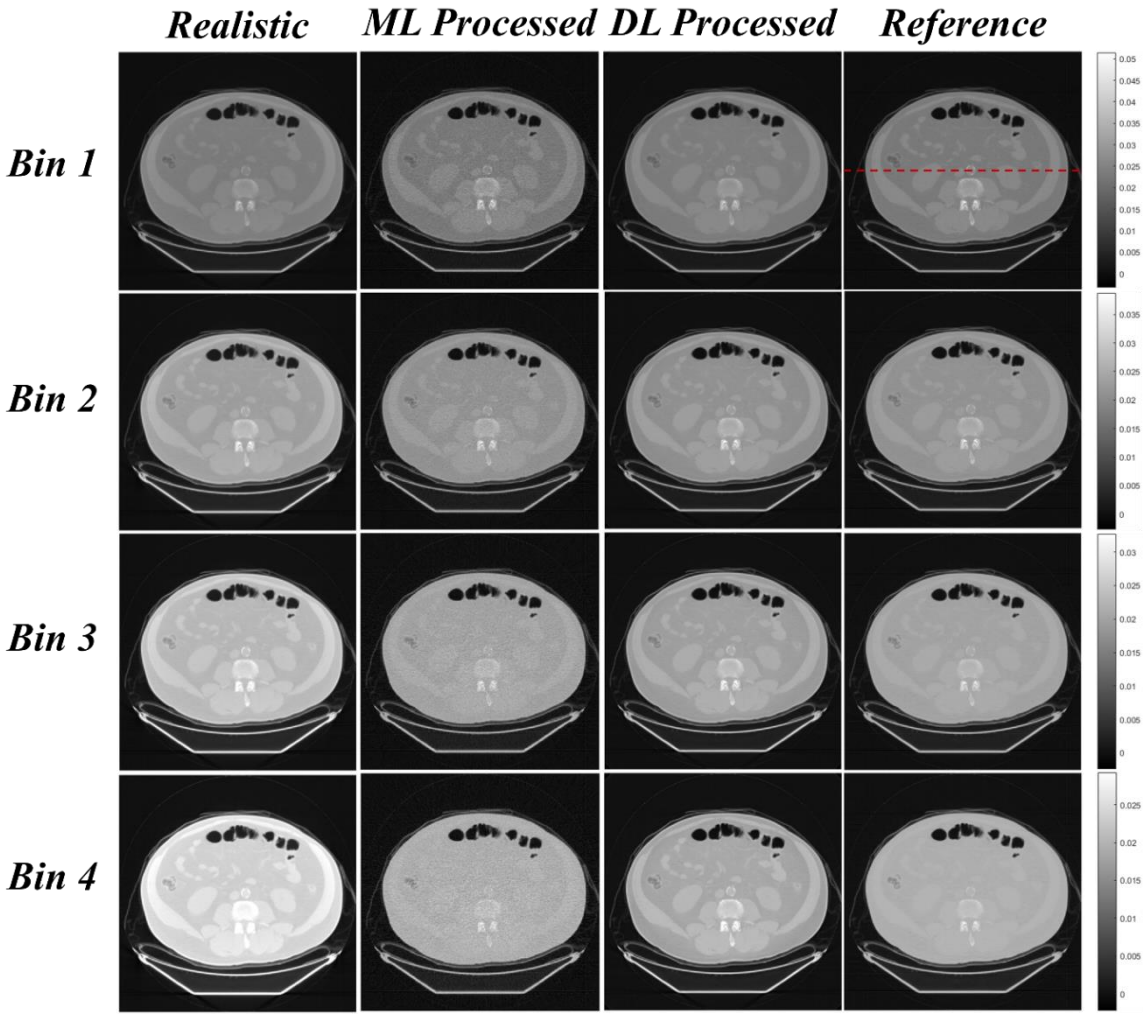

Figure 4.6: The reconstructed images. Each column from left to right represents the realistic images, ML processed images, DL processed images, and reference images. Each row represent the images under each energy bin. The display window for images in each row is the same, as shown on the rightmost, and the unit is mm^{-1}. (The red dashed line is used to indicate the position of the line profiles plotted in Figure 4.8.)

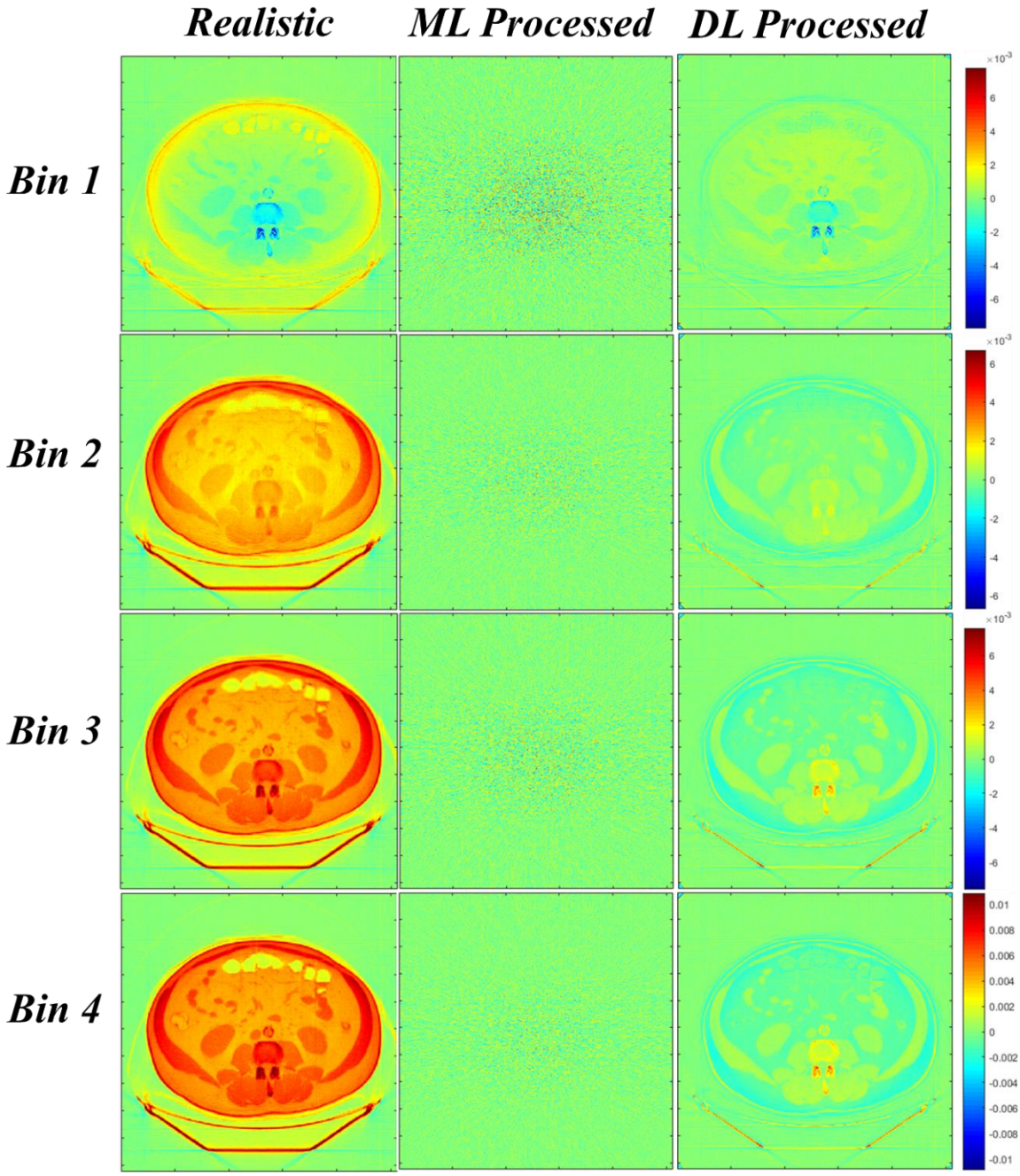

Figure 4.7: After subtracting the reference images, the difference images of realistic images (left column), ML processed images (middle column), and DL processed images (right column). Each row represent the images under each energy bin. The display window for images in each row is the same, as shown on the rightmost, and the unit is mm^{-1}.

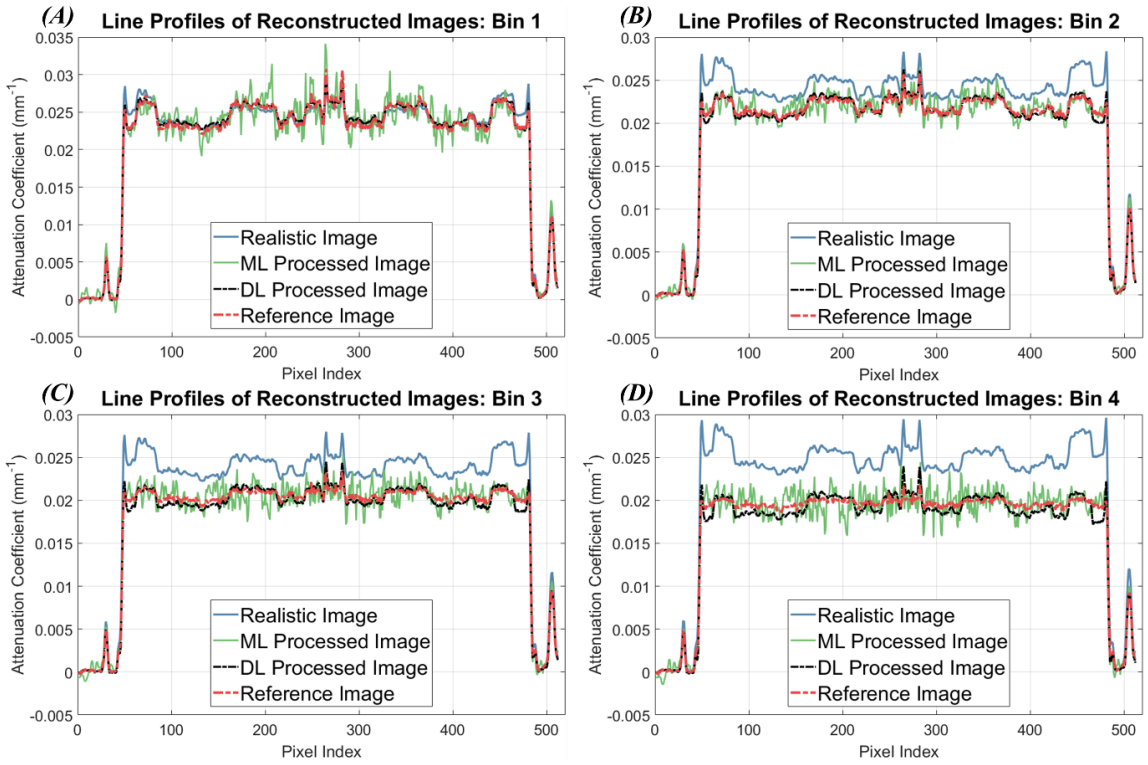

Figure 4.8: The line profiles of the images in Figure 4.6. The plot (A), (B), (C), and (D) represent to energy bin 1, 2, 3, and 4, respectively. The position of the line profile in the image is indicated as a red dashed line in Figure 4.6.

Table 4.2: The RMSE, SSIM, PSNR, and runtime of realistic images and DL processed images averaged across the whole test dataset.

	Realistic Images	ML processed Images	DL processed Images
RMSE	0.00243	0.00090	**0.00058**
SSIM	99.15%	99.90%	**99.99%**
PSNR	51.57	60.86	**64.71**
Runtime	N/A	4053.21 sec.	**1.98 sec.**

4.5 Discussion and conclusion

In this study, we developed a PCCT data distortion correction approach based on deep learning neural network. When applying the algorithm to process the test dataset data, the accuracy of both sinograms and reconstructed images were greatly improved. For the reconstructed images in the whole test dataset, the averaged RMSE was improved from

0.00243 to 0.00058, the averaged SSIM was improved from 99.15% to 99.99%, and the averaged PSNR was improved from 51.57 to 64.71.

To provide a large dataset for network training, we simulated a PCCT system and used clinical CT images in a public dataset to be as scan objects. We used a realistic detector model to simulate the data distortion in PCCT and also used an ideal detector model to serve as the reference. Therefore, the network was trained in the supervised way with the pairs of the distorted PCCT data and the reference PCCT data.

The network was designed to process each individual sinogram view rather than the reconstructed image or the sinogram as a whole. The benefits of the design are in two folds. First, because the distortion caused by the detector response happens independently in each sinogram view, it makes the correction more effective by directly targeting on the signal distortion in each view. Second, it also makes the approach more accessible because the method becomes more lightweight when the size of the processed data is smaller. The data selection was further performed in the training dataset. One sinogram view was sampled in every ten views to be actually used for network training. The redundancy of the data can be reduced by doing data selection, which can hence promote the generalization capability of the network and facilitate the training as well.

Data distortion in PCCT is one major obstacle that limits the usage of PCCT from broader applications [8, 9, 34]. To overcome the obstacle, many researches have been conducted to correct distortion based on analytical models and iterative methods [16-19, 35, 36]. In this study, a deep learning neural network based approach is proposed. Compared with conventional iterative approaches such as maximum likelihood, the deep learning approach developed in this study produces greater improvement in terms of RMSE, SSIM, and PSNR (as reported in Table 4.2). Furthermore, once the neural network finishes training, the computational cost of deep learning approach is much less than the computational cost of iterative approaches. For example, when we deployed our algorithm on the person workstation, the deep learning approach takes only 1.98 sec. on average to process one PCCT sinogram (in size of 4×1024×720), while the maximum likelihood approach takes 4053.21 sec. to process one PCCT sinogram.

The approach we developed for PCCT data correction has certain limitations. Even though the detector model we used to simulate the distortion includes lots of degradation factors such as the charge sharing and K-escape x-rays, and so on, the pulse pileup effect is not included in the model. The pulse pileup can have a significant effect on the PCCT data distortion when the x-ray flux is higher than the detector's dead time. Many researches were conducted to study the pulse pileup effect and some numerical models have been developed [15, 37, 38]. Based on the models, incorporating the pulse pileup effect correction into our PCCT data correction algorithm will be the future of our study.

In conclusion, a deep learning neural network based method was developed in the study to correct the PCCT data distortion. The accuracy of the PCCT data can be greatly improved (RMSE improved 73.7%) by using the method. The proposed method has the potential to facilitate the PCCT studies and applications in practice.

References

[1] Z. Yu *et al.*, "Evaluation of conventional imaging performance in a research whole-body CT system with a photon-counting detector array," *Physics in Medicine & Biology,* vol. 61, no. 4, p. 1572, 2016.

[2] X. Wang, A. Zamyatin, and D. Shi, "Dose reduction potential with photon counting computed tomography," in *Medical Imaging 2012: Physics of Medical Imaging*, 2012, vol. 8313, p. 831349: International Society for Optics and Photonics.

[3] M. J. Willemink, M. Persson, A. Pourmorteza, N. J. Pelc, and D. Fleischmann, "Photon-counting CT: technical principles and clinical prospects," *Radiology,* vol. 289, no. 2, pp. 293-312, 2018.

[4] X. Wang, D. Meier, K. Taguchi, D. J. Wagenaar, B. E. Patt, and E. C. Frey, "Material separation in x ‐ ray CT with energy resolved photon ‐ counting detectors," *Medical physics,* vol. 38, no. 3, pp. 1534-1546, 2011.

[5] X. Dong, O. V. Pen, Z. Zhang, and G. Cao, "An improved physics model for multi-material identification in photon counting CT," in *Medical Imaging 2019: Physics of Medical Imaging*, 2019, vol. 10948, p. 109484O: International Society for Optics and Photonics.

[6] Z. Li, S. Leng, L. Yu, Z. Yu, and C. H. McCollough, "Image-based material decomposition with a general volume constraint for photon-counting CT," in *Medical Imaging 2015: Physics of Medical Imaging*, 2015, vol. 9412, p. 94120T: International Society for Optics and Photonics.

[7] S. Lee, Y.-N. Choi, and H.-J. Kim, "Quantitative material decomposition using spectral computed tomography with an energy-resolved photon-counting detector," *Physics in Medicine & Biology,* vol. 59, no. 18, p. 5457, 2014.

[8] J. Cammin, S. G. Kappler, T. Weidinger, and K. Taguchi, "Evaluation of models of spectral distortions in photon-counting detectors for computed tomography," *Journal of Medical Imaging,* vol. 3, no. 2, p. 023503, 2016.

[9] K. Taguchi and J. S. Iwanczyk, "Vision 20/20: Single photon counting x‐ray detectors in medical imaging," *Medical physics,* vol. 40, no. 10, 2013.

[10] J. Cammin, J. Xu, W. C. Barber, J. S. Iwanczyk, N. E. Hartsough, and K. Taguchi, "A cascaded model of spectral distortions due to spectral response effects and pulse pileup effects in a photon-counting x-ray detector for CT," (in English), *Medical Physics,* vol. 41, no. 4, Apr 2014.

[11] K. Taguchi *et al.*, "Modeling the performance of a photon counting x‐ray detector for CT: Energy response and pulse pileup effects," *Medical physics,* vol. 38, no. 2, pp. 1089-1102, 2011.

[12] X. Liu *et al.*, "Spectral response model for a multibin photon-counting spectral computed tomography detector and its applications," *Journal of Medical Imaging,* vol. 2, no. 3, p. 033502, 2015.

[13] S. Srivastava, J. Cammin, G. S. Fung, B. M. Tsui, and K. Taguchi, "Spectral response compensation for photon-counting clinical x-ray CT using sinogram restoration," in *Medical Imaging 2012: Physics of Medical Imaging*, 2012, vol. 8313, p. 831311: International Society for Optics and Photonics.

[14] K. Taguchi *et al.*, "Pulse pileup statistics for energy sensitive photon counting detectors with pulse height analysis," in *Medical Imaging 2012: Physics of Medical Imaging*, 2012, vol. 8313, p. 83130Z: International Society for Optics and Photonics.

[15] A. S. Wang, D. Harrison, V. Lobastov, and J. E. Tkaczyk, "Pulse pileup statistics for energy discriminating photon counting x‐ray detectors," *Medical physics,* vol. 38, no. 7, pp. 4265-4275, 2011.

[16] O. Lee, S. Kappler, C. Polster, and K. Taguchi, "A study of modeling x-ray transmittance for material decomposition without contrast agents," in *Medical Imaging 2017: Physics of Medical Imaging*, 2017, vol. 10132, p. 101323G: International Society for Optics and Photonics.

[17] T. G. Schmidt, R. F. Barber, and E. Y. Sidky, "A Spectral CT Method to Directly Estimate Basis Material Maps From Experimental Photon-Counting Data," *IEEE transactions on medical imaging,* vol. 36, no. 9, pp. 1808-1819, 2017.

[18] P.-A. Rodesch, V. Rebuffel, C. Fournier, F. Forbes, and L. Verger, "Spectral CT reconstruction with an explicit photon-counting detector model: a one-step approach," in *Medical Imaging 2018: Physics of Medical Imaging*, 2018, vol. 10573, p. 1057353: International Society for Optics and Photonics.

[19] O. Semerci, N. Hao, M. E. Kilmer, and E. L. Miller, "Tensor-based formulation and nuclear norm regularization for multienergy computed tomography," *IEEE Transactions on Image Processing,* vol. 23, no. 4, pp. 1678-1693, 2014.

[20] O. Lee, S. Kappler, C. Polster, and K. Taguchi, "Estimation of basis line-integrals in a spectral distortion-modeled photon counting detector using low-order polynomial approximation of x-ray transmittance," *IEEE transactions on medical imaging,* vol. 36, no. 2, pp. 560-573, 2017.

[21] W. Zhao *et al.*, "A unified material decomposition framework for quantitative dual‐ and triple‐energy CT imaging," *Medical physics,* 2018.

[22] D. Shen, G. Wu, and H.-I. Suk, "Deep learning in medical image analysis," *Annual review of biomedical engineering,* vol. 19, pp. 221-248, 2017.

[23] G. Wang, J. C. Ye, K. Mueller, and J. A. Fessler, "Image reconstruction is a new frontier of machine learning," *IEEE transactions on medical imaging,* vol. 37, no. 6, pp. 1289-1296, 2018.

[24] H. Greenspan, B. Van Ginneken, and R. M. Summers, "Guest editorial deep learning in medical imaging: Overview and future promise of an exciting new technique," *IEEE Transactions on Medical Imaging,* vol. 35, no. 5, pp. 1153-1159, 2016.

[25] K. Hornik, M. Stinchcombe, and H. White, "Multilayer feedforward networks are universal approximators," *Neural networks*, vol. 2, no. 5, pp. 359-366, 1989.
[26] Y. LeCun, Y. Bengio, and G. Hinton, "Deep learning," *nature*, vol. 521, no. 7553, p. 436, 2015.
[27] N. C. Institute. (5 June). *National Biomedical Imaging Archive (NBIA)*. Available: https://imaging.nci.nih.gov/ncia/login.jsf
[28] J. H. Hubbell and S. M. Seltzer, "Tables of X-ray mass attenuation coefficients and mass energy-absorption coefficients 1 keV to 20 MeV for elements Z= 1 to 92 and 48 additional substances of dosimetric interest," National Inst. of Standards and Technology-PL, Gaithersburg, MD (United States). Ionizing Radiation Div.1995.
[29] G. Poludniowski, G. Landry, F. DeBlois, P. Evans, and F. Verhaegen, "SpekCalc: a program to calculate photon spectra from tungsten anode x-ray tubes," *Physics in medicine and biology*, vol. 54, no. 19, p. N433, 2009.
[30] R. L. Siddon, "Fast calculation of the exact radiological path for a three-dimensional CT array," *Med Phys*, vol. 12, no. 2, pp. 252-5, Mar-Apr 1985.
[31] K. Taguchi, K. Stierstorfer, C. Polster, O. Lee, and S. Kappler, "Spatio‐energetic cross‐talk in photon counting detectors: Numerical detector model (PcTK) and workflow for CT image quality assessment," *Medical physics*, 2018.
[32] L. Le Cam, "Maximum likelihood: an introduction," *International Statistical Review/Revue Internationale de Statistique*, pp. 153-171, 1990.
[33] C. O. Schirra *et al.*, "Statistical reconstruction of material decomposed data in spectral CT," *IEEE transactions on medical imaging*, vol. 32, no. 7, pp. 1249-1257, 2013.
[34] K. Taguchi, S. Srivastava, H. Kudo, and W. C. Barber, "Enabling photon counting clinical x-ray CT," in *Nuclear Science Symposium Conference Record (NSS/MIC), 2009 IEEE*, 2009, pp. 3581-3585: IEEE.
[35] J. Dickmann *et al.*, "A count rate-dependent method for spectral distortion correction in photon counting CT," in *Medical Imaging 2018: Physics of Medical Imaging*, 2018, vol. 10573, p. 1057311: International Society for Optics and Photonics.
[36] H. Ding and S. Molloi, "Image‐based spectral distortion correction for photon‐counting x‐ray detectors," *Medical physics*, vol. 39, no. 4, pp. 1864-1876, 2012.
[37] K. Taguchi, E. C. Frey, X. Wang, J. S. Iwanczyk, and W. C. Barber, "An analytical model of the effects of pulse pileup on the energy spectrum recorded by energy resolved photon counting x‐ray detectors," *Medical physics*, vol. 37, no. 8, pp. 3957-3969, 2010.
[38] E. Roessl, H. Daerr, and R. Proksa, "A Fourier approach to pulse pile-up in photon-counting x-ray detectors," (in English), *Medical Physics*, vol. 43, no. 3, pp. 1295-1298, Mar 2016.

Chapter 5 Summary and outlook

5.1 Summary

CT imaging has been playing a significant role in clinics since it was invented in 1972 [1]. Compared to other imaging modalities such as x-ray imaging, MRI, PET, SPECT, *etc.*, CT imaging has distinguishing characteristics of being able to generate three dimensional images with comprehensive inner structural information in fast speed (less than one second) [2]. The advantages makes CT be the most frequently used imaging technique in clinical practice that the doctors rely heavily on for diagnosis.

However, traditional CT imaging lacks of material-specific capability due to the mechanism of image formation, which makes it cannot be used for molecular imaging. Molecular imaging plays a central role in present and future biomedical research and clinical diagnosis and treatment. For example, imaging of molecular markers and biological processes can provide unprecedented rich information leading to individualized therapies, novel drug design, earlier diagnosis, and personalized medicine. Therefore there exists a pressing need to enable the traditional CT imaging technique with material-specific capability for molecular imaging purpose [3, 4].

The study of chapter 2 was focused on developing an XFMI system to achieve molecular imaging. XFMI utilizes x-ray fluorescence signal to locate a target molecule and reconstruct the elemental distribution in a biological body, which makes it a powerful molecular imaging technique. In this study, a systematic investigation was conducted about the effect of the x-ray excitation spectrum on the molecular sensitivity of XFMI system. Three different excitation spectra were designed by altering the x-ray filter material and thickness, and applied to the XFMI imaging of two iodine-containing phantoms. The results shows that under optimized excitation beam, the molecular sensitivity of the XFMI system was demonstrated to be improved by a factor of 5.26. Furthermore, based on the experimental investigation, an XFMI simulation model was built and validated, which will find use for further improving the molecular sensitivity and guiding the XFMI system design in the future.

The study of chapter 3 was focused on developing a material identification method from PCCT. PCCT is an emerging technique that has the ability to distinguish photon energy and generate much richer image data that contains x-ray spectral information compared to conventional CT. Therefore, the richness of image data opens the possibility to achieve material identification from PCCT. In this study, a physics model was developed based on x-ray matter interaction physics to calculate the effective atomic number (Z_{eff}) and effective electron density ($\rho_{e_{eff}}$) from PCCT image data for material identification. As the validation of the physics model, the Z_{eff} and $\rho_{e_{eff}}$ were calculated under various energy conditions for many materials. The result shows that, given a specific material, the calculated Z_{eff} and $\rho_{e_{eff}}$ from the physics model demonstrate good accuracy and robustness to different energy conditions. To study the feasibility of incorporating the physics model with PCCT data, both physical experiment and numerical simulation of PCCT system were conducted to generate PCCT data from a water phantom and a contrast phantom. Five different materials (C3H6O, H2O, SiO2, NaCl, and CaCl2) that the phantoms are composed of were studied and their Z_{eff} and $\rho_{e_{eff}}$ were calculated from PCCT data. The result shows the Z_{eff} and $\rho_{e_{eff}}$ calculated from PCCT data are well correlated with their reference values, and all the five materials can be clearly separated and identified in the $Z_{eff} - \rho_{e_{eff}}$ map. Therefore, the result shows that material identification can be achieved from the model in the $Z_{eff} - \rho_{e_{eff}}$ map. The model has the value to serve as a material identification scheme for PCCT system for practical use in the future.

The study of chapter 4 was focused on developing a correction method for photon counting CT data correction with deep learning neural network. The data distortion existing in PCCT is the long standing problem which is the biggest factor that diminishes the application of PCCT. For example, as reported in the study of chapter 3, when using the distorted PPCT data for material identification, the error can be as high as 6.3%, as compared to the error of 2.1% without data distortion. In this study, a deep learning neural network based correction approach was developed to correct the data distortion. The network was designed to process each individual sinogram view rather than the reconstructed image or

the sinogram as a whole. Such design can make the algorithm training easier and also retain the performance of the algorithm as well. After the algorithm was trained on PCCT simulation data, when applying the algorithm to process the test dataset data, the accuracy of the PCCT data can be greatly improved (RMSE improved 73.7%). Compared with traditional data correction approaches such as maximum likelihood, the deep learning approach demonstrate superiority in terms of RMSE, SSIM, PSNR, and most importantly, runtime. The proposed method has the potential to facilitate the PCCT studies and applications in practice.

In summary, to accomplish the goal of developing material-specific CT for molecular imaging, three studies were conducted to separately investigate different techniques: x-ray fluorescence molecular imaging, material identification from photon counting CT, and photon counting CT data distortion correction approach based on deep learning. X-ray fluorescence molecular imaging utilizes fluorescence signal to achieve molecular imaging in CT; Material identification can be achieved based on the rich image data from PCCT; And the deep learning based correction method is an efficient approach for PCCT data distortion correction, and furthermore can boost its performance on material identification.

5.2 Outlook

The potential future research directions can be briefly summarized as follows. First, for XFMI research, improving the molecular sensitivity of XFMI system is the key to promote the application of XFMI technique [5]. The molecular sensitivity of XFMI system is jointly affected by many factors, such as the detector configuration [6], the source configuration [7], the choice of contrast agent [8], and so on. For instance, different contrast agent (iodine, gold etc.) has different photoelectric absorption coefficient and fluorescence yield, which will lead to different fluorescence signal intensity. As a result, comprehensive investigations on how different configurations affect the molecular sensitivity are significant in optimizing the XFMI system design. Second, for material identification from PCCT, the data distortion is the major obstacle that limits the accuracy of calculated Z_{eff} and $\rho_{e_{eff}}$[9] . In the simulation study, we found out that different x-ray source setting and

detector energy bins setting can yield to different accuracy level of PCCT data, which further leads to different accuracy level of calculated Z_{eff} and $\rho_{e_{eff}}$. The finding gives rise to the possibility of improving material identification by optimizing PCCT system design [10]. How to optimize PCCT system design to eliminate the data distortion problem could be the future research direction. Third, for PCCT data distortion correction method with deep learning, our study revealed that when applying the developed algorithm to experimental PCCT data, the performance of the algorithm depends on the setting of the detector [10]. We think this is because our training data are not sufficiently diverse and cannot reflect the real distortion pattern distribution in reality. In the simulation, only one specific detector setting was used to generate realistic PCCT data, while in reality the detector can have various setting and even from various vendors, which could lead to different data distortion patterns. How to develop a generic algorithm that can be used to correct the various PCCT data distortion patterns in reality would be the future research direction.

References

[1] R. E. Alexander and R. B. Gunderman, "EMI and the first CT scanner," *Journal of the American College of Radiology,* vol. 7, no. 10, pp. 778-781, 2010.

[2] C. M. Tempany, K. H. Zou, S. G. Silverman, D. L. Brown, A. B. Kurtz, and B. J. McNeil, "Staging of advanced ovarian cancer: comparison of imaging modalities—report from the Radiological Diagnostic Oncology Group," *Radiology,* vol. 215, no. 3, pp. 761-767, 2000.

[3] R. Weissleder, "Molecular imaging in cancer," *Science,* vol. 312, no. 5777, pp. 1168-1171, 2006.

[4] M. A. Pysz, S. S. Gambhir, and J. K. Willmann, "Molecular imaging: current status and emerging strategies," *Clinical radiology,* vol. 65, no. 7, pp. 500-516, 2010.

[5] X. Dong, C. Chen, and G. Cao, "Improving Molecular Sensitivity in X-Ray Fluorescence Molecular Imaging (XFMI) of Iodine Distribution in Mouse-Sized Phantoms via Excitation Spectrum Optimization," *IEEE Access,* vol. 6, pp. 56966-56976, 2018.

[6] M. Ahmad, M. Bazalova, L. Xiang, and L. Xing, "Order of magnitude sensitivity increase in X-ray Fluorescence Computed Tomography (XFCT) imaging with an optimized spectro-spatial detector configuration: theory and simulation," *IEEE Trans Med Imaging,* vol. 33, no. 5, pp. 1119-28, May 2014.

[7] T. Sasaya *et al.*, "Preliminary study on X-ray fluorescence computed tomography imaging of gold nanoparticles: Acceleration of data acquisition by multiple pinholes scheme," *Nuclear Instruments and Methods in Physics Research Section A: Accelerators, Spectrometers, Detectors and Associated Equipment,* 2017.

[8] Y. Kuang, G. Pratx, M. Bazalova, B. Meng, J. Qian, and L. Xing, "First demonstration of multiplexed x-ray fluorescence computed tomography (XFCT) imaging," *IEEE transactions on medical imaging*, vol. 32, no. 2, pp. 262-267, 2013.
[9] X. Dong, O. V. Pen, Z. Zhang, and G. Cao, "An improved physics model for multi-material identification in photon counting CT," in *Medical Imaging 2019: Physics of Medical Imaging*, 2019, vol. 10948, p. 109484O: International Society for Optics and Photonics.
[10] L. Ren, B. Zheng, and H. Liu, "Tutorial on X-ray photon counting detector characterization," *Journal of X-ray science and technology*, no. Preprint, pp. 1-28, 2018.